OXYANION ADSORPTION BY IRON AND RUTHENIUM OXIDES: A MACROSCOPIC, SPECTROSCOPIC, AND KINETIC INVESTIGATION

Todd Peter Luxton

Dissertation Submitted to the Faculty of the Virginia Polytechnic Institute and State University
in Partial Fulfillment of the Requirements for the Degree of

Doctor of Philosophy
In
Crop and Soil Environmental Sciences

Dr. Matthew J. Eick (Chair)
Dr. Michael F. Hochella, Jr.
Dr. Kirk G. Scheckel
Dr. Lucian W. Zelazny

July 18th, 2007
Blacksburg, VA

Keywords: Adsorption, Solid/Solution Interface, Arsenic, Chromium, Spectroscopy, Pressure-Jump Relaxation Kinetics

Oxyanion Adsorption by Iron and Ruthenium Oxides: A Macroscopic, Spectroscopic, and Kinetic Investigation

T. P. Luxton

DISSERTATION ABSTRACT

The adsorption and desorption behavior of trace element contaminants was evaluated on two solids—goethite and ruthenium oxide. The importance of anion displacement as a mechanism responsible for arsenic release from iron oxides was investigated on goethite. The adsorption and polymerization of silicate on goethite was examined as a function of surface concentration to determine the influence of adsorbed silicate monomers and polymers on arsenite adsorption and desorption. A kinetic model was employed to describe arsenite adsorption and desorption in the absence and presence of silicate. The potential environmental impacts of the research are discussed. Hydrous and crystalline ruthenium oxides were extensively characterized by traditional colloidal surface characterization techniques, dissolution experiments, and macro- and spectroscopic experiments. The two ruthenium oxide phases exhibited large specific surface areas, a high density of reactive surface functional groups and the presence of multiple Ru oxidation states in both solids. Enhanced dissolution of hydrous ruthenium oxide occurred in the presence of oxalate and ascorbate. While enhanced dissolution of the crystalline phase occurred only in the presence of oxalate at pH 3. Results from the dissolution experiments were used to develop possible mechanisms for the oxalate and ascorbate promoted dissolution of ruthenium oxides. Macroscopic adsorption studies of arsenate adsorption on both ruthenium oxides were examined over a broad pH (3-10) and initial solution concentration range (0.01 to 33 mM). Results from the adsorption studies indicate arsenate forms a stable surface complex with both ruthenium oxide phases. Extended x-ray absorption fine structure spectroscopy and Pressure-jump relaxation studies indicates arsenate is specifically adsorbed the ruthenium oxide surface. Chromate adsorption on ruthenium oxides was investigated as a function of pH and initial chromate solution concentration. Macroscopic adsorption studies and zeta potential measurements suggest chromate forms an inner-sphere surface complex with both oxide phases. X-ray absorption near edge spectroscopy data indicates chromate (Cr(VI)) is reduced to chromium (Cr(III)) on the ruthenium oxide surface. Modeling of the first Cr shell indicated the two oxygen backscattering distances similar to the Cr-O atomic distances reported for oxygen coordinated to Cr(VI) and Cr(III) providing additional evidence for Cr(VI) reduction.

ACKNOWLEDGEMENTS

Any success I have had in life belongs more to family and friends than it does to me. I want to thank my advisor, Dr. Matthew Eick, for providing me with the opportunity to freely explore my scientific interests. Matt has been an incredible advisor, mentor, and friend. I could have never finished my dissertation project without his encouragement, support, and insight. I also want to extend my deepest gratitude to the other members of my Ph.D. committee: Dr. Kirk Scheckel, Dr. Lucian Zelazny, and Dr. Michael Hochella Jr. for being so generous with their time. Special thanks to Kirk and Dr. Zelazny for all of the time they spent with me in the laboratory and classroom. I also want to thank the present and former members of the Soil Chemistry group including: Jillian Campbell, Stephanie Garman, Mindy Waltham, and Joe Hunt. I have enjoyed working, laughing, and swearing with all of you. In addition to the former soil chemistry graduate students, I am grateful to my fellow graduate students in the CSES department. Special thanks to John Spargo for countless conversations and arguments that have enabled me to grow as a scientist. I look forward to hopefully working with you in the future. I also want to thank Dr. Andrew Madden, Dr. Michael Borda, Kelly Haus, and Nick Wigginton for all their help in the laboratory.

In addition to my Virginia Tech colleagues I want to thank my friends and family for everything they have done and all of their support. I cannot thank you enough. I am so blessed to be a part of such a wonderful community of people. Special thanks to my parents, Linda and Pete, who sacrificed so much for my brother and I.

TABLE OF CONTENTS

LIST OF TABLES

LIST OF FIGURES

THE ROLE OF SILICATE IN THE ADSORPTION/DESORPTION OF ARSENITE ON GOETHITE

ABSTRACT

The importance of anion displacement as a mechanism for arsenic release was examined through the competitive adsorption and desorption of arsenite on goethite in the presence of silicate. Arsenite remained the only arsenic species throughout the adsorption studies. Oxyanion surface concentration versus time plots developed from adsorption experiments were analyzed with a kinetic rate equation to determine the apparent rate coefficients for arsenite and silicate alone and arsenite in the presence of pre-equilibrated silicate. Silicate adsorption on goethite was significantly slower than arsenite. FTIR analysis indicated that silicate polymerization on goethite may be related to the slow adsorption kinetics. Under all conditions pre-equilibrated silicate reduced the rate and total quantity of arsenite adsorbed. The percent increase in the final aqueous arsenite concentration ranged from 0.25 to 30% depending on the concentration of the adsorbed silicate and aqueous arsenite. Increases in the aqueous arsenite were greatest after 30 minutes before reaching a steady state after 150 minutes. Desorption experiments where silicate was introduced to previously adsorbed arsenite indicated that silicate was able to irreversibly displace between 0.3 and 1.5% of the adsorbed arsenite resulting in an increase in solution concentrations ranging from 9 to 266 $\mu g\ L^{-1}$ of arsenite. Experimental results demonstrate the importance of anion displacement as a mechanism for arsenic release. This is readily seen through the ability of silicate, a naturally occurring and ubiquitous oxyanion, to: 1) reduce arsenite adsorption rates, 2) block potential adsorption sites thereby reducing the total quantity of arsenite adsorbed, and 3) displace adsorbed arsenite. These three processes may ultimately result in an increase in the mobility and potential bioavailability of arsenite.

INTRODUCTION

The potential bioavailabilty and transport of trace element oxyanions (eg. As, Cr(VI), W(VI) I(V), Se, and Sb,) in natural systems is strongly governed by adsorption/desorption reactions at the solid/solution interface (Brown et al., 2002; McBride, 1994; Sparks, 2003; Sposito, 1989). Furthermore, iron (hydr)oxides, due to their natural abundance and surface reactivity play a crucial role in controlling the partitioning of oxyanions between the solid/solution interface (Schwertmann and Cornell, 1996). Numerous studies have evaluated oxyanion interactions with mineral surfaces from a steady state or thermodynamic standpoint. This information is vitally important in developing geochemical models that predict oxyanion bioavailability in the environment. In most scenarios, geochemical models are used to predict the final elemental speciation, but not the rate at which the system approaches steady state after a perturbing chemical or physical process. Therefore, examining the kinetics of reactions at the solid/solution interface in geologic systems is critically important to understanding contaminant mobility and bioavailability (Lasaga, 1998; Lasaga and Kirkpatrick, 1981; McBride, 1994; Sparks et al., 1996).

Currently, there are three widely accepted mechanisms for arsenic release in sediments and soils: 1) oxidation of arsenic rich sulfide materials, 2) reductive dissolution of iron oxides and concurrent release of adsorbed arsenic, and 3) anion displacement (competitive adsorption/desorption) (Acharyya and Shah, 2007; Nickson et al., 2000; Nordstrom, 2002; Polizzotto et al., 2006; Polizzotto et al., 2005; Singh, 2006; Swartz et al., 2005; van Green et al., 2006). Of these proposed mechanisms anion displacement has received the least amount of

attention. The well established correlations and solid state speciation have led many to conclude reduction/oxidation reactions are the only important factor controlling arsenic release, even when the field data does not support the conclusion. Recently, van Green, et al. (2006) evaluated potential mechanisms controlling arsenic solubility in detailed groundwater profiles of eight shallow wells (~30 m) in a 4 km^2 area of Bangladesh. The researchers reported that more than 95% of the arsenic was in the form of arsenite and better correlations exist between dissolved arsenic and phosphate extracted (P-extract) arsenic and cation concentration (Na, K, Mg, and Ca) as compared to dissolved arsenic and Fe(II) concentration. It is unlikely that the base cations compete with arsenic for sorption sites. But the correlation between the two concentrations may be the result of elevated pH or dissolution of carbonate and silicate minerals which concurrently release (bi)carbonate, and silicate (Fetter, 1994; Garrels, 1967). The results of van Green, et al. (2006) suggest that anion displacement may be an important factor in releasing arsenic in areas of the Ganges- Brahmaputra river basin.

The importance of anion displacement as a mechanism for arsenic release cannot be over looked or underestimated. Several laboratory based and field studies have demonstrated the ability of naturally occurring inorganic ions to displace adsorbed arsenic or inhibit arsenic adsorption (Acharyya and Shah, 2007; Aggett and Roberts, 1986; Appelo et al., 2002; Darland and Inskeep, 1997; Dixit and Hering, 2006; Gao et al., 2006; Garman et al., 2004; Grafe et al., 2001; Grafe et al., 2002; Liu et al., 2001; Luxton et al., 2006; Meng et al., 2000; Nickson et al., 2000; Polizzotto et al., 2006; Redman et al., 2002; Smith et al., 2002b; Swartz et al., 2005; Swedlund and Webster, 1999; Waltham and Eick, 2002).

Most anion displacement research has focused on phosphate promoted desorption of arsenic; due to the increased use of agronomic fertilizers and adsorbed to water treatment residuals in high phosphate drinking water.. Fewer researchers have evaluated the potential roles of silicate, carbonate, and sulfate, three naturally occurring and ubiquitous anions. Phosphate promoted desorption of arsenic plays a critical role in agricultural settings, but in unammended soils phosphate is present at relatively low concentrations due to continuous biological uptake (Geelhoed et al., 1997; Singh, 2006; Tadanier and Eick, 2003). Relatively few studies have focused on arsenic desorption by sulfate and those that have indicate sulfate is not an effective desorbent (Mahoney et al., 2005; Meng et al., 2000; Smedley et al., 2002). The influence of (bi)carbonate on arsenic desorption has been more thoroughly evaluated due to the predominance of elevated carbonate concentrations in groundwater associated with carbonate mineralogy and elevated pH. These studies have shown that in neutral to basic pH environments when (bi)carbonate concentrations exceed reactive surface sites densities, (bi)carbonate promotes arsenic desorption (Anawar et al., 2004; Appelo et al., 2002; Meng et al., 2000; Pantsar and Manninen, 1997; Smedley and Kinniburgh, 2002). However, in acidic environments and/or at low concentrations (bi)carbonate is not effective at promoting arsenic desorption (Anawar et al., 2004; Appelo et al., 2002; Meng et al., 2000; Nickson et al., 2000).

Research examining the influence of silicate on inhibiting arsenic adsorption has focused on both engineered and natural environments (Luxton et al., 2006; Meng et al., 2000; Polizzotto et al., 2006; Swartz et al., 2005; Swedlund and Webster, 1999; van Green et al., 2006; Waltham and Eick, 2002). Orthosilicate ($H_4SiO_4^0$ and $H_3SiO_4^-$), like arsenic, has a high affinity for iron-(hydr)oxide surfaces, also forming inner-sphere surface complexes through a ligand exchange with surface hydroxyl functional groups (Doelsch et al., 2003; Doelsch et al., 2001; Hansen et al., 1994b; Sigg and Stumm, 1981; Vempati and Loeppert, 1989; Vempati et al., 1990). Silicate is commonly present in the environment at concentrations between 5-35 mg L^{-1} (0.17 to 1.24

mM) and not infrequently at concentrations as high as 75 mg L^{-1} (2.7 mM) in groundwater (Iler, 1979). Hence, silicate is a potentially effective ligand for inhibiting adsorption or promoting desorption of arsenite. The rate of silicate adsorption on iron (hydr)oxides is considerably slower than arsenite (Garman et al., 2004; Hansen et al., 1994b; McPhail et al., 1972; Waltham and Eick, 2002). Unlike most oxyanions, silicate under goes polymerization at relatively low solution concentrations (Alverez and Sparks, 1985; Applin, 1987), and on hydrous oxide surfaces, potentially enhancing the competitive ligand effect (Doelsch et al., 2003; Doelsch et al., 2001; Hansen et al., 1994b; Vempati et al., 1990). The polymerization of silicate on mineral surfaces is hypothesized to be one of the reasons for its slow adsorption kinetics (Hansen et al., 1994b).

The competitive interaction between dissolved silica, both in monomeric and polymeric forms, and arsenite adsorbed on poorly crystalline hydrous iron oxides has been previously investigated (Meng et al., 2000; Swedlund and Webster, 1999). These studies indicated that silicate was able to competitively displace arsenite sorbed on ferrihydrite. However, neither study evaluated changes in the rate of arsenite adsorption in the presence of silicate, or how sorbed arsenite would react to the introduction of silicate. Waltham and Eick (2002) reported on the kinetics of arsenite adsorption in the presence of silicate and found that silicate does reduce the rate and total quantity of arsenite adsorbed. However, they did not evaluate the effect of silicate polymerization, or the potential desorption of equilibrated arsenite upon the introduction of silicate.

In this paper we examine the extent to which silica, as a naturally occurring competitive ligand, affects the mobility and potential bioavailability of arsenite in natural and engineered environments where sorption onto crystalline iron (hydr)oxide mineral surfaces is a significant mechanism for contaminant sequestration. The research objectives are threefold. First, determine to what extent silicate inhibits arsenite adsorption and adsorption rates on goethite. Second, evaluate silicate adsorption on goethite using FTIR spectroscopy to determine if silicate polymerization occurs under the experimental conditions and how silicate polymers affect arsenite adsorption. Finally, evaluate the potential for silicate to desorb appreciable quantities of adsorbed arsenite.

METHODS AND MATERIALS

Goethite Synthesis and Characterization

Goethite used in the current study was synthesized by hydrolysis of ferric nitrate ($Fe(NO_3)_3$) using a method described by Schwertmann and Cornell (1991). All solutions were prepared with distilled doubly-deionized water and reagent grade chemicals. Contact with glass surfaces was avoided to prevent silica contamination. The identity, purity, and structure of the goethite sample was confirmed by x-ray diffraction (XRD), differential scanning calorimetry (DSC), thermogravimetric analysis (TGA), and field emission scanning electron microscopy (FESEM). Results form these analyses were consistent with data presented by Schwertmann and Cornell (1991 and 1996) and a goethite standard from Bayer® (Krefeld, FRG). Field emission scanning electron microscopy images showed that the synthetic goethite consisted of euhedral acicular crystals of uniform shape and size approximately 300 nm in length and 75 nm laterally. The quantity of poorly crystalline or amorphous Fe was determined by the ratio of ammonium oxalate (AO) in the dark to citrate-bicarbonate-dithionite (CBD) extractable Fe (Loeppert and Inskeep, 1996; Schwertmann and Cornell, 1991). The extractable Fe was 0.28 % (AO Fe mg /

CBD Fe mg), indicating minimal amounts of amorphous or short-ordered crystals. Specific surface area was 73 m^2 g^{-1}, as determined by a five point N_2 Brunauer-Emmett-Teller (BET) gas adsorption isotherm. The point of zero charge as determined by the isoelectric point (IEP) was 9.56.

Oxyanion Adsorption/Desorption

The kinetics of arsenite (H_3AsO_3) and silicate (H_4SiO_4) adsorption on goethite and arsenite desorption were examined as a function of pH, concentration, and competitive anion interaction at constant ionic strength (0.01M NaCl) and suspension density (1 g L^{-1}) utilizing a pH-monitored stirred-batch reactor. Kinetic adsorption experiments were conducted in duplicate at pH 4, 6 and 8 at two oxyanion concentrations (50 and 100 μM for arsenite; 100 and 1000 μM for silicate). Arsenite adsorption kinetics were measured in the absence and presence of a competing oxyanion. In the competing oxyanion experiments, two addition scenarios were evaluated: a) equilibration with silicate before measuring arsenite adsorption kinetics and b) equilibration of the goethite surface with arsenite prior to measuring arsenite desorption kinetics. For the kinetic adsorption experiments an appropriate quantity (0.400 g) of freeze dried and N_2 sparged goethite was weighed into a 500 mL Teflon reaction vessel to which 350 mL of 0.01 M NaCl was added. The suspension was dispersed for ~2min using an ultrasonic dimembrator. The Teflon linear was placed in a water jacketed reaction vessel kept at 25^o C, stirred at 300 rpm using a three blade impeller, and kept under positive pressure with N_2 gas to eliminate CO_2 effects and to prevent arsenite oxidation. The suspension was allowed to hydrate for a period of 24 h while the pH was adjusted to the appropriate value using a Brinkman® 716 Stat-Trino pH stat (Brinkman Instruments, Westbury, NY) with either 0.1 M HCl or NaOH.

For the single oxyanion kinetic experiments, after the 24 h hydration period the suspension was brought to volume (400 mL) minus the quantity of arsenite or silicate stock solutions to be added. The arsenite was added from a 0.015 M sodium arsenite stock solution kept under positive N_2 pressure to prevent oxidation. The silicate stock solution was added from a 0.0123 M sodium silicate stock solution kept at pH 11 to prevent silica polymerization (Iler, 1979). All stock solutions were made with reagent grade sodium salts. Sampling began 5 minutes after the addition of the oxyanion and continued until a steady state was reached. The steady state time was chosen to be the time when there was minimal change in the quantity of arsenite or silicate in solution.

For the competitive oxyanion adsorption kinetics the same procedure previously described was used with the following modifications. After hydration the goethite suspension was brought to a volume of 390 mL and either silicate or arsenite was added to the suspension. The suspension was then allowed to equilibrate at a constant pH prior to the addition of the second oxyanion. For arsenite the equilibration time period was 4 h, and for silicate the equilibration time period was 40 h. The length of time required for the system to reach a steady state was determined from the single ion adsorption experiments and a review of the literature (Garman et al., 2004; Grafe et al., 2001; Hansen et al., 1994a; Raven et al., 1998; Waltham and Eick, 2002). After equilibration, the suspension was brought to volume minus the quantity of solution containing the second oxyanion. The second oxyanion was added and sampling began after 5 minutes. The pH of the suspension was monitored throughout the duration of the experiment and adjusted as needed using either 0.1 M HCl or NaOH. At specific time intervals a 10 mL sample was removed from the reaction vessel and filtered through a 0.22 μm Fisher brand® (Fisher, Atlanta, GA) membrane. The resulting filtrate was analyzed for Si and/or As

using an inductively coupled plasma atomic emission spectrometer (ICP-AES) (SpectroFlame FTMOA85D, Spectro Analytical Instruments, Fitchburg, MA). The detection limit on the SpectroFlame ICP-AES for As and Si was 10 and 6 μg L^{-1} respectively. The quantity of oxyanion adsorbed at specific time intervals was determined by subtracting the initial oxyanion concentration by the measured concentration. The quantity of arsenite desorbed was determined by subtracting the concentration of arsenite at time (*t*) from the solution concentration of arsenite prior to the addition of silicate.

Arsenic Speciation

The presence of arsenate due to the oxidation of arsenite by Fe(III) was determined by analyzing for dissolved Fe(II) colormetrically by 1,10-phenanthroline, and adsorbed arsenate by x-ray photoelectron spectroscopy (XPS) at pH 4. Since the oxidation of arsenite to arsenate is favored at low pH it was assumed if there was no oxidation of arsenite at pH 4 then arsenite would be stable at higher pH values (Inskeep et al., 2002). For the Fe(II) analysis a goethite suspension was prepared using the same suspension density and experimental procedures described in the Oxyanion Adsorption/Desorption section. The method was modified by extending the equilibration time to 70 h. A 10 mL sample was removed from the reaction vessel and filtered through a 0.22 μm filter at 30 min, 1, 5, 10, 20, 40, 60, and 70 h for Fe(II) analysis. After filtration the samples were acidified to pH < 2 and stored at 5^{o} C to prevent oxidation of Fe(II). The presence of Fe(II) was determined using the 1,10 phenanthroline method presented by Loeppert and Inskeep (1996) using a Beckman Coulter DU® 640 (Fullerton, CA) spectrophotometer with a visible source set at 510 nm.

After the 70 h equilibration time period a 25 mL sample of the goethite suspension was filtered and washed with 0.01 M NaCl. The resulting solid was allowed to dry under a positive N_2 pressure. The subsequent goethite was analyzed by XPS to evaluate the redox status of the adsorbed As on the surface. XPS spectra were collected on a Perkin-Elmer 5400 ESCA system (Wellesley, MA). The x-ray source was monochromatic Al Kα radiation at 1486.7 eV. Both wide and narrow scans were used, the former to determine the range and abundance of elements present and the latter to determine the chemical state. A small advantageous C(1s) peak (285.0 eV) was monitored throughout each experiment. The C(1s) peak was invariant throughout each experiment and corrections for charging were not required. Binding energies for the As(3d) peak were assigned relative to the advantageous C(1s) peak. Narrow scans for the As speciation were collected from 60 to 40 eV for the As(3d) binding energy. The presence of the Fe(3p) peak at 55.6 eV did not interfere with the As(3d) peak. In order to determine the chemical state of the adsorbed As, reference spectra of arsenite and arsenate reagent grade arsenic sodium oxides ($NaAsO_2$ and $NaAsO_3$) were collected prior to the goethite analysis to determine peak position for As(V) and As(III). Spectra obtained from the As(3d) binding energy region were collected for 1200 cycles of 0.1 eV/step at a 20 msec/step.

Kinetic Analysis of Oxyanion Adsorption/Desorption Data

The rate of arsenite and silicate adsorption and arsenite desorption was determined by fitting the adsorption data (time vs. surface concentration or solution concentration) to a modified Mitscherlich equation (Mitscherlich, 1909). For the analysis of the current adsorption data we included a y-intercept (C_1) in the original equation (Eq. 1-1).

$$C = C_1 + a*(1-e^{-kt}) \quad (1\text{-}1)$$

The rational for including a y-intercept will be discussed later. The two measured parameters in the modified Mitscherlich equation are *C* and *t* corresponding to concentration and time, respectively. For ion adsorption *C* equals the surface concentration (μmol m^{-2}), while for ion desorption *C* is equal to solution concentration (μM). In the current formulation of the equation, C_1 is equal to the y-intercept, *a* is equal to the total concentration of oxyanion adsorbed or desorbed as time approaches ∞, and *k* is the rate coefficient. The parameters C_1, *a*, and *k* are constants. For the arsenite desorption experiments C_1 was set to zero. Adsorption rates were determined from the averaged data for each of the individual experiments (n=2) at a specific pH. The adsorption data was fit with the modified Mitscherlich equation using the method of least squares for non-linear regression and the computer program SigmaPlot© (Version 10.0, 2006 Systat Software, Inc. San Jose, CA, USA). The rate of ion adsorption/desorption was determined by taking the derivative of the equation with respect to time (*t*). Thus the adsorption/desorption rate (r) equals

$$r = \frac{dC}{dt} = ake^{-kt} \quad (1\text{-}2)$$

FTIR Spectroscopy

Fourier transformed infrared (FTIR) spectra were collected for silicate adsorption on goethite as a function of reaction time, silicate concentration and pH. FTIR spectra were obtained with a Thermo Nicloet Nexus® 670 spectrometer and a horizontal Thermo Nicolet Smart ARK ATR attachment equipped with a 45° ZnSe trapezoidal crystal with 12 internal reflections and a cutoff of 600 cm^{-1} (Thermo Electron, Madison WI). The measured path length was approximately 12 μm based on the molar absorptivity of water. The spectrometer was equipped with a KBr beam splitter and a DTGS detector. The experimental procedure for preparing IR samples followed the same procedure described in the Oxyanion Adsorption/Desorption section with the following modifications. After 6 and 48 h a 25 mL sample was removed from the reaction vessel for FTIR analysis. The sample was filtered onto a 0.22 μm membrane. The resulting goethite was then washed with 25 mL of 0.01 M NaCl to remove entrained non-reacted silicate prior to IR analysis. The wet goethite paste was smeared onto the ZnSe crystal and immediately analyzed. Spectra were obtained from the co-addition of 512 scans collected at a resolution of 4 cm^{-1}. Data analysis of the collected spectrum was performed with the Omnic software package (Version 7.2, 2005, Thermo Scientific, Waltham, MA, USA). All of the spectra were corrected for the presence of water. Additionally, a spectrum of unreacted goethite (prepared under the same conditions) was subtracted from the goethite + silicate spectrum in order to evaluate only the adsorbed silica species. After the goethite subtraction the resulting spectra was baseline corrected between 1400 and 700 cm^{-1} using a linear function.

RESULTS AND DISCUSSION

Arsenic Speciation

Based on the results of the colormetric assay and XPS spectra arsenite was not oxidized to arsenate. There was no detectable Fe(II) in any of the filtrates collected over the 70 h

equilibration time period. The reference binding energy for the arsenate and arsenite sodium salts was 45.7 and 44.4 eV respectively which are in excellent agreement with those presented in the National Institute of Standards and Technology, U.S. database (2002). The binding energy for the As adsorbed to the goethite surface was 44.4 eV and exhibited a similar peak width at half max as that of the $NaAsO_2$ (2.1 eV). Several studies have found similar binding energies for As(III) associated with Fe oxides (Bang et al., 2005; Costa et al., 2002; Nesbitt et al., 1995). While the oxidation of arsenite to arsenate is thermodynamically favorable at low pH the kinetics have been reported to be extremely slow in pure systems with high Fe:As ratios (Devitre et al., 1991; Oscarson et al., 1981; Oscarson et al., 1980; Sun and Doner, 1998).

Kinetic Rate Analysis

The Mitscherlich equation was originally developed to model agronomic crop yield response to fertilizer application rates but has been extensively modified and used in other scientific disciplines to model and interpret data that exhibits exponential growth (Black, 1993). Previously, the equation has been applied to geochemical research regarding the dissolution of rock phosphate and phosphate availability in agricultural soils (Mackay et al., 1986; Yampracka et al., 2006). However, to our knowledge the equation has not been used to model ion adsorption data.

The Mitcherlich equation and our modified equation are ideally suited for modeling kinetic batch reactor data. The two advantages of the equation are the ability to determine a rate coefficient and estimate equilibrium surface ion concentration from ion adsorption data plotted as a function of time. The value of the rate coefficient is determined by the non-linear regression of the adsorption data (k), and the estimated equilibrium concentration is equal to a or C_1+a as time approaches infinity. The biggest draw back of the equation is the inherent assumption that the reaction is first order with respect to the adsorbing/desorbing ion as a result of the rate being directly proportional to a (Equation 1-2). However, with the inclusion of a y-intercept (C_1) the reaction does not necessarily need to be first order due to the non-zero intercept. This allows for greater flexibility in modeling ion adsorption data while still providing an empirical or relative rate coefficient that allows for comparison of experimental results without needing to determine an empirical rate law.

Initially, the oxyanion adsorption data was evaluated without the inclusion of y-intercept. We assumed the oxyanion surface concentration was zero at time zero, thereby forcing the equation through the origin. The nonlinear regression analysis resulted in an under estimation of the quantity of oxyanion adsorbed after 15 minutes and the time required to reach equilibrium. Additionally, it underestimated the final equilibrium surface concentration (Figure 1-1). The under estimation of adsorbed oxyanion concentration and over estimation of the time to reach equilibrium artificially inflated the rate at which arsenite is adsorbed on goethite. The inclusion of a y-intercept in the model enabled a better prediction of the adsorption data as the system approached equilibrium. In the current study the emphasis is on evaluating increased arsenite bioavailabilty in environments where iron oxide sequestration is an important factor controlling arsenite transport and bioavailabilty. In order to accurately evaluate increased mobility and bioavailability due to longer sorption time periods it was necessary that our kinetic model accurately describe changes in adsorption rates near equilibrium. Therefore, it was necessary to introduce a y-intercept (C_1).

Adsorption Kinetics

Single Oxyanion Adsorption

The complete results from the adsorption of silicate and arsenite alone and the adsorption of arsenite in the presence of silicate are tabulated in Luxton (2007). Figure 1-1 contains an example of the adsorption results for arsenite and silicate adsorption as a function of time at pH 6 and an initial oxyanion solution concentration of 100 μM. The data presented in Figure 1-1 is representative of the results for the other oxyanion concentrations investigated. The adsorption results indicate that arsenite adsorption rates exceeded those of silicate as evidenced by the time required to reach equilibrium (note shorter time span for arsenite adsorption). Results from the non-linear regression analysis of adsorption data, for arsenite and silicate alone, are presented in Table 1-1. The value of C_1 for arsenite adsorption greatly exceeds the value of a, indicating that under all conditions 90% or more of the reaction was completed in the first 5 minutes (Table 1-1). Previous research has demonstrated that oxyanion adsorption on iron oxides is fast requiring chemical relaxation techniques to accurately determine initial adsorption rates (Grossl et al., 1997; Grossl and Sparks, 1995). However, due to the acute toxicity of arsenite associated with low solution concentrations, changes in adsorption rates near equilibrium become extremely important in estimating increased bioavailability. Based on the rate coefficients calculated, arsenite adsorption rates displayed a weak dependence on initial solution concentration and pH. Interestingly, the total quantity of arsenite adsorbed was not influenced by pH (Table 1-1). In contrast silicate adsorption was more dependent upon initial solution concentration and pH.

Waltham and Eick (2002) noted a similar dependence for silicate and arsenite adsorption rates based on pH and initial solution concentration. They attributed the slower adsorption kinetics of silicate to the very weak acidic oxyanion ($pK_a = 9.98$). However, arsenite, is also a weak acid ($pK_a = 9.22$), but does not exhibit the same pH or concentration dependence. The reason for these differences is not well understood, but may be related to two potential factors: 1) a change in the arsenite bonding mechanism at low pH and 2) silicate polymerization on the goethite surface. Goldberg and Johnston (2001) and Ari, et al. (2001) have both suggested and shown spectroscopically that arsenite can bind with iron and aluminum oxide surfaces via an outer-sphere mechanism, possibly through a positively charged surface site and the lone pair of electrons on As in the arsenite molecule. At pH 4 the goethite exhibits zeta potential value of ~40 mV indicating a large positive surface charge (Luxton et al., 2006) providing an environment conducive for outer-sphere adsorption. The formation an outer-sphere arsenite complex at low pH may supersede the ligand exchange mechanism necessary for ion adsorption and enhance the removal of arsenite from solution. This phenomenon could account for the lack of a pH dependence on arsenite adsorption and the increased adsorption rates at pH 4 and 6 as compared to silicate.

Along with a change in arsenite bonding mechanism, the formation of silicate polymers on the goethite surface is a likely candidate for the differences in adsorption rates. The slower adsorption kinetics of silicate is well documented in the literature (Dietzel, 2002; Garman et al., 2004; Hansen et al., 1994a; Waltham and Eick, 2002). Research has suggested that the slow adsorption rate is related to the formation of silica polymers on iron (hydr)oxide surfaces (Hansen et al., 1994b). While silicate solution concentrations in all experiments were below saturation for amorphous silica, goethite may serve as a template for silicate polymerization by concentrating silica on the surface in localized environments that either approach or exceed saturation. Silica polymers on iron oxides have been observed with FTIR spectroscopy on ferrihydrite at initial solution concentrations less than amorphous silica saturation (Doelsch et al.,

2003; Doelsch et al., 2001; Hansen et al., 1994b; Vempati and Loeppert, 1989; Vempati et al., 1990).

Competitive Arsenite Adsorption

Under the competitive adsorption scenarios silicate was pre-equilibrated with the goethite surface prior to the addition of arsenite. Arsenite adsorption rates along with the total quantity of arsenite adsorbed decreased in the presence of silicate (Table 1-2 and Figure 1-2). The effect of silicate on the reduction in the arsenite rate coefficient was greatest between 0 and 100 μM silicate for both arsenite concentrations. The value of the rate coefficient was reduced by 37% and 57% for the 50 and 100 μM arsenite concentrations, respectively, and by an additional 25 and 14% from 100 to 1000 μM silicate. The reduction in arsenite adsorption rates becomes important when considering aqueous arsenite transport from an anoxic to oxic environment where sorption by iron hydroxides is the dominant mechanism for sequestering arsenic.

There was a minimal reduction in the total quantity of arsenite adsorbed for 50 μM arsenite and a 3 to 5% reduction for 100 μM arsenite after the adsorption of 100 μM silicate. Desorption data for silicate indicated between 0.05-0.10 and 0.23-0.33 μmol m^{-2} of silicate was desorbed for 50 and 100 μM arsenite, respectively. The lack of a significant reduction in the total quantity of arsenite adsorbed and silicate desorbed is attributed to an excess of reactive surface sites. Previous research suggests that the concentration of reactive surface sites on goethite is between 3.5 and 6 μmol m^{-2} minus the sites required for charge balance (Barrón and Torrent, 1996; Hiemstra and van Riemsdijk, 1996).

The impact silicate has on reducing the rate and total quantity of arsenite adsorbed is best demonstrated by analyzing the arsenite solution data. The last column in Table 1-2 shows the increase in the final aqueous concentration of 50 and 100 μM arsenite due to the presence of adsorbed silicate at equilibrium. Under all conditions there was an order of magnitude increase in the final aqueous arsenite concentration as silicate increased from 100 to 1000 μM or from 2.8 to 28 mg L^{-1} silicate. The increase in the total aqueous arsenite at equilibrium demonstrates the ability of adsorbed silicate to block arsenite adsorption sites on goethite. This results in an increase in arsenite mobility and bioavailabilty. Aqueous arsenite solution concentrations, during adsorption, in the presence and absence of silicate demonstrate an increase in aqueous arsenite as a function of time up to 150 minutes when silicate is present of the goethite surface (Figure 1-3A-dashed line). The increase in arsenite bioavailabilty initially varies with time (Figure 1-3B) leading to a dramatic increase in aqueous arsenite during the first hour of adsorption. The aqueous arsenite concentration at 200 minutes is equal to the increase in arsenite concentration listed in Table 1-2. All of the other data sets exhibited similar trends where arsenic was most available after ~30 minutes. Experimental results from the competitive adsorption of arsenite demonstrate the ability of ambient silicate concentrations to initially elevate aqueous arsenite concentrations dramatically during adsorption, and inhibit or block arsenite adsorption sites on goethite. The reduction in rate and total quantity adsorbed ultimately results in increased aqueous arsenite. Recent studies conducted in the Ganges-Brahmaputra river basin have reported dissolved silicate concentrations between 35 and 1900 μM in locations with elevated arsenic (Polizzotto et al., 2006 and Swartz et al., 2005) suggesting elevated arsenite concentrations may be related to silicate adsorption on iron (hydr)oxides.

The moderate reduction in the arsenite adsorption rate coefficient as silicate concentration was increased, is supported by the fact that there was an overall reduction (12%) in the total arsenite adsorbed. We expected a much larger reduction in the rate coefficient and the

total quantity of arsenite adsorbed based on previous work. Silicate adsorption isotherms conducted on goethite with similar chemical and physical properties (acidity, size, surface area) indicated complete saturation of reactive surface sites at silicate concentrations of 1000 μM (Luxton and Eick, 2004). However, for both arsenite concentrations the quantity of arsenite adsorbed per silicate desorbed was less than one, indicating more arsenite was adsorbed than silicate desorbed. The lack of a 1:1 relationship suggest either a change in the arsenite binding mechanism (outer- instead of inner-sphere) or a change in the silicate binding mechanism.

FTIR Spectroscopy

The adsorption kinetics of silicate was further investigated to determine if the differences in adsorption rates were related to the formation of silica polymers and the impact polymers might have had on arsenite adsorption. The primary IR region of interest was located between 1300 and 900 cm^{-1}. This area is associated with Fe-O-Si linkages (970-930 cm^{-1}), Si-OH linkages (960-1000 cm^{-1}) and asymmetric Si-O-Si stretching vibrations (1080 and 1150 cm^{-1}) (Chaneac et al., 1996; Della Volpe et al., 1997; Doelsch et al., 2003; Doelsch et al., 2001; Hansen et al., 1994b; Mul et al., 2004; Parfitt et al., 1992; Vempati and Loeppert, 1989). Spectra collected at pH 4 and 6 at two time intervals (6 h and 48 h) are presented in Figures 1-4 and 1-5. In both figures plot A corresponds to 100 μM Si and plot B to 1000 μM. Results from the FTIR analysis indicate silicate does polymerize on goethite and that silicate polymerization is related to both concentration and pH. The broad absorption peaks associated with silicate is probably related to the disordered nature and size of the silica polymers resulting from changes in goethite surface morphology (Hochella, 1990). Numerous studies characterizing silica gels have noted wide variations in the position of Si-O-Si absorption bands due to differences is the synthesis methods and the presence or absence of a substrate (Chaneac et al., 1996; Della Volpe et al., 1997; Mul et al., 2004). Similarly, van der Marel and Beutelspacher (1976), provide several examples of variations in the exact location of IR absorption bands for SiO_2 phases. The FTIR spectra indicate that silicate initially adsorbs to the goethite surface as a monomer or possibly a dimer (Alverez and Sparks, 1985) before undergoing further polymerization. Adsorption and FTIR data suggest that the mechanism for silicate polymerization is related to the surface concentration of silicate. Hence at low surface concentrations only minimal quantities of silica polymers are detected (pH 4 and 6 100 μM silicate, Table 1-1), and the majority of the adsorbed silicate is primarily associated with surface functional groups (Fe-O-Si) and not polymers as evidenced by peak max between 950-1000 cm^{-1}. The 1000 μM data suggests a change in the silicate surface speciation with time. Initially, silicate is associated with surface functional groups, but as polymerization occurs some of the silica appears to desorb from the goethite surface without being released into the bulk solution. This can be readily seen through the decrease in the intensity of the Fe-O-Si and Si-OH peaks and an increase in the intensity of the Si-O-Si peaks between 6 and 48 h (Figure 1-4 and 1-5). Desorption of the silicate from surface functional groups may have contributed to the lack of a larger reduction in the arsenite rate coefficients and the lack of a 1:1 stoichiometry exhibited for arsenite adsorption and silicate desorption.

Competitive Arsenite Desorption

Silicate irreversibly displaced/desorbed previously equilibrated arsenite adsorbed to goethite (Table 1-3). Desorption of arsenite occurred at total oxyanion concentrations less than

the adsorption max for goethite, indicating competitive displacement of arsenite. The quantity of arsenite desorbed was more closely related to the initial silicate solution concentration than the total quantity of arsenite adsorbed (Table 1-3 and 1- 6). The kinetic analysis of the rate data for arsenite desorption was done with out the inclusion of a y-intercept in the Mitscherlich equation, due to the ability to describe desorption data from t = 0-3000 min (Figure 1-6). The calculated rate coefficients increased with increasing silicate concentrations. The ratio of silicate molecules adsorbed to arsenite molecules desorbed was close to 100 and 50 for 100 and 1000 μM silicate. This combined with the increasing rate coefficient suggests that the arsenite desorption mechanism is related to a mass action phenomenon with respect to silicate solution concentration. Arsenite desorption rate coefficients were 1 to 2 orders of magnitude smaller for desorption than adsorption data, even with the inclusion of a y-intercept. The large difference in relative magnitude of each rate coefficient indicates the stability of the adsorbed arsenite. The 100 μM arsenite and 1000 μM silicate adsorption scenario yielded the largest quantity (8%) of arsenite desorbed. In all other experiments the quantity of arsenite desorbed was 5% or less. From a strictly sorption perspective silicate desorbs only minor amounts of arsenite from goethite. However, the same implications discussed in the Competitive Adsorption section apply: small changes in the total quantity of arsenite adsorbed leads to significant increases in aqueous arsenite concentrations (Table 1-3). The significance of the ability of silicate to irreversibly displace adsorbed arsenite at surface coverage's below saturation is most evident when geochemical processes are at steady state. Under these conditions, arsenite is sequestered by iron oxides and not readily bioavailable. The introduction of 3 mg L^{-1} (~100 μM) of silica in groundwater or surface waters will irreversibility desorb a portion of the sequestered arsenite elevating aqueous arsenite concentrations. The quantity of arsenite released will be dependent on the quantity of arsenite adsorbed, Table 1-3, but will likely exceed 10 μg L^{-1} if the initial arsenite concentration was greater that 3.7 mg L^{-1} (50 μM).

ENVIRONMENTAL IMPACTS

The current research demonstrates that environmentally relevant concentrations of silicate reduce the rate and total quantity of arsenic adsorbed on goethite. The reduction in rate and total quantity adsorbed results in a large initial increase in reactive (aqueous) arsenite during the initial uptake and a decrease in total arsenite sequestered. The presence of silicate polymers on the goethite surface were positively identified with FTIR spectroscopy. Silicate polymers did not significantly impact arsenite adsorption rates or the total quantity of arsenite adsorbed as compared to monomers. The similarity in adsorption rates seems to be related to desorption of silicate from the surface during silicate polymer growth—thereby increasing the number of reactive surface sites for adsorption. Low concentration of silicate (100 μM; 2.7 mg L^{-1}) results in minimal arsenite desorption. Increasing silicate concentrations result in increased arsenite desorption suggesting a mass action mechanism as compared to a competitive adsorption mechanism with increasing silicate concentrations. Our data indicate the importance of anion displacement as a mechanism controlling arsenite uptake and release.

The importance of this becomes apparent in oxic, low (bi)carbonate concentration environments where sequestration by iron oxides is the primary mechanism for arsenite uptake. This is due to the ability of silicate to block arsenite adsorption sites and promote arsenite desorption at surface coverage's below saturation. Environments having these chemical conditions exist in many parts of the Ganges-Brahmaputra river basin in the form of shallow oxic

wells (Chowdhury et al., 2000). Historically ground water extracted from areas with abundant iron oxides was deemed safe for drinking water purposes. However, many of the wells are becoming progressively contaminated with arsenic due to excessive groundwater withdrawal (Singh, 2006). The reason for the emergence of arsenic is not well understood but might be related to anion displacement based on our experimental work and field data collected by Chowdhury et al. (2000) and Singh (2006). The continual supply of silicate fostered by silicate mineral weathering dissolution is a likely candidate or contributing factor in promoting arsenite desorption and reducing adsorption rates.

TABLES

Table 1-1Results from the non-linear regression of the Mitcherlich equation for arsenite and silicate adsorption on goethite. All regression results had a modified R^2 value of 0.95 or above and were significant at $\alpha = 0.01$. The (+/-) heading indicates the error estimate calculated for each parameter used in the non-linear regression.

Oxyanion	Initial Conc. (μM)	pH	C_1 (μmol m^{-2})	+/-	a (μmol m^{-2})	+/-	k (min^{-1})	+/-	Total Sorbed (μmol m^{-2})
Arsenite	50	4	0.624	0.003	0.035	0.002	0.0610	0.0095	0.66
		6	0.630	0.005	0.032	0.005	0.0810	0.0102	0.66
		8	0.655	0.007	0.010	0.007	0.1000	0.0030	0.67
Arsenite	100	4	0.880	0.007	0.189	0.006	0.0500	0.0030	1.08
		6	0.972	0.011	0.115	0.010	0.0676	0.0086	1.09
		8	1.010	0.013	0.096	0.013	0.0830	0.0160	1.11
Silicate	100	4	0.344	0.004	0.450	0.005	0.0015	0.0001	0.81
		6	0.286	0.004	0.610	0.005	0.0027	0.0001	1.00
		8	0.350	0.010	0.631	0.011	0.0085	0.0004	1.00
Silicate	1000	4	1.233	0.062	1.004	0.068	0.0047	0.0015	2.33
		6	1.305	0.096	1.323	0.110	0.0050	0.0015	2.72
		8	1.856	0.121	1.425	0.148	0.0055	0.0019	3.31

Table 1-2 Results from the non-linear regression of the Mitcherlich equation for arsenite adsorption after equilibration of silicate. All regression results had a modified R^2 value of 0.95 or above and were significant at $\alpha = 0.01$. The (+/-) heading indicates the error estimate calculated for each parameter used in the non-linear regression.

Arsenite (μM)	Silicate (μM)	pH	C_1 (μmol m^{-2})	+/-	a (μmol m^{-2})	+/-	k (min^{-1})	+/-	Total Sorbed (μmol m^{-2})	Increase in Final As(III) (μg)
50	100	4	0.595	0.004	0.077	0.004	0.0488	0.0048	0.66	10
		6	0.619	0.004	0.062	0.003	0.0482	0.0042	0.66	11
		8	0.633	0.003	0.045	0.003	0.0470	0.0072	0.67	11
	1000	4	0.523	0.004	0.083	0.004	0.0315	0.0027	0.61	267
		6	0.512	0.005	0.088	0.005	0.0274	0.0028	0.61	284
		8	0.505	0.003	0.085	0.003	0.0270	0.0020	0.59	410
100	100	4	0.510	0.028	0.200	0.028	0.0280	0.0066	0.98	487
		6	0.806	0.013	0.226	0.012	0.0296	0.0033	1.05	202
		8	0.778	0.015	0.251	0.014	0.0302	0.0034	1.04	360
	1000	4	0.425	0.006	0.269	0.006	0.0207	0.0011	0.70	2018
		6	0.277	0.015	0.377	0.015	0.0182	0.0022	0.72	2007
		8	0.331	0.020	0.366	0.020	0.0241	0.0022	0.69	2275

Table 1-3 Results from the non-linear regression of the Mitcherlich equation for arsenite desorption during silicate adsorption. All regression results had a modified R^2 value of 0.95 or above and were significant at α = 0.01. The (+/-) heading indicates the error estimate calculated for each parameter used in the non-linear regression.

Arsenite (μM)	Silicate (μM)	pH	a (μM)	+/-	k (min^{-1})	+/-	Arsenite Released (μg L^{-1})
50	100	4	0.149	0.016	$1.5*10^{-4}$	$3.0*10^{-4}$	16
		6	0.208	0.028	$3.0*10^{-4}$	$4.0*10^{-4}$	9
		8	0.236	0.037	$3.3*10^{-4}$	$1.2*10^{-4}$	18
	1000	4	3.675	0.311	$3.1*10^{-4}$	$3.0*10^{-4}$	252
		6	3.933	0.092	$7.4*10^{-4}$	$5.0*10^{-4}$	307
		8	4.094	0.080	$1.1*10^{-3}$	$2.0*10^{-4}$	310
100	100	4	1.538	0.039	$4.8*10^{-4}$	$2.0*10^{-4}$	121
		6	0.879	0.066	$3.0*10^{-4}$	$2.0*10^{-4}$	70
		8	0.975	0.051	$5.1*10^{-4}$	$3.0*10^{-4}$	71
	1000	4	0.828	0.083	$1.5*10^{-3}$	$1.2*10^{-4}$	274
		8	0.799	0.172	$1.6*10^{-3}$	$1.1*10^{-4}$	630

FIGURES

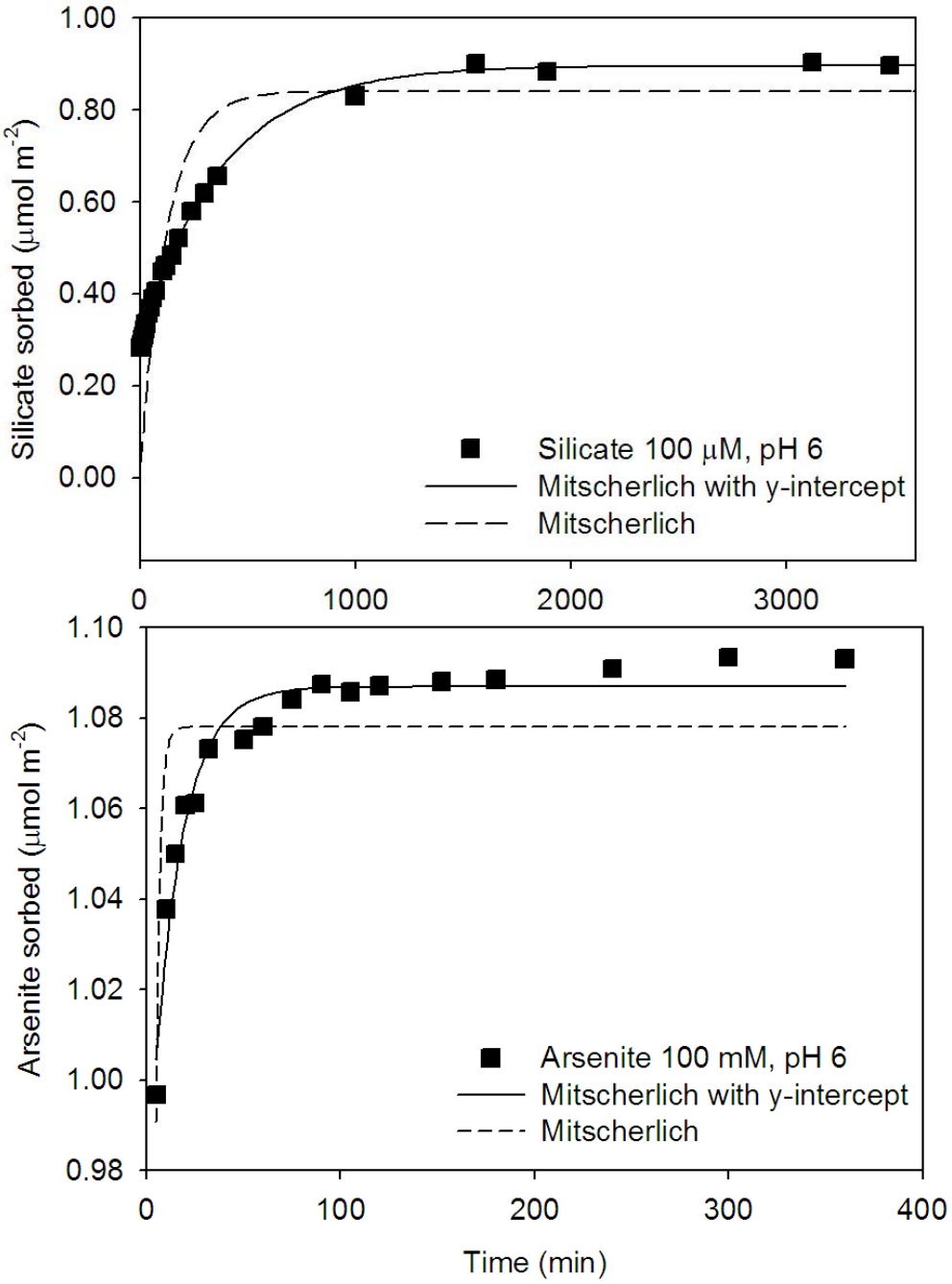

Figure 1-1 Arsenite and silicate adsorption on goethite at pH 6 and initial oxyanion solution concentration of 100μM. Symbols represent experimental data, and the lines represent the results of the nonlinear regression of the Mitscherlich equation with and without the inclusion of a y-intercept.

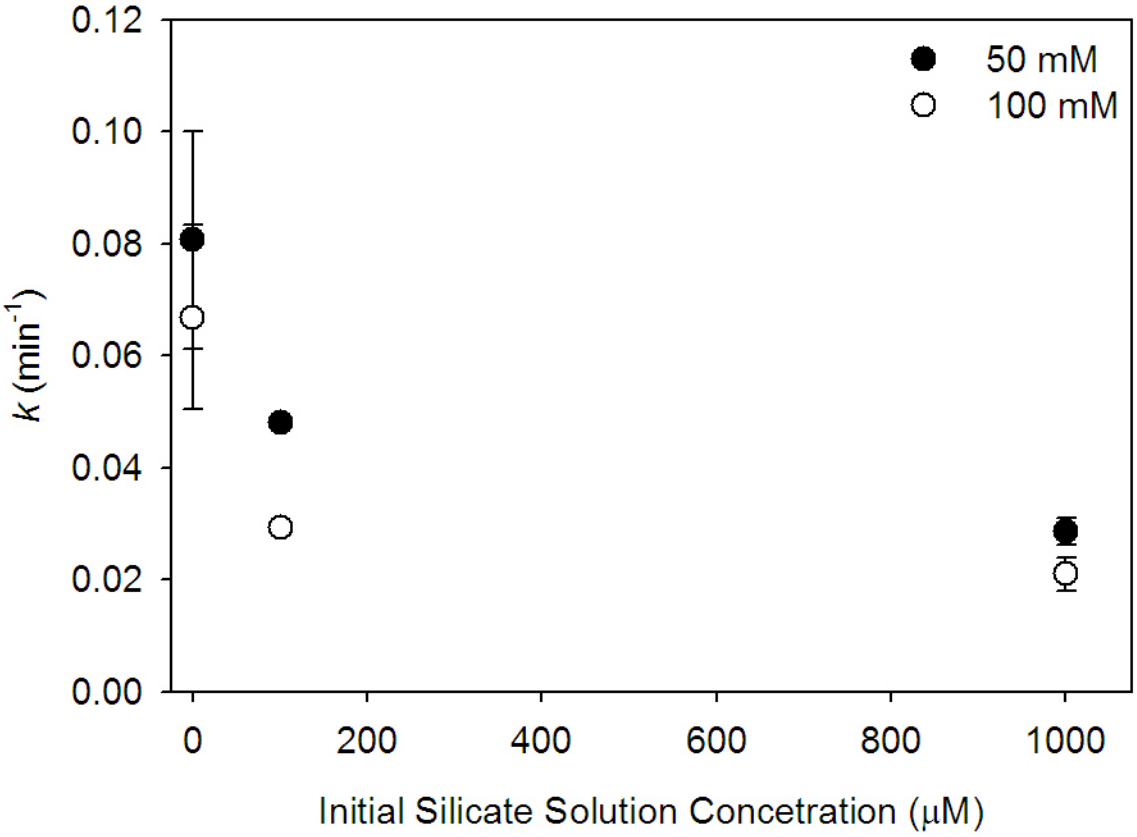

Figure 1-2 The influence of silicate on the adsorption rate coefficient of arsenite calculated from the modified Mitscherlich equation. The plotted rate coefficients are equal to the average of the values for pH 4, 6, and 8. The error bars represent the difference between the least and greatest values.

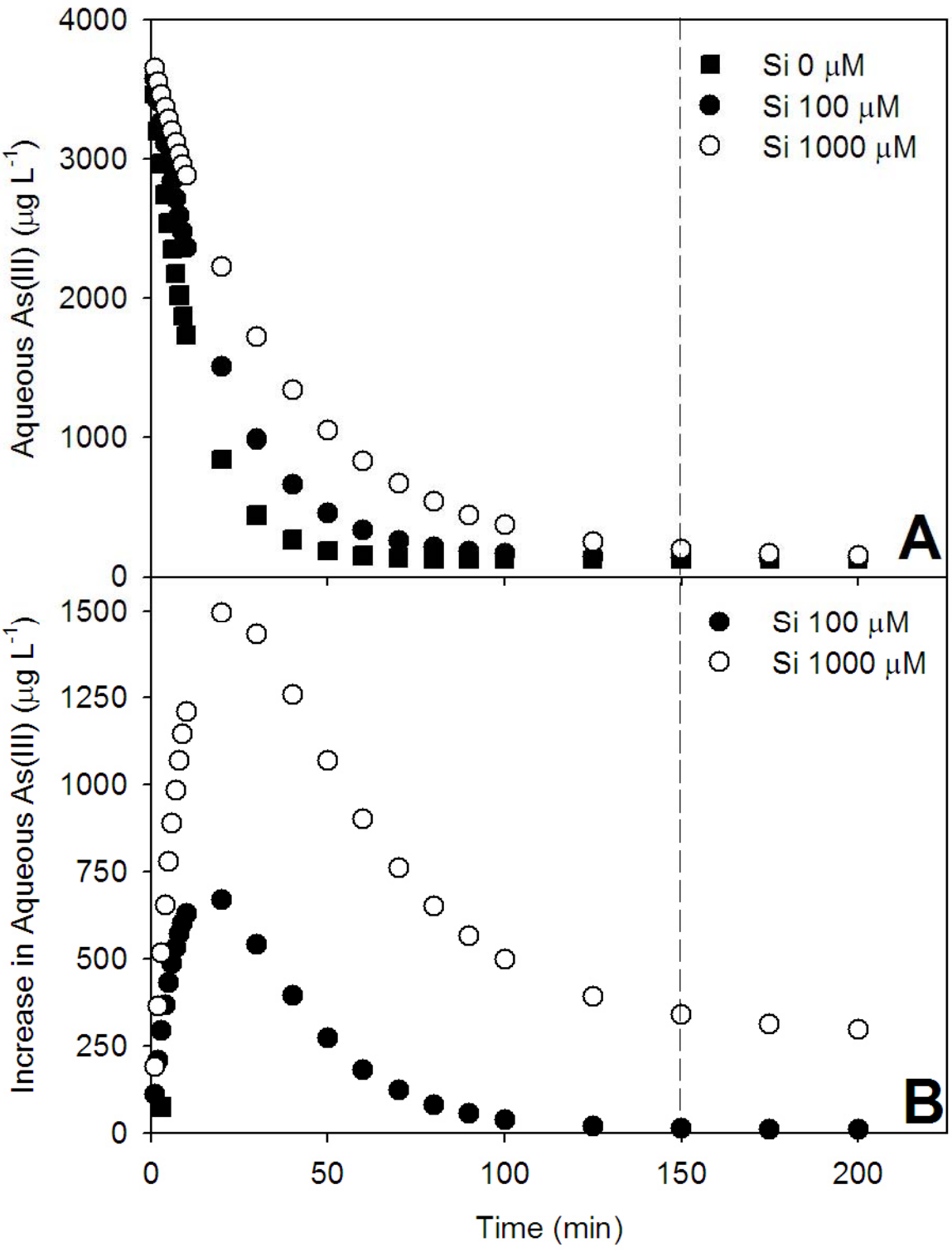

Figure1-3 Changes in arsenite solution concentration as a function of time during adsorption for 50 μM arsenite at pH 6. A) **Aqueous arsenite concentration (μg L^{-1}) for arsenite adsorption alone and in the presence of 100 and 1000 μM silicate.** B) **The increase in aqueous arsenite in the presence of silicate, data obtained from subtracting the aqueous concentration of arsenite in the presence of silicate from arsenite alone at specific time intervals.**

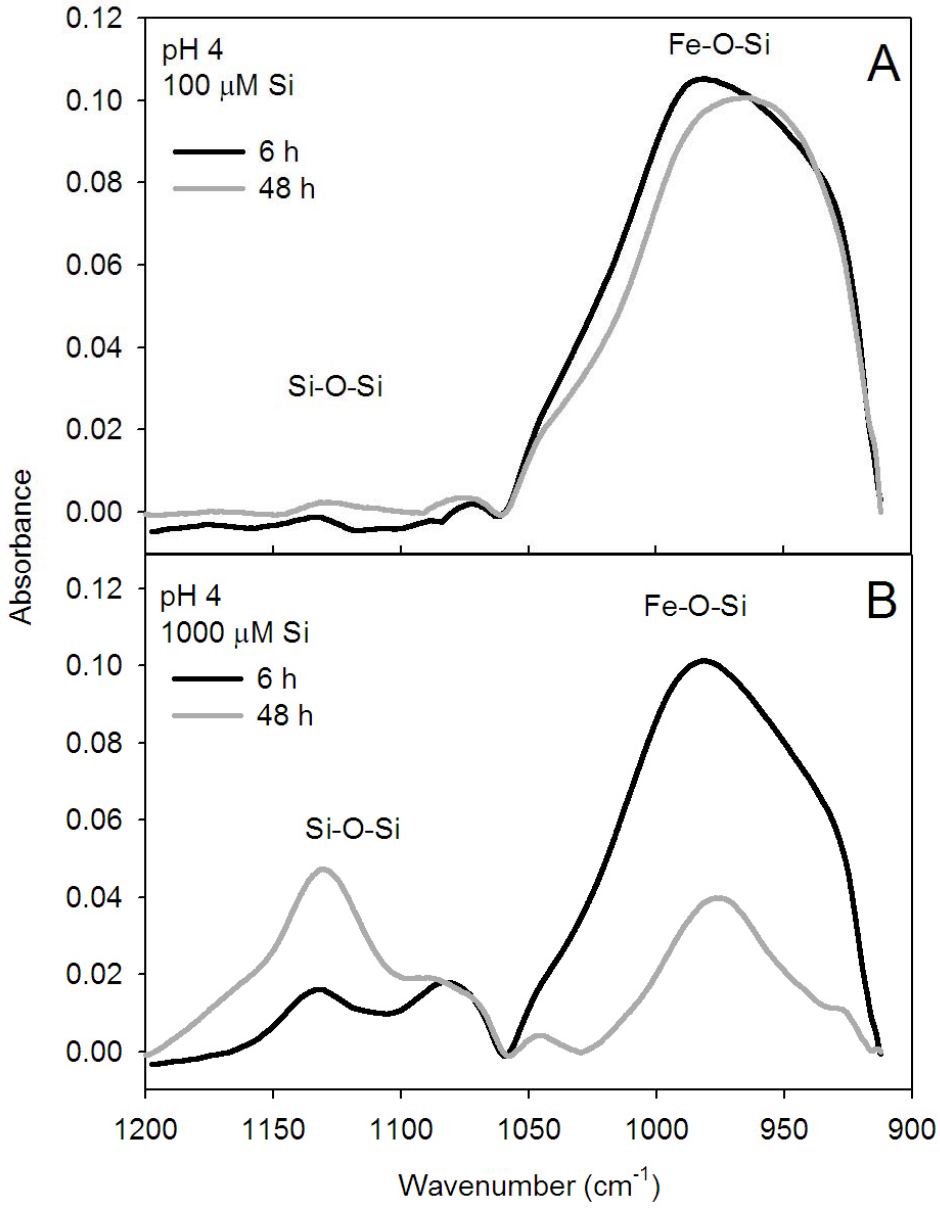

Figure 1-4 FTIR spectra of silicate adsorbed on goethite after 6 and 48 hours at pH 4; A) Initial silicate concentration 100 μM and B) initial silicate concentration 1000 μM

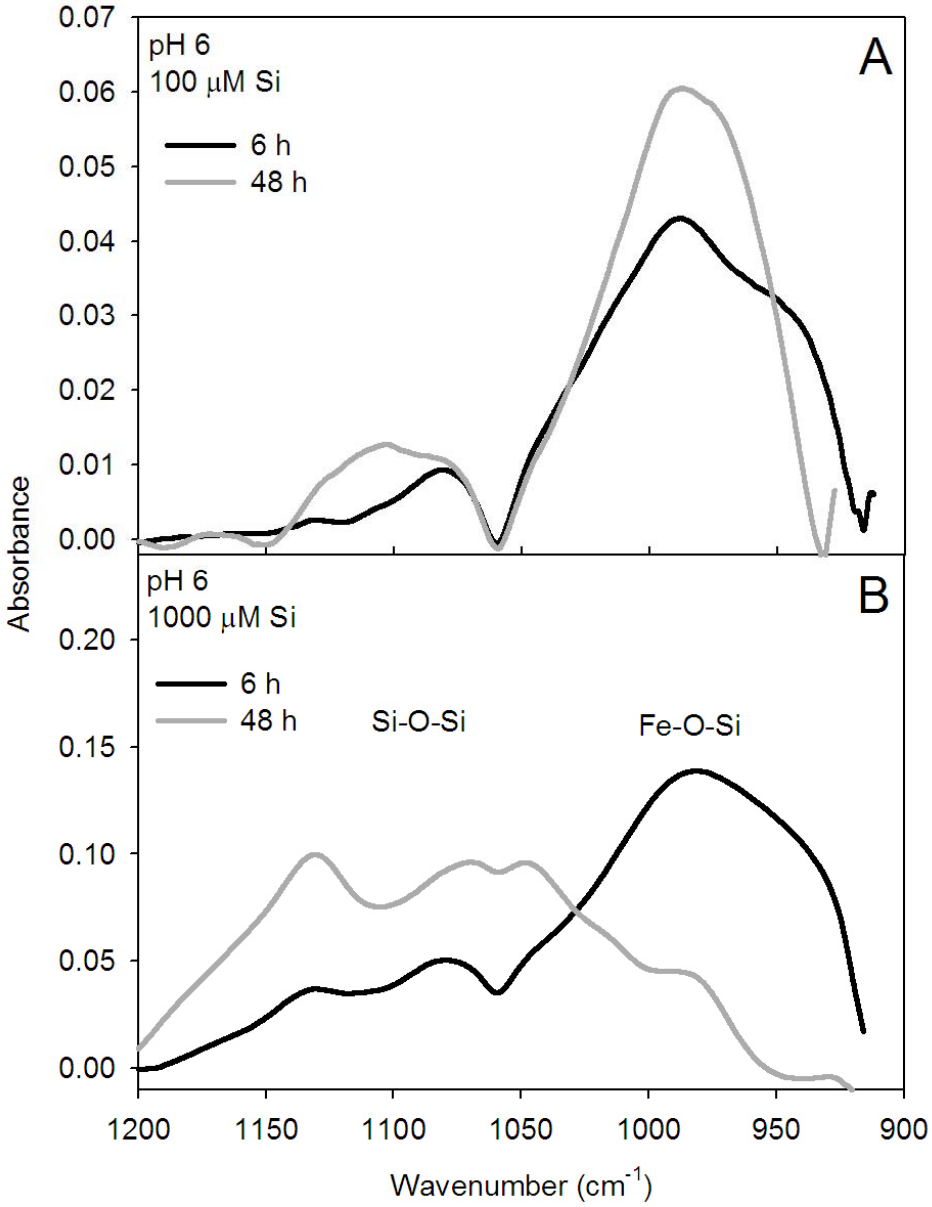

Figure 1-5 FTIR spectra of silicate adsorbed on goethite after 6 and 48 hours at pH 6; A) Initial silicate concentration 100 μM and B) initial silicate concentration 1000 μM

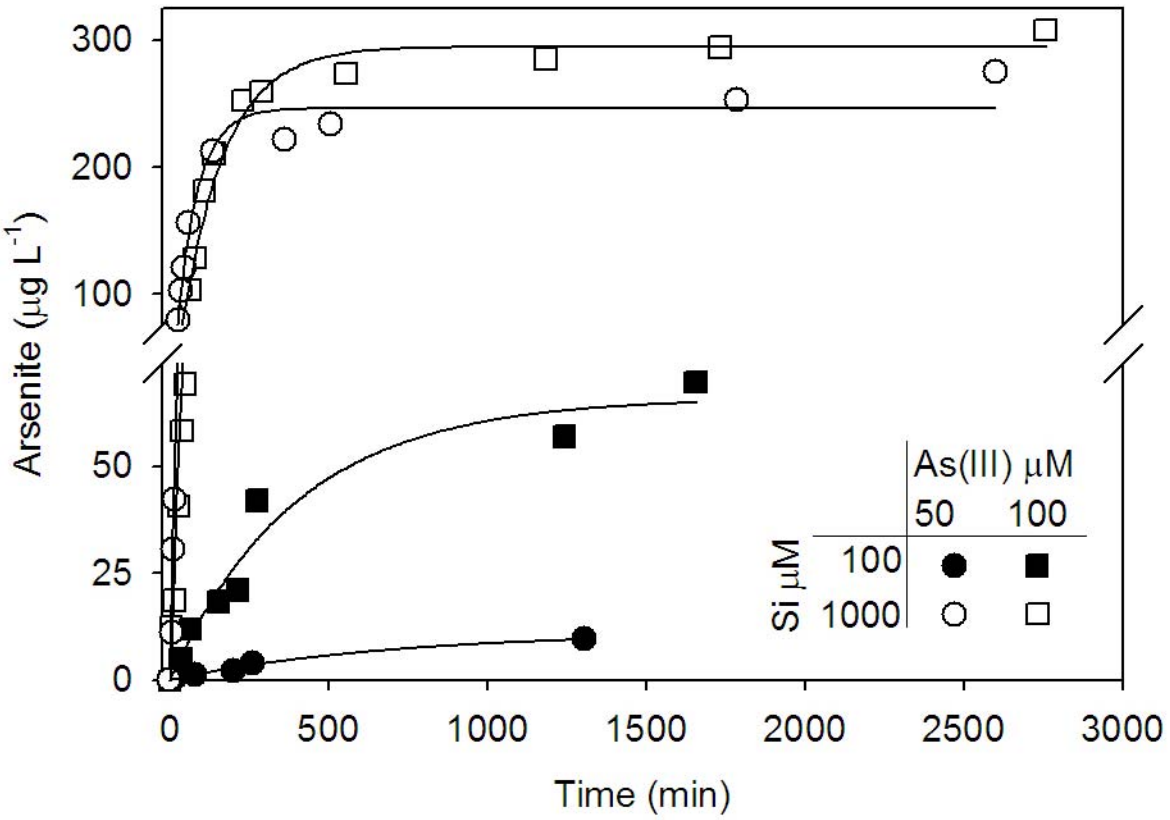

Figure 1-6 Arsenite desorption during silicate adsorption. Symbols represent experimental data, and the lines represent the results of the nonlinear regression of the Mitscherlich equation without the inclusion of a y-intercept. The plotted data is from the pH 6 experiments except for 100 μM arsenite and 1000 μM silicate, pH 4 data. Data breaks from 74 to 76 μg L^{-1} arsenite. A break in the y-axis was included to increases the resolution of the 100 μM data. Values between 74.5 and 77.5 were omitted.

REFERENCES

Acharyya S. K. and Shah B. A. (2007) Arsenic-contaminated groundwater from parts of Damodar fan-delta and west of Bhagirathi River, West Bengal, India: influence of fluvial geomorphology and Quaternary morphostratigraphy. *Environmental Geology* **52**(3), 489-501.

Aggett J. and Roberts L. S. (1986) Insight into the mechanism of accumulation of arsenate and phosphate in hydro lake sediments by measuring the rate of dissolution with ethylenediaminetraactic acid. *Environmental Science and Technology* **20**, 183-186.

Alverez R. and Sparks D. L. (1985) Polymerization of silicate anions in solutions at low concentrations. *Nature* **318**(6047), 649-651.

Anawar H. M., Akai J., and Sakugawa H. (2004) Mobilization of arsenic from subsurface sediments by effect of bicarbonate ions in groundwater. *Chemosphere* **54**(6), 753-762.

Appelo C. A. J., Van der Weiden M. J. J., Tournassat C., and Charlet L. (2002) Surface complexation of ferrous iron and carbonate on ferrihydrite and the mobilization of arsenic. *Environmental Science & Technology* **36**(14), 3096-3103.

Applin K. R. (1987) The diffusion of dissolved silica in dilute aqueous solution. *Geochimica et Cosmochimica* **51**, 2147-2151.

Arai Y., Elzinga E. J., and Sparks D. L. (2001) X-ray absorption spectroscopic investigation of arsenite and arsenate adsorption at the aluminum oxide-water interface. *Journal of Colloid and Interface Science* **235**, 80-88.

Bang S., Johnson M. D., Korfiatis G. P., and Meng X. G. (2005) Chemical reactions between arsenic and zero-valent iron in water. *Water Research* **39**(5), 763-770.

Barrón V. and Torrent J. (1996) Surface hydroxyl configuration of various crystal faces of hematite and goethite. *Journal of Colloid and Interface Science* **177**, 407-410.

Black C. A. (1993) *Soil Fertility Evaluation and Control*. Lewis Publishers.

Brown G. E., Jr., Parks G. A. (2002) Metal ion sorption processes in the marine environment; an old subject revisited. In *Geochimica et Cosmochimica Acta*, Vol. 66, pp. 106.

Chaneac C., Tronc E., and Jolivet J. P. (1996) Magnetic iron oxide-silica nanocomposites. Synthesis and characterization. **6**(12), 1905-1911.

Chowdhury T. R., Basu G. K., Mandal B. K., Biswas B. K., Samanta G., Chowdhury U. K., Chanda C. R., Lodh D., LalRoy S., Saha K. C., Roy S., Kabir S., Quamruzzaman Q., and Chakraborti D. (2000) Arsenic poisoning in the Ganges delta (vol 401, pg 545, 1999). *Nature* **404**(6773), 36-36.

Costa M. C., do Rego A. M. B., and Abrantes L. M. (2002) Characterization of a natural and an electro-oxidized arsenopyrite: a study on electrochemical and X-ray photoelectron spectroscopy. *International Journal of Mining and Processing* **65**(2), 83-108.

Darland J. E. and Inskeep W. P. (1997) Effects of pH and phosphate competition on the transport of arsenate. *Journal of Environmental Quality* **26**(4), 1133-1139.

Della Volpe C., Dire S., and Pagani E. (1997) A comparative analysis of surface structure and surface tension of hybrid silica films. **209**(1-2), 51-60.

Devitre R., Belzile N., and Tessier A. (1991) Speciation and Adsorption of Arsenic on Diagenetic Iron Oxyhydroxides. *Limnology and Oceanography* **36**(7), 1480-1485.

Dixit S. and Hering J. G. (2006) Sorption of Fe(II) and As(III) on goethite in single- and dual-sorbate systems. *Chemical Geology* **228**(1-3), 6-15.

Doelsch E., Masion A., Rose J., Stone W. E. E., Bottero J. Y., and Bertsch P. M. (2003) Chemistry and structure of colloids obtained by hydrolysis of Fe(III) in the presence of SiO_4 ligands. *Colloids and Surfaces a-Physicochemical and Engineering Aspects* **217**(1-3), 121-128.

Doelsch E., Stone W. E. E., Petit S., Masion A., Rose J., Bottero J. Y., and Nahon D. (2001) Speciation and crystal chemistry of Fe(III) chloride hydrolyzed in the presence of SiO_4 ligands. 2. Characterization of Si-Fe aggregates by FTIR and Si-29 solid-state NMR. *Langmuir* **17**(5), 1399-1405.

Gao S., Goldberg S., Herbel M. J., Chalmers A. T., Fujii R., and Tanji K. K. (2006) Sorption processes affecting arsenic solubility in oxidized surface sediments from Tulare Lake bed, California. *Chemical Geology* **228**(1-3), 33-43.

Garman S., Eick M. J., and Luxton T. P. (2004) Kinetics of chromate adsorption on goethite in the presence of sorbed silicic acid. *Journal of Environmental Quality* **33**(1703-1708).

Geelhoed J. S., Hiemstra T., and van Riemsdijk W. H. (1997) Phosphate and sulfate adsorption of goethite: Single anion and competitive adsorption. *Geochimica et Cosmochimica Acta* **61**, 2389-2396.

Goldberg S. and Johnston C. (2001) Mechanisms of arsenic adsorption on amorphous oxides evaluated using macroscopic measurements, vibrational spectroscopy, and surface complexation modeling. *Journal of Colloid and Interface Science* **234**, 204-216.

Grafe M., Eick M. J., and Grossl P. R. (2001) Adsorption of arsenate (V) and arsenite (III) on goethite in the presence and absence of dissolved organic carbon. *Soil Science Society of America Journal* **65**, 1680-1687.

Grafe M., Eick M. J., Grossl P. R., and Saunders A. M. (2002) Adsorption of arsenate and arsenite on ferrihydrite in the presence and absence of dissolved organic carbon. *Journal of Environmental Quality* **31**, 1115-1123.

Grossl P. R., Eick M., Sparks D. L., Goldberg S., and Ainsworth C. C. (1997) Arsenate and chromate retention mechanisms on goethite 2. Kinetic evaluation using a pressure-jump relaxation technique. *Environmental Science & Technology* **31**(2), 321-326.

Grossl P. R. and Sparks D. L. (1995) Evaluation for Contaminant Ion Adsorption-Desorption on Goethite Using Pressure-Jump Relaxation Kinetics. *Geoderma* **67**(1-2), 87-101.

Hansen H. C. B., Rabenlange B., Raulundrasmussen K., and Borggaard O. K. (1994a) Monosilicate adsorption by ferrihydrite and goethite at pH 3-6. *Soil Science* **158**(1), 40-46.

Hansen H. C. B., Wetche T. P., Raulund-Rasmussen K., and Borggaard O. K. (1994b) Stability constants for silicate adsorbed to ferrihydrite. *Clay Minerals* **29**, 341-350.

Hiemstra T. and van Riemsdijk W. H. (1996) A surface structural approach to ion adsorption: the charge distribution (CD) model. *Journal of Colloid and Interface Science* **179**, 488-508.

Hochella, Jr M. F. J. (1990) Atomic structure, microtopography, composition, and reactivity of mineral surfaces. In *Mineral-Water Interface geochemistry*, Vol. 23 (ed. M. F. Hochella, Jr and A. F. White). Mineralogical Society of America.

Iler R. K. (1979) *The Chemistry of Silica*. Jon Wiley & Sons.

Inskeep W. P., McDermott T. R., and Fendorf S. E. (2002) As(V)/(III) cycling in soils and natural waters: chemical and microbiological processes. In *Environmental Chemistry of Arsenic* (ed. W. T. Frankenberger). Marcel Dekker, Inc.

Lasaga A. C. (1998) *Kinetic Theory in the Earth Sciences*. Princeton University Press, Princeton, NJ.

Lasaga A. C. and Kirkpatrick R. J. (1981) Kinetics of Geochemical Processes. In *Reviews in Mineralogy*, Vol. 8 (ed. P. H. Ribbe), pp. 398. Mineralogical Society of America.

Liu F., De Cristofaro A., and Violante A. (2001) Effect of pH, phosphate and oxalate on the adsorption/desorption of arsenate on/from goethite. *Soil Science* **166**(3), 197-208.

Loeppert R. L. and Inskeep W. P. (1996) Iron. In *Methods of Soil Analysis, Part 3. SSSA Book Ser. No. 5.* (ed. D. L. Sparks), pp. 639-664. SSSA.

Luxton T. P. (2007) Oxyanion Adsorption on Ruthenium and Iron Oxides. Dissertation, Virginia Tech.

Luxton T. P. and Eick M. (2004) Modeling arsenite and silicic acid adsorption on goethite using the CD MUSIC surface complexation model. *Annual Meeting of the Soil Science Society of America*.

Luxton T. R., Tadanier C. J., and Eick M. J. (2006) Mobilization of arsenite by competitive interaction with silicic acid. *Soil Science Society of America Journal* **70**(1), 204-214.

Mackay A. D., Syers J. K., Tillman R. W., and Gregg P. E. H. (1986) A Simple-Model to Describe the Dissolution of Phosphate Rock in Soils. *Soil Science Society of America Journal* **50**(2), 291-296.

Mahoney J., Langmuir D., Gosselin N., and Rowson J. (2005) Arsenic readily released to pore waters from buried mill tailings. *Applied Geochemistry* **20**(5), 947-959.

McBride M. B. (1994) *Environmental Chemistry of Soils*. Oxford Press.

McPhail M., Page A. L., and Bingham F. T. (1972) Adsorption interactions of monosilicic and boric acid on hydrous oxides of iron and aluminum. *Soil Science society of America Proceedings* **36**, 510-514.

Meng X. G., Bang S., and Korfiatis G. P. (2000) Effects of silicate, sulfate, and carbonate on arsenic removal by ferric chloride. *Water Research* **34**(4), 1255-1261.

Mitscherlich E. A. (1909) Das Gesetz des Minimums und das Gesetz des abnehmendon Bodenertrages. *Landwritschaftliche Jahrbucher* **38**(537-552).

Mul G., Hamminga G. M., and Moulijn J. A. (2004) Operando ATR-FTIR analysis of liquid-phase catalytic reactions: can heterogeneous catalysts be observed? *Vibrational Spectroscopy* **34**(1), 109-121.

National Institute of Standards and Technology U. S. (2002) NIST X-ray Photoelectron Spectroscopy Database: version 2.0, Vol. 2004. National Institute of Science and Technology.

Nesbitt H. W., Muir L. J., and Pratt A. R. (1995) Oxidation of arsenopyrite by air and air-saturated, distilled water, and implications for mechanism of oxidation. *Geochimica et Cosmochimica Acta* **59**(9), 1773-1786.

Nickson R. T., McArthur J. M., Ravenscroft P., Burgess W. C., and Ahmed K. M. (2000) Mechanism of arsenic release to groundwater, Bangladesh and West Bengel. *Applied Geochemistry* **15**, 403-413.

Nordstrom D. K. (2002) Public health - Worldwide occurrences of arsenic in ground water. *Science* **296**(5576), 2143-2145.

Oscarson D. W., Huang P. M., Defosse C., and Herbillon A. (1981) Oxidative Power of Mn(IV) and Fe(III) Oxides with Respect to As(III) in Terrestrial and Aquatic Environments. *Nature* **291**(5810), 50-51.

Oscarson D. W., Huang P. M., and Liaw W. K. (1980) The Oxidation of Arsenite by Aquatic Sediments. *Journal of Environmental Quality* **9**(4), 700-703.

Pantsar K. M. and Manninen P. K. G. (1997) Speciation of mobile arsenic in soil samples as a function of pH. *Science of the Total Environment* **204**(2), 193-200.

Parfitt R. L., Vandergaast S. J., and Childs C. W. (1992) A Structural Model for Natural Siliceous Ferrihydrite. *Clays and Clay Minerals* **40**(6), 675-681.

Polizzotto M. L., Harvey C. F., Li G. C., Badruzzman B., Ali A., Newville M., Sutton S., and Fendorf S. (2006) Solid-phases and desorption processes of arsenic within Bangladesh sediments. *Chemical Geology* **228**(1-3), 97-111.

Polizzotto M. L., Harvey C. F., Sutton S. R., and Fendorf S. (2005) Processes conducive to the release and transport of arsenic into aquifers of Bangladesh. *Proceedings of the National Academy of Sciences of the United States of America* **102**(52), 18819-18823.

Raven K. P., Jain A., and Loeppert R. H. (1998) Arsenite and arsenate adsorption on ferrihydrite: Kinetics, equilibrium, and adsorption envelopes. *Environmental Science & Technology* **32**(3), 344-349.

Redman A. D., Macalady D. L., and Ahmann D. (2002) Natural organic matter affects arsenic speciation and sorption onto hematite. *Environmental Science & Technology* **36**(13), 2889-2896.

Schwertmann U. and Cornell R. M. (1991) *Iron Oxides in the Laboratory: Preparation and Characterization*. VCH.

Schwertmann U. and Cornell R. M. (1996) *The Iron Oxides: Structures, Properties, Reactions, Occurrences and Uses*. VCH.

Sigg L. and Stumm W. (1981) The interaction of anions and weak acids with the hydrous goethite (α-FeOOH) surface. *Colloids and Surfaces* **2**, 101-117.

Singh A. K. (2006) Chemistry of arsenic in groundwater of Ganges-Brahmaputra river basin. *Current Science* **91**(5), 599-606.

Smedley P. L. and Kinniburgh D. G. (2002) A review of the source, behavior and distribution of arsenic in natural waters. *Applied Geochemistry* **17**(5), 517-568.

Smedley P. L., Nicolli H. B., Macdonald D. M. J., Barros A. J., and Tullio J. O. (2002) Hydrogeochemistry of arsenic and other inorganic constituents in groundwaters from La Pampa, Argentina. *Applied Geochemistry* **17**(3), 259-284.

Smith A. H., Lopipero P. A., Bates M. N., and Steinmaus C. M. (2002a) Public health - Arsenic epidemiology and drinking water standards. *Science* **296**(5576), 2145-2146.

Smith E., Naidu R., and Alston A. M. (2002b) Chemistry of inorganic arsenic in soils: II. Effect of phosphorus, sodium, and calcium on arsenic sorption. *Journal of Environmental Quality* **31**, 557-563.

Sparks D. L. (2003) *Environmental Soil Chemistry*. Academic Press.

Sparks D. L., Fendorf S. E., V. T. I. C., and Carski T. H. (1996) Kinetic Methods and Measurements. In *Methods of Soil Analysis Part 3 Chemical Methods* (ed. D. L. Sparks), pp. 1275-1307. Soil Science Society of America Inc.

Sposito G. (1989) *The Chemistry of Soils*. Oxford University Press.

Stollenwerk K. G. (2003) *Arsenic in Groundwater*. Kluwer Academic Publishers.

Sun X. H. and Doner H. E. (1998) Adsorption and oxidation of arsenite on goethite. *Soil Science* **163**(4), 278-287.

Swartz C. H., Blute N. K., Badruzzman B., Ali A., Brabander D., Jay J., Besancon J., Islam S., Hemond H. F., and Harvey C. F. (2005) Mobility of arsenic in a Bangladesh aquifer: Inferences from geochemical profiles, leaching data, and mineralogical characterization (vol 68, pg 4539, 2004). *Geochimica et Cosmochimica Acta* **69**(21), 5159-5159.

Swedlund P. J. and Webster J. G. (1999) Adsorption and polymerization of silicic acid on ferrihydrite, and its effect on arsenic adsorption. *Water Research* **33**(16), 3413-3422.

van der Marel H. W. and Beutelspacher H. (1976) *Atlas of Infrared Spectroscopy of Clay Minerals and Their Admixtures*. Elsevier Scientific Publishing.

van Green A., Zheng Y., Cheng Z., Aziz Z., Horneman A., Dhar R. K., Mailloux B., Stute M., Weinman B., Goodbred S., Seddique A. A., Hope M. A., and Ahmed K. M. (2006) A transect of groundwater and sediment properties in Araihazar, Bangladesh: Further evidence of decoupling between As and Fe mobilization. *Chemical Geology* **228**(1-3), 85-96.

Vempati R. K. and Loeppert R. H. (1989) Influence of Structural and Adsorbed Si on the Transformation of Synthetic Ferrihydrite. *Clays and Clay Minerals* **37**(3), 273-279.

Vempati R. K., Loeppert R. H., Dufner D. C., and Cocke D. L. (1990) X-ray photoelectron spectroscopy as a tool to differentiate silicon-bonding state in amorphous iron oxides. *Soil Science Society of America Journal* **54**, 695-698.

Waltham C. and Eick M. J. (2002) Kinetics of arsenic adsorption on goethite in the presence of sorbed silicic acid. *Soil Science Society of America* **66**(3), 818-825.

Welch A. H., Westjohn D. B., Helsel D. R., and Wanty R. B. (2000) Arsenic in ground water of the United States: Occurrence and geochemistry. *Ground Water* **38**(4), 589-604.

Yampracka S., Attandndana T., Sidibe-Diarra A., Srivihok A., and Yost R. S. (2006) Predicting the dissolution of four rock phosphates in flooded acid sulfate soils of Thailand. *Soil Science* **171**(3), 200-209.

CHARACTERIZATION AND DISSOLUTION PROPERTIES OF RUTHENIUM OXIDES

ABSTRACT

Ruthenium oxides (RuO_2•$1.1H_2O$ and RuO_2) have been synthesized by forced hydrolysis and oxidation of ruthenium chloride. The resulting materials were extensively characterized to determine the crystallinity, surface area, and ruthenium oxidation state. Surface charging experiments indicate a large quantity of reactive functional groups for both materials 50 μmol m^{-2} for RuO_2•$1.1H_2O$ and 20 μmol m^{-2} for RuO_2 and a decrease in the acidity of the surface functional groups with crystallization of the hydrous oxide. Dissolution studies conducted in acidic and basic pH environments indicate Ru-oxides are insoluble in 0.1 M HCl and slightly soluble in 0.1 M NaOH. Oxalate and ascorbate (5 mM) promoted dissolution of RuO_2•$1.1H_2O$ over the pH range investigated (3-8). Dissolution rates increased with decreasing pH and ligand surface coverage. XPS analysis of the RuO_2•$1.1H_2O$ surface after ligand promoted dissolution revealed the reduction of Ru(IV) to Ru(III) indicating that both ascorbate and oxalate reductively dissolve RuO_2•$1.1H_2O$. Dissolution experiments with RuO_2 resulted in dissolution only for 5 mM oxalate at pH 3. At all other pH values investigated and in the presence of ascorbate there was no increase in dissolved Ru concentration as a function of time. Dissolution rates calculated for RuO_2•$1.1H_2O$ and RuO_2 are compared with previously published dissolution rates for iron oxides, demonstrating an order of magnitude decrease in the oxalate and ascorbate promoted dissolution.

INTRODUCTION

Ruthenium oxides (RuO_2•xH_2O and RuO_2) have been extensively used in industrial and research applications as eletrocatalysts for chlorine, oxygen, and hydrogen gas production; oxidation of carbon monoxide; ferroelectric memory devices (hard drives), and synthesis of a variety of organic chemicals (Over et al., 2000; Trasatti, 1992; Trasatti, 1994). More recently, ruthenium oxides have been investigated as potential chemical batteries due to the minimal energy requirements and oxide stability during proton diffusion into the crystal structure (Fu et al., 2002; Galizzioli et al., 1974; McKeown et al., 1999; Trasatti and Buzzanca, 1971; Zheng et al., 1995). Adding to the list of ruthenium oxide applications, Impellitteri et al. (2003) and Scheckel et al. (2004) have evaluated RuO_2•xH_2O as a potential metal oxide sorbent material for water treatment applications. The two studies focused on the high sorption capacity of Pb and As (1g Pb and 0.15 g As(III) g^{-1} Ru) and the complete rapid oxidation of arsenite (AsO_3^{3-}) to arsenate (AsO_4^{3-}). Currently there are no other metal oxide materials being used in industrial and residential wastewater treatment with such large sorption capacities and oxidative potential. Basic research evaluating the crystal structure, morphology, surface site acidity, reactive functional group density, and dissolution behavior are critical in determining under what chemical environments ruthenium oxides could be employed as sorbent materials.

The versatility and wide range of applications associated with oxides of ruthenium has lead to a tremendous amount of research aimed at characterizing synthesis procedures, electro chemical properties, crystalline structure, and surface morphology in an effort to understand the chemical mechanisms involved in the previously mentioned applications (Basame et al., 2001; Chen et al., 1997; Froment et al., 1999; Hu and Huang, 2001; Huang and Chen, 2001; Kotz et al.,

1983; Lister et al., 2002b; Lyons and Burke, 1987; Malek et al., 1996; McKeown et al., 1999; Over et al., 2000; Panic et al., 2003; Park and Park, 2002; Raistrick and Sherman, 1987; Rard, 1985; Varshal et al., 1983; Zheng and Xin, 2002). Hydrous ruthenium oxide most commonly synthesized by forced hydrolysis and oxidation of $RuCl_3$ which results in a hydrous oxide ($RuO_2 \bullet xH_2O$) with varying amounts of coordinated water depending on the exact procedure (McKenzie and Marken, 2002; Park and Park, 2002; Zheng et al., 1995). Typically the hydrous oxide is completely amorphous in nature with no detectable x-ray or electron diffraction pattern (Hu and Huang, 2001; Long et al., 1999; Malek et al., 1996; Zheng and Huang, 2002). Heating the hydrous oxide to temperatures greater than 300^o C results in the dehydration of the solid phase and the formation of a rutile crystal structure with the chemical formula RuO_2 (Bhaskar et al., 2001; Malek et al., 1996; McKeown et al., 1999). X-ray photoelectron spectroscopy and cyclic voltammetry have both demonstrated that the two oxide phases contain Ru in mixed oxidation states (i.e. Ru (III) and (IV) in $RuO_2 \bullet xH_2O$, and Ru (III), (IV), and (VI) in RuO_2) (Bhaskar et al., 2001; Froment et al., 1999; Hrbek et al., 1995; Iembo et al., 1997; Kim et al., 2001; Kotz et al., 1983; Sunol et al., 2000; Zen et al., 2001).

Studies focusing on the acidity and chemical reactivity of ruthenium oxide functional groups and ruthenium oxide dissolution in aqueous media are less common (Lyons and Burke, 1987; Rard, 1985; Xue and Osseoasare, 1989). This information is necessary in order to evaluate Ru-oxides use as sorbent in water treatment. Hence, the objectives of the current study are to synthesize hydrous ruthenium oxide ($RuO_2 \bullet xH_2O$) via forced hydration and oxidation, and synthesize ruthenium oxide (RuO_2) by heat treatment of the hydrous phase. The resulting solid materials will be extensively characterized to determine the chemical formula for the solid material, crystalline structure, surface area and ruthenium oxidation state. The surface charging characteristics, surface acidity constants, and points of zero charge will be determined for the two materials in order to assess chemical reactivity and surface charge in the environmental pH range (3-10). Finally, dissolution studies will be conducted in the presence of hydrochloric acid, sodium hydroxide, oxalate, and ascorbate to determine the dissolution behavior of ruthenium oxides in adverse pH environments and in the presence of metal chelating ligands. Results from the current work will help to establish under what environmental conditions ruthenium oxides can be used as metal oxide sorbent materials.

MATERIALS AND METHODS

Materials

All materials used in the current study were ACS reagent grade chemicals (Fisher Scientific, Fair Lawn, NJ) unless otherwise noted. The amorphous ruthenium oxides were synthesized from the oxidation of ruthenium chloride ($RuCl_3$) (Alfa Aesar, Ward Hill, MA). The synthesis procedure was developed from the procedures published by Zheng et al.(1995) and McKenzie and Marken (2002). Briefly a 0.1 M $RuCl_3$ solution was slowly added to 500 mL of 95^o C Milli-Q water (Millipore Corp., Burlington, MA). The resulting solution was titrated with 0.5 M NaOH until precipitation began at approximately pH 6. The precipitate was allowed to settle and cool for three hours before transferring to dialysis tubing (Fisher Scientific, Fair Lawn, NJ). The ruthenium oxide precipitate was rinsed with Milli-Q water until the conductivity of the bathing solution was equal to the conductivity of an atmosphere equilibrated beaker of Milli-Q water. The precipitate was flash frozen in liquid N_2 and freeze-dried. After freeze drying, half of the amorphous ruthenium oxide material ($RuO_2 \bullet xH_2O$) was heated to 500^o C in a muffle furnace to produce a crystalline ruthenium oxide (RuO_2).

Oxide Characterization

The synthesized $RuO_2 \bullet xH_2O$ and RuO_2 were extensively characterized to determine crystallinity, crystalline water content, surface area, ruthenium oxidation state, chemical composition, surface site acidity/reactivity, and dissolution behavior. The structure of the ruthenium oxides was determined by powder x-ray diffraction (XRD) using a Scintag® XDS 2000 X-ray Diffraction Spectrophotometer (Scintag Inc., Sunnyvale, CA) with CuKα radiation and a scan rate of 0.02^o θ/min. Thermal analysis of the ruthenium oxides was performed using thermogravimetric analysis (TGA) (TA Instrument Hi-Res TGA 2950, New Castle, DE) and differential scanning calorimetry (DSC) (Dupont Instruments DSC 2910, New castle DE). For both techniques the ruthenium oxide samples were equilibrated at 308 K and heated at 10 K min^{-1} to 873 K.

The shape and crystallinity of the both oxides was evaluated by high resolution transmission electron microscopy (HRTEM) using a Titan S/TEM 80-300 X twin FEI microscope (Eindhoven, The Netherlands) at Virginia Polytechnic Institute and State University, USA. The system operated at 200 kVV with a resolution of 0.025 nm. TEM samples were prepared by evaporation of a dilute suspension of $RuO_2 \bullet xH_2O$ or RuO_2. A 0.1 μL droplet was deposited on an ultra thin carbon coated Ni mesh TEM grid and dried over night in a 40^o C oven. Fourier transforms of the HRTEM images were collected to evaluate crystallinity.

Specific surface area (SSA) of the oxides was determined by N_2 adsorption/desorption isotherms at liquid N_2 temperatures (77 K) (Micromoretics ASAP 2010 Surface Area Analyzer, Norcross, GA). Micro-pore surface area and volume was determined from t-plots constructed from the N_2 isotherms (Rouquerol et al., 1999).

Chemical composition and Ru oxidation state in the oxides were determined using X-ray photoelectron spectroscopy. XPS spectra were collected on a PerkinElmer 5400 ESCA system (Wellesley, MA). The x-ray source was monochromatic Mg Kα radiation at 1253.6 eV. Both wide and narrow scans were conducted, the former to determine range and abundance of elements present and the latter to determine the chemical state. Spectra obtained for the broad scans were collected over 10 cycles of 1 eV/step at 25 msec/step. Narrow scans were collected for 100 cycles of 0.1 eV/step at 25 msec/step. An advantageous carbon (C(1s)) peak (285.0 eV) was present in all samples and used as an internal reference. The C(1s) peak was invariant throughout each experiment and corrections for charging were not required. Binding energies for Ru and O were assigned relative to the C(1s) peak. Narrow scans for the O(1s) peak were collected from 543 to 526 eV. Narrow scans for the Ru (3p and 3d) peaks were collected from 500 to 453eV and 292 to 275eV, respectively.

Surface Charge

The charging behavior and point of zero charge of the ruthenium oxides was determined by electrophoretic mobility measurements and proton titrations. For the electrophoretic mobility measurements oxides suspensions (0.5 g L^{-1}) were prepared with 0.001, 0.01, and 0.10 M NaCl solutions in individual vials adjusted to various pH values between 3 and 11. Measurements were collected using a Malvern Zetasizer 3000HSa (Southboro, MA). Based on preliminary data and particle size, the voltage applied to the capillary cell was set at 100 mV and a Henry function ($f(K_a)$) of 1.5-1.23 was used to calculate the zeta potential. Proton titrations were conducted on

oxides suspensions (5 g L^{-1}) with 0.01, 0.05 and 0.10 M NaCl solutions. The suspension was adjusted to pH 3 with 0.17 M HCL and then titrated to pH 11 with 0.14 M NaOH. During the titrations 0.2 mL of base was added to the suspension and the pH was allowed to equilibrate for 90 sec, before the next base addition. Titrations were conducted using a Radiometer TIM 900 Titration Manager and ABU901 autoburette (Radiometer Analytical S.A., Lyon France). All titrations were carried out in a N_2 environment under positive pressure.

Dissolution Experiments

The dissolution behavior of amorphous and crystalline Ru-oxide was evaluated under acidic and basic conditions and in the presence of two organic acids. Dissolution studies evaluating the proton and hydroxyl promoted dissolution of Ru-oxides were conducted in the presence of 100 mM HCl and 100 mM NaOH. Dissolution studies involving organic acids were conducted in the presence of a 5 mM oxalic ($C_2O_4H_2$) and ascorbic ($C_6H_8O_6$) acids. Oxalate promoted dissolution studies were conducted from pH 2 to 8, and ascorbic acid studies were conducted at pH 3, 5 and 7. All experiments were conducted in duplicate at a constant ionic strength of 0.01 M NaCl using a pH monitored stirred batch reactor technique. Briefly, an appropriate quantity of N_2 sparged Ru-oxide was weighed into a 500 mL glass breaker to which 350 mL of 0.01 M NaCl was added. The suspension was dispersed for ~2 min using an ultrasonic dimembrator. The beaker was placed in a water jacketed reaction vessel kept at 25^o C, stirred at 300 rpm using a three blade impeller, and kept under positive pressure with N_2 gas to eliminate CO_2. The suspension was allowed to hydrate for a period of 24 h while the pH was adjusted to the appropriate value using a Brinkman® 716 Stat-Trino pH stat (Brinkman Instruments, Westbury, NY) with either 0.1 M HCl or NaOH. Following the 24 h hydration period the suspension was brought to volume (400 mL) minus the volume of HCl, NaOH or organic acid to be added. The acid was added from a 980 mM HCl solution of trace metal grade hydrochloric acid. The base was added from a 750 mM NaOH solution prepared with boiled and distilled CO_2 free water. Prior to the addition the NaOH solution was kept in a positive pressure N_2 environment to prevent CO_2 diffusion. Oxalic and ascorbic acid were added from a ~100 mM stock solution prepared no more than three days prior to the experiment. The concentrations of the organic acid stock solutions were determined by total organic carbon analysis using Sievers® 900 TOC Analyzer (Ionics Instruments, Boulder, CO). Sampling began immediately after the addition of acid or base and continued for 50 h. The pH of the 5 mM organic acid dissolution experiments was maintained using a pH-stat over the 50 h dissolution period. At specific time intervals a 15 mL sample was removed and filtered through a 0.22 μm Fisherbrand® (Fisher, Atlanta, GA) membrane. The resulting filtrate was analyzed for Ru and C. Ruthenium was analyzed using an inductively coupled plasma atomic emission spectrometer (ICP-AES) (SpectroFlame FTMOA85D, Spectro Analytical Instruments, Fitchburg, MA). The detection limit on the SpectroFlame ICP-AES for Ru was 10 μg L^{-1}. The concentration of organic acid in the filtrate was determined by TOC analysis followed by conversion to molar concentration of either oxalic or ascorbic acid. Dissolution rates were determined from the linear portion of the dissolution experiment using a linear empirical rate law assuming zero order reaction kinetics with respect to the solid phase (Lasaga, 1981) (Eq2-1).

$$C = C_o + k_1 t \qquad (2\text{-}1)$$

RESULTS AND DISCUSSION

Oxide Characterization

Thermal analysis of the amorphous Ru-oxide indicated three weight loss events. Two of the weight loss events correspond to an endo- and exothermic peak in the DCS data (Figure 2-1). The final weight loss event occurs near 500^{o} C and is not accompanied by a significant change in the DSC data. The largest weight loss corresponds to the endothermic peak which extends from 50^{o} to 200^{o} C is attributed to the release of structural water from the amorphous material (RuO_2•xH_2O). The second weight loss event which corresponds with the exothermic peak (225^{o} to 350^{o} C) is attributed to dehydroxylation of the amorphous material during the formation of the crystalline phase (RuO_2). The temperature at which the amorphous material undergoes crystallization is in good agreement with published data which indicates phase transformation occurs between 300 and 425^{o} C (Bhaskar et al., 2001; Malek et al., 1996; McKeown et al., 1999). The third weight loss event at approximately 500^{o} C is thought to be related to the loss of coordinated oxygen resulting in the formation of coordinately unsaturated sites (cus) on the Ru-oxide surface and oxidation of Ru(IV) to Ru(VI) (Bhaskar et al., 2001; McKeown et al., 1999; Wang et al., 2003). The percent total weight loss was used to determine the quantity of structural water associated with the amorphous Ru-oxide. The total weight loss was 13% which translates to 1.1 moles of water per mole of material, resulting in a chemical formula of RuO_2•$1.1H_2O$ for the amorphous material.

X-ray diffraction spectra of Ru-oxide annealed at various temperatures indicates that initially the Ru-oixde is amorphous with no distinguishable diffraction peaks (Figure 2-2). Upon heating the material begins to crystallize, resulting in a crystalline RuO_2 phase with a rutile structure. All of the peaks positions in the 500^{o} C RuO_2 spectrum were well correlated with the International Center for Diffraction Files (01-071-4825, Newton Square, PA, 2005) and other published data (Bhaskar et al., 2001; Ji et al., 2001; Kaga et al., 1999; Malek et al., 1996).

Nitrogen adsorption isotherms for both the RuO_2•$1.1H_2O$ and RuO_2 show a minimal amount of hysteresis indicating the absence of extensive meso-porosity for either material (Figure 2-3). Specific Surface area measurements using the Brunauer-Emmet-Teller (BET) method indicated the surface area to be 100 and 50 m^2 g^{-1} for RuO_2•$1.1H_2O$ and RuO_2, respectively. The extent of micro-porosity (pore diameter less than 20 Å) was estimated from a t-plot. There was no indication of micro-porosity for RuO_2, while an estimated 10% of the total surface area of RuO_2•$1.1H_2O$ was comprised of micro-pores.

High Resolution TEM images of RuO_2•$1.1H_2O$ and RuO_2 are presented in Figure 2-4. Images of RuO_2•$1.1H_2O$ showed no indication of crystallinity and fast Fourier transforms (FFT) of the images yielded no detectable spot pattern. The RuO_2•$1.1H_2O$ aggregates did not exhibit any specific shape or size, however, the aggregates rarely exceeded 50 nm. The one noticeable feature from the RuO_2•$1.1H_2O$ HRTEM images is the rough surface noted on the aggregate edges (Figure 2-4A and B). The rough surface and lack of a detectable XRD pattern indicate the amorphous nature of the material while at the same time demonstrating the origin of micro-porosity and large SSA. Similar images of RuO_2•xH_2O demonstrating the absence of any detectable structure have been previously published (Zheng and Xin, 2002). Images of RuO_2 indicate the particles exhibit strong crystallinity as evidenced by the visible crystal lattice, well defined FFT pattern, and lattice fringes (Figure 2-4C and D). Aggregation of RuO_2 particles during the evaporation process made determining particle size difficult. For particles where the crystal edges could be clearly determined the average size was between 10 and 25 nm.

X-ray photoelectric spectroscopy was used to determine the chemical composition of Ru-oxide and to determine the oxidation state of Ru in $RuO_2 \cdot 1.1H_2O$ and RuO_2. There was no indication of contamination of the Ru-oxides as only Ru, O and advantageous C were present Figure 2-5. The oxidation state of ruthenium was determined from narrow scans of the Ru 3d doublet (277-294 eV) (Figure 2-6). Both spectra display the characteristic shape of the Ru 3d doublet exhibiting two relatively narrow peaks corresponding to the 5/2 and 3/2 spin orbit components. The presence of advantageous carbon (284.8 eV) increases the difficulty of isolating the Ru $3d_{3/2}$ spin component necessitating the use of only the 5/2 spin component for determining the Ru oxidation state. Ideally, both Ru oxides are composed solely of Ru(IV), however previous research has reported incomplete oxidation of Ru(III) during $RuCl_3$ oxidation (Kotz et al., 1983; Rard, 1985). Additionally, some researchers have proposed the formation of cus sites which exhibit Ru(VI) like characteristics (McKeown et al., 1999; Panic et al., 2000). The peak maximum for the 5/2 spin component of $RuO_2 \cdot 1.1H_2O$ and RuO_2 occurs at 281.10 and 280.70 eV, respectively. Additionally, the Ru 3d5/2 peak for $RuO_2 \cdot 1.1H_2O$ exhibits peak broadening on the high binding energy (B.E.) side and there is a weak feature present at 282 .8 eV for the RuO_2 (Figure 2-6). Typically the Ru(IV) $3d_{5/2}$ peak in Ru-oxides is characterized by a relatively narrow peak centered at an average binding energy of 280.66 eV which is close to the measured value for RuO_2 (National Institute of Standards and Technology, 2002). The slight shift to a higher B.E. and the peak broadening on the high energy side for $RuO_2 \cdot 1.1H_2O$ are most likely due to the presence of Ru(III) ($3d_{5/2}$ = 281.55 eV) (National Institute of Standards and Technology, 2002). The weak feature present in the RuO_2 spectra at 282.6 eV is attributed to the cus sights present on the oxide surface which result in Ru(IV) oxidation to Ru(VI). The B.E. for Ru (VI) in RuO_3 is 282.5 eV, very close to the value of the feature present in Figure 2-6. As previously mentioned the presence of trace quantities of Ru(III) and Ru(VI) in $RuO_2 \cdot 1.1H_2O$ and RuO_2, respectively is not uncommon due to incomplete oxidation of the $RuCl_3$ precursor, and the loss of coordinated oxygen. Much of the electrochemical and material science research on Ru-oxides has focused on their unique ability to catalyze electrochemical reactions (Trasatti, 1991). Much of this has been attributed to the ability of the oxide surface to form activated sites through metal redox reactions, without adversely affecting crystallinity or solid stability (Trasatti, 1991). The ability of Ru to readily undergo redox reactions without degrading the structure makes it an attractive sorbent material for the oxidation or reduction of organic compounds to less toxic forms, or the oxidation and sequestration inorganic contaminants.

Surface Charging Behavior

The surface charging behavior and point of zero charge (PZC) of $RuO_2 \cdot 1.1H_2O$ and RuO_2 were examined using two separate techniques: zeta potential measurement and proton titration. The PZC determined for both techniques are the isoelectric point (IEP) and the point of zero net proton charge (PZNPC) for the zeta potential measurements and proton titrations, respectively. Both methods were used to assure the PZC measured was due to protonation/deprotonation reactions at the oxide surface and not physical or chemical transformations associated with the specific methods. The PZC determined for $RuO_2 \cdot 1.1H_2O$ and RuO_2 by both methods were in good agreement with each other (Table 2-1 and Figure 2-7). Additionally, the experimentally determined PZC for both oxides is in good agreement with published literature (Kosmulski, 2001 and references there in).

Based on the predominant terminal crystal planes of RuO_2 (Huang and Chen, 2001; Ji et al., 2001; Lister et al., 2002a) and the structure proposed for $RuO_2 \bullet 1.1H_2O$ (McKeown et al., 1999) the surface charge of both oxides is controlled by two types of surface hydroxyl groups. The two types are comprised of a singly and doubly coordinated hydroxyl group. Applying Pauling's bond valence principle (Pauling, 1929) the surface charge can be described by four protonation reactions:

$$\equiv Ru\text{—}O^{-1.33} + H \rightleftharpoons \equiv Ru\text{—}OH^{-0.33} \quad (2\text{-}2)$$

$$\equiv Ru\text{—}OH^{-0.33} \rightleftharpoons \equiv Ru\text{—}OH_2^{0.67} \quad (2\text{-}3)$$

$$\equiv Ru_2\text{—}O^{-0.66} + H^+ \rightleftharpoons \equiv Ru_2\text{—}OH^{0.34} \quad (2\text{-}4)$$

$$\equiv Ru_2\text{—}OH^{0.34} + H^+ \rightleftharpoons \equiv Ru_2\text{—}OH_2^{1.34} \quad (2\text{-}5)$$

As previously mentioned RuO_2 is isostructrual with Rutile (TiO_2). A broad survey of the literature by (Kosmulski, 2001) has demonstrated the similarity between the measured PZC values of isostructural metal oxides. Comparison of the PZC of the Ru-oxides and amorphous and crystalline Ti-oxides indicates both metal oxide exhibit a similar PZC (Kosmulski, 2001). The similarity between the two oxides was used as a basis for determining which of the four protonation reactions contribute to the surface charge between pH 3 and 11. Previous research into the charging behavior of TiO_2 indicates that only Eq. 2-5 and 2-5 are expected to occur in the specified pH range (Hiemstra et al., 1989b; Machesky et al., 2001; Predota et al., 2004; Ridley et al., 2004). Furthermore, research has indicated that surface functional groups exhibiting a charge greater that 1 or -1 generally do not occur in the pH range of 3 to 11 (Hiemstra et al., 1989a; Hiemstra et al., 1989b; Ridley et al., 2004).

Examination of the derivative of the proton titration data indicated the presence of two minimum suggesting a difference between the pKa values of the singly and doubly coordinated functional groups. The pH of the two minimum for both solids are listed in Table 2-1 as pKa_1 and pKa_2. The more acidic functional group is not known, but based on surface complexation modeling of TiO_2 titration data the doubly coordinated group is expected to be more acidic (Hiemstra et al., 1989b; Ridley et al., 2004).

If the surface charge of Ru-oxides is controlled by Eq. 2-3 and 2-5 then the total quantity of H^+ consumed by the surface is equal to hydroxyl surface site density since each protonation reaction involves the uptake of a single proton. The total quantity of protons consumed by $RuO_2 \bullet 1.1H_2O$ was 50 μmol m^{-2} and 20 μmol m^{-2} for RuO_2. The quantity of proton consumed by both oxides indicates a large potential adsorption capacity, compared to other metal oxides. For example, the surface site density of ferrihydrite and hematite is approximately 19 and 16.6 μmol m^{-2} (Schwertmann and Cornell, 2000). The surface site density for hematite and RuO_2 are similar, but $RuO_2 \bullet 1.1H_2O$ greatly exceeds ferrihydrite.

Ruthenium Oxide Dissolution.

Knowledge of the stability and solubility of $RuO_2 \bullet 1.1H_2O$ and RuO_2 is critical in evaluating their potential use as sorbent materials. Metal oxides that readily decompose or exhibit enhanced solubility in pH extremes or in the presence of organic ligands/oxidants have limited use due to the potential for release of the adsorbed contaminant. The dissolution kinetics of $RuO_2 \bullet 1.1H_2O$ and RuO_2 were investigated as a function of proton, hydroxyl, ligand, and reductively promoted dissolution to determine $RuO_2 \bullet 1.1H_2O$ and RuO_2 solubility.

The proton and hydroxyl promoted dissolution of RuO_2•$1.1H_2O$ and RuO_2 was determined in the presence of 0.1 M HCl and NaOH (Figure 2-8). Both oxides exhibited minimal dissolution over the 50 h time period. In the presence of 0.1 M HCl there was no detectable dissolution of RuO_2•$1.1H_2O$ and minimal dissolution of RuO_2. In the presence of the 0.1 M NaOH there was an initial spike in the Ru followed by a decrease in the Ru concentration over time (Figure 2-8). The initial quantity of Ru dissolved for RuO_2•$1.1H_2O$ was 5 times that of the crystalline material (Figure 2-8) demonstrating the amorphous material is immediately more soluble at elevated pH (~13). Unlike the amorphous material there was a rapid decrease in the concentration of dissolved Ru for RuO_2. After two hours the Ru concentration reached an equilibrium concentration equal to that of the 0.1 M HCl dissolution. The similarity in the quantity of Ru surface dissolved in the presence of HCl, and NaOH suggests that a portion of the RuO_2 is readily soluble. We believe this is due to the presence of a meta-stable crystalline phase comprised of ultra fine and/or heavily defect laden crystals. During the synthesis of RuO_2 the resulting crystalline material was not re-hydrated in the presence of acid or base to remove meta stable phases which is often the case in laboratory preparation of other (hydr)oxides for dissolution experiments (Furrer and Stumm, 1986).

The decrease in Ru concentration for RuO_2•$1.1H_2O$ occurred slowly over the entire 50 h time period. Adsorption reactions are generally fast and occur on a time scale of minutes to hours, while adsorption and re-precipitation reactions occur over an extended time period of days to months (Sparks, 2003). Therefore, the rapid decrease in Ru for RuO_2 is believed to be related to Ru adsorption on the oxide surface, while the slow decrease in Ru for RuO_2•$1.1H_2O$ is believed to be related to re-precipitation or re-incorporation of the dissolved phase. Compared to similar research conducted with goethite at identical HCl and NaOH concentrations, Ru-oxides are considerably more stable (Cornell et al., 1976). The insolubility of Ru-oxides at low pH indicates they could be used for sequestration of trace elements in low pH environments (i.e. As released by oxidation of sulfide minerals).

Metal oxide dissolution in the presence of oxalate and ascorbate has been extensively researched (Bennett and Casey, 1993; Cornell and Schwertmann, 2000). The common use of oxalate and ascorbate as a dissolution enhancing ligands/reductants is a result of their common occurrence in nature and their ability to act as analogs for dissolved organic matter. Both ligands exhibit pH dependent adsorption on oxide surfaces (Figure 2-9). The pH adsorption isotherm for oxalate and ascorbate on RuO_2 was similar in nature to adsorption on the hydrous oxide (Figure 2-9). Over all there was a reduction in the quantity of ascorbate adsorbed and an increase in the quantity of oxalate. The reduction in ascorbate adsorption is consistent with a decrease in surface area and reactive surface site density of RuO_2 compared to RuO_2•$1.1H_2O$. The increase in oxalate adsorption for RuO_2 is most likely related to changes in the acidity of surface functional groups. Based on potentiometric titration data the surface charge of Ru-oxides is controlled by protonation and deprotonation of singly and doubly coordinated hydroxyl groups. The pKa values for each functional groups are listed in Table 2-1 for RuO_2•$1.1H_2O$ and RuO_2. The difference between the values of the second pKa for RuO_2•$1.1H_2O$ and RuO_2 indicates the doubly coordinated hydroxyl groups are much more acidic for the amorphous material. Furthermore, the surface of RuO_2 retains protonated surface functional groups and less negative surface charge at elevated pH (Figure 2-4C and D). At pH 7, the pH at which oxalate adsorption on RuO_2 exceeds RuO_2•$1.1H_2O$, the surface charge of RuO_2 is approximately -1 μmol m^{-2} compared to -10 μmol m^{-2} for RuO_2•$1.1H_2O$. A reduction in the surface charge of the RuO_2

creates a more conducive environment by reducing the electrostatic repulsion between the surface and the adsorbing anion.

The mechanism by which oxalate and ascorbate promote dissolution varies (Afonso et al., 1990; Deng, 1997; Furrer and Stumm, 1986; Panias et al., 1996; Suter et al., 1991; Xyla et al., 1992; Zinder et al., 1986). Under non-reductive conditions oxalate is thought to promote dissolution through the formation of a bidentate mononuclear surface complex resulting in the polarization of metal oxygen bonds promoting metal ion detachment in silicates and iron oxides (Afonso et al., 1990; Furrer and Stumm, 1986) (Eq. 2-6).

$$(RuO)RuOH_2^{0.67} + L^{-2} \rightleftharpoons (RuO)Ru\text{-}L^{-1.33} + H_2O + H^+ \rightleftharpoons RuOH^{-0.33} + Ru\text{-}L^{+2} \qquad (2\text{-}6)$$

Ascorbate promoted dissolution occurs through reduction of the oxide metal cation (Ru(IV) to Ru(III)) followed by subsequent release of the reduced metal. Generally the reaction is thought to occur through an adsorbed ascorbate surface complex (Afonso et al., 1990; Deng, 1997; Suter et al., 1991). However, the potential for outer-sphere electron transfer cannot be ruled out as previous research has demonstrated the reduction of Ru(IV) solution complexes ($Ru(NH_3)_5pyridine^{3+}$ and $Ru(NH_3)_4bipyridine^{3+}$) by ascorbate through an outer-sphere electron transfer reaction (Williams and Yandell, 1982). Current results indicate ascorbate forms a surface complex with Ru-oxides (Figure 2-9), therefore a general reductive dissolution mechanism is considered where Ru(IV) reduction occurs through inner-sphere electron transfer mechanism which is the generally accepted mechanism for ascorbate dissolution of Fe oxides (Afonso et al., 1990; Deng, 1997; Suter et al., 1991) (Eq. 2-7).

$$(RuO)_2Ru_2^{(IV)}OH^{0.34} + HA^- \rightleftharpoons (RuO)_2Ru_2^{(VI)}\text{-}A^{-2.33} \rightleftharpoons$$
$$(RuO)_2Ru_2^{(III)}\text{-}A^{-0.34} + 2H^+ \rightleftharpoons 2RuOH^{-0.34} + Ru_2^{(III)}\text{-}A \qquad (2\text{-}7)$$

Since ascorbate oxidation involves a two electron transfer, Equation 2-7 indicates the release of two Ru metal centers during dissolution (Afonso et al., 1990; Suter et al., 1991; Williams and Yandell, 1982).

Figure 2-10, shows the dissolution of $RuO_2 \cdot 1.1H_2O$ in the presence of oxalate and ascorbate at various pH values. Dissolution of the $RuO_2 \cdot 1.1H_2O$ by both organics was initially rapid exhibiting exponential growth before becoming linear after ~10 h. The same phenomenon has been noted for dissolution of other metal oxide and slightly soluble materials and is characteristic of a surface controlled process (Furrer and Stumm, 1986). Dissolution rates for $RuO_2 \cdot 1.1H_2O$ by oxalate and ascorbate were calculated from the linear portion of the experiment (>10 h) which is representative of the steady-state condition (Furrer and Stumm, 1986). The dissolution rate of $RuO_2 \cdot 1.1H_2O$ by oxalate and ascorbate was related to pH and the ligand surface concentration (Figure 2-11). The increased pH dependence of ascorbate promoted dissolution compared to oxalate promoted is related to the reactivity of ascorbate. Deprotonated forms of ascorbate are not as effective at promoting reductive dissolution compared to their protonated counterparts (i.e. the reactivity of $H_2A > HA^- > A_2^-$) (Afonso et al., 1990; Williams and Yandell, 1982). The reaction order of oxalate and ascorbate was determined from linear regression of the ligand surface concentration as a function of rate (Figure 2-11). Interestingly the reaction order calculated for ascorbate and oxalate were identical (reaction order = slope = 0.5) even though the two organics displayed markedly different pH adsorption behavior and exhibit different dissolution rates (Figure 2-9 and 2-11). The fractional reaction order for oxalate and ascorbate is typical for dissolution of metal oxides and silicates (Bennett and Casey, 1994; Lasaga, 1981; Lasaga, 1998; Nagy, 1995).

Solid samples of $RuO_2 \cdot 1.1H_2O$ recovered from the pH 3 dissolution experiments were analyzed by XPS to determine changes in the oxidation state of Ru after exposure to oxalate and ascorbate in order to evaluate the proposed dissolution mechanisms (Figure 2-12). The solid material was washed three times with 0.01 M NaCl (pH 3), and dried at 40^o C prior to XPS analysis. Due to the overlap of the Ru 3d doublet with the C1s peak, changes in the Ru oxidation state were evaluated solely from the Ru $3d_{5/2}$ peak. The Ru $3d_{5/2}$ peak for $RuO_2 \cdot 1.1H_2O$ was located at 280.8 eV which in excellent agreement with the values obtained from the National Institute for Standards and Technology (National Institute of Standards and Technology, 2002) XPS database. The Ru $3d_{5/2}$ peak for $RuO_2 \cdot 1.1H_2O$ after ascorbate promoted dissolution shifted 0.6 eV to 281.4 eV. The shift to a higher B.E. indicates the presence of Ru(III) in the solid material which is consistent with the dissolution mechanism outlined in Equation 2-7. Unexpectedly the Ru $3d_{5/2}$ peak for oxalate promoted dissolution also shifted 0.6 eV to a higher B.E. which is inconsistent with the proposed non-reductive dissolution mechanism (Eq 2-6). The presence of Ru(III) in the solid collected from the oxalate dissolution experiments was not expected since the reduction of Ru(IV) to Ru(III) was not thought to be thermodynamically favorable (Sparks, 2003; Zen et al., 2001). Two potential explanations for the reduction of Ru(IV) include: 1) changes in the standard reduction potential of Ru based on the thermodynamic stability of the surrounding ligands (Atkins et al., 2006), or 2) indirect electron transfer from un-reacted $RuCl_3$, similar to the dissolution mechanism proposed for goethite dissolution in the presence of oxalate and Fe^{2+} (Cornell and Schindler, 1987; Zinder et al., 1986).

As a general trend the formation of more thermodynamically stable transmission metal complexes results in an increase in the standard reduction potential (E^o) of the metal (more negative value) with the end result being a metal complex more resistant to reduction by inner-or outer-sphere electron transfer (Atkins et al., 2006; Williams and Yandell, 1982). Table 2-2 lists the E^o for three Ru redox couples, oxalate, and ascorbate (the E^o for $RuO_2 \cdot 1.1H_2O$ was calculated from thermodynamic data since experimental values were not available). The increase in E^o (less positive values) for Ru in more structured environments is readily demonstrated by the values presented for the redox couples. Based on the data listed in Table 2-2, reduction of Ru(IV) in $RuO_2 \cdot 1.1H_2O$ is thermodynamically favorable at standard state conditions. A similar trend in of increasing reduction potentials with increasing thermodynamic stability is also present for Fe and Mn oxides, two of the most common metal electron receptors in nature.

Dissolution of goethite by oxalate in the absence of light and Fe^{2+} occurs through a ligand promoted dissolution mechanism similar to the one outlined in Equation 2-6. However, in the presence of Fe^{2+}, oxalate promoted dissolution occurs through an indirect electron transfer (Cornell and Schindler, 1987; Suter et al., 1991; Zinder et al., 1986). A similar type of mechanism may occur with oxalate promoted dissolution of $RuO_2 \cdot 1.1H_2O$. As previously mentioned hydrous Ru-oxides synthesized by the oxidation of $RuCl_3$ often contain trace quantities of the un-oxidized salt (Kotz et al., 1983; Rard, 1985). The presence of Ru^{3+} from the un-reacted chloride salt could promote reductive dissolution of $RuO_2 \cdot 1.1H_2O$ through an indirect electron transfer, similar to what is seen for oxalate promoted dissolution of goethite in the presence of Fe^{2+}.

Results from the XPS analysis of $RuO_2 \cdot 1.1H_2O$ dissolution by oxalate reveal that a purely ligand promoted dissolution mechanism is incorrect. Instead oxalate promoted dissolution of $RuO_2 \cdot 1.1H_2O$ more closely resembles Mn (hydr)oxide reduction (scenario 1) or reductive dissolution of Fe (hydr)oxide through indirect electron transfer from Fe^{2+} (Scenario 2).

Potential reaction sequences for both mechanisms are presented in Equations 2-8 and 2-9 (The dissolution mechanism in Equation 2-8 and 2-9 are modeled after the mechanisms proposed by Xyla et al. (1992) and Suter et al. (1991), respectively).

$$(RuO)_2Ru_2^{(IV)}OH^{0.34} + L^{-2} \rightleftharpoons (RuO)_2Ru_2^{(VI)}\text{-}L^{-2.33} \rightleftharpoons$$
$$(RuO)_2Ru_2^{(III)}\text{-}L^{-0.34} + 2H^{+} \rightleftharpoons 2RuOH^{-0.34} + Ru_2^{(III)}\text{-}L \quad (2\text{-}8)$$

$$(RuO)Ru^{(IV)}OH_2^{0.67} + L^{-2} \rightleftharpoons (RuO)Ru^{(IV)}\text{-}L^{-1.33} + OH^{-} + Ru^{3+} \rightleftharpoons$$
$$(RuO)Ru^{(IV)}\text{-}L\text{-}Ru^{(III)2.66} \rightleftharpoons (RuO)Ru^{(III)}\text{-}L\text{-}Ru^{(IV)2.66} \rightleftharpoons \quad (2\text{-}9)$$
$$(RuO)Ru^{(III)} + Ru^{(IV)}\text{-}L^{+2} + H_2O \rightleftharpoons RuOH_2^{0.67} + Ru^{(III)}$$

The actual mechanism involved in the oxalate promoted dissolution of $RuO_2 \cdot 1.1H_2O$ is more than likely a combination of the two mechanisms since reductive dissolution of $RuO_2 \cdot 1.1H_2O$ (Eq. 2-8) would provide a source of Ru^{3+} for reductive dissolution by indirect electron transfer (Eq. 2-9) thereby initiating an autocatalytic dissolution cycle.

Dissolution of RuO_2 by oxalate and ascorbate was only detectable for oxalate at pH 3 (Figure 2-13). There was a detectable quantity of Ru present for ascorbate promoted dissolution at pH 3, but the concentration was invariant throughout the experiment. The lack of appreciable dissolution of RuO_2 by oxalate at pH values above 3 is not surprising, even at surface concentrations of oxalate near adsorption capacity (20 μmol m^{-2}) (Figure 2-9). Ruthenium oxide (RuO_2) is extremely insoluble making it an ideal electrocatalyst for $Cl_{2(g)}$ production due its ability to withstand harsh chemical environments associated with chlorine synthesis (Panic et al., 2000; Raistrick and Sherman, 1987; Rard, 1985; Trasatti, 1991). As previously mentioned rutile (TiO_2) is isostructural with RuO_2 and is often used as a support for RuO_2 films in electrochemical reactors (Panic et al., 2000; Panic et al., 2003; Raistrick and Sherman, 1987). The adsorption of oxalate by RuO_2 has not been previously investigated, but several recent studies have evaluated oxalate adsorption on rutile (TiO_2) (Dobson and McQuillan, 1999; Hug and Sulzberger, 1994; Hug and Bahnemann, 2006). The similarity in crystal structure and resistance to degradation of TiO_2 and RuO_2 would indicate that oxalate adsorption on rutile should be similar to adsorption on RuO_2. Spectroscopic research indicates oxalate forms stable mono- and bidentate inner-sphere complexes with rutile that do not promote or enhance dissolution (Hug and Bahnemann, 2006). Adsorption and kinetic data (pH > 3) suggest the same conclusion for RuO_2, indicating oxalate is not nucleophilic enough to promote ligand dissolution above pH 3.

The lack of any detectable dissolution of RuO_2 by ascorbate (Figure 2-13) conflicts with thermodynamic calculations using standard potentials experimentally determined for Ru(IV) reduction in RuO_2 and ascorbate oxidation (Table 2-2). Instead the current results indicate that RuO_2 is stable in the presence of reductants known to dissolve Fe-oxides a primary material used in sequestering oxyanions and metals for water treatment. The calculated value of E^o for the reduction of $Ru(IV)O_2$ by ascorbate is 0.09V. The low magnitude of the value suggests only a small decrease in the Gibbs Free energy of the reaction (-1.9 kJ mol^{-1}). Surface structural anomalies, competitive interaction of ascorbate with Cl^- (background electrolyte) for adsorption sites, or steric interaction of ascorbate with the RuO_2 surface could reduce the gain in Free energy making the reaction thermodynamically unfavorable.

Kinetic rates calculated from dissolution experiments are empirical in nature and direct comparison of rates between different studies is not possible. However, qualitatively the values allow for limited comparisons between studies and solid phases. Dissolution rates calculated for

RuO_2•1.1H_2O and RuO_2 in the presence of both ligands at pH 3 were compared with dissolution rates for various Fe (hydr)oxides and silica (Table 2-3). The oxalate promoted dissolution rate for RuO_2•1.1H_2O and RuO_2 at pH 3 was an order of magnitude slower than the dissolution rates presented for several oxides. The same was true for ascorbate in comparison to goethite and hematite. Overall the reported dissolution rates for Ru-oxide dissolution by oxalate and ascorbate are on average an order of magnitude slower than those reported for Fe (hyr)oxides, indicating a high degree of mineral stability.

SUMMARY

The physical, chemical, and solubility properties of two Ruthenium oxides have been extensively characterized to evaluate their potential use as sorbent materials for water treatment. The hydrous ruthenium oxide (RuO_2•1.1H_2O) was determined to be amorphous in nature with a large SSA (100 m^2 g^{-1}). Annealing of the hydrous oxide material at 500^o C produced a crystalline ruthenium oxide (RuO_2) with a rutile crystal structure and half the surface area of the amorphous material (50 m^2 g^{-1}). HRTEM images indicated the RuO_2 particles were between 10 and 25 nm in size. XPS measurements indicated both oxides contained mixed oxidation states of Ru. Both RuO_2•1.1H_2O and RuO_2 were predominately composed of Ru(IV) with smaller quantities of Ru(III) and Ru(VI) present for RuO_2•1.1H_2O and RuO_2, respectively. Surface charging experiments revealed an increase in ZPC and a decrease in the quantity of titratable functional groups with crystallization of the amorphous material. Proton titrations revealed surface site densities of 50 and 20 μmol m^{-2} for RuO_2•1.1H_2O and RuO_2, respectively.

Proton promoted dissolution of the Ru-oxides indicated no detectable dissolution in the presence of 0.1 M HCl. Conversely there was an initial release of Ru in hydroxyl promoted dissolution experiments which subsequently re-adsorbed or re-precipitated over the 50 hour study period. Ascorbate promoted dissolution of RuO_2•1.1H_2O exceed the rate of oxalate dissolution at equimolar concentrations (5 mM) over the pH range investigated. Analysis of the oxidation state of Ru in RuO_2•1.1H_2O after ascorbate and oxalate promoted dissolution indicated the presence of Ru(III) in both materials, indicating reductive dissolution of RuO_2•1.1H_2O by both oxalate and ascorbate. Two dissolution mechanism for oxalate reduction of RuO_2•1.1H_2O were proposed based on previous research examining Mn (hydr)oxide dissolution and indirect reduction of Fe(III) (hydr)oxides by oxalate and Fe^{2+}. Both dissolution mechanisms are believed to be involved during oxalate dissolution. Dissolution of RuO_2 was only detectable for oxalate at pH 3. At all other pH values investigated and in the presence of ascorbate there was not detectable dissolution of RuO_2.

The chemical and physical properties characterized in the current research indicate ruthenium oxides may be used successfully as sorbent materials in water treatment. The large surface area, presence of multiple Ru oxidation states in both materials, and the large quantity of surface functional groups represent ideal qualities of metal oxide sorbents used in water treatment. The insoluble nature, adsorption reactivity in the environmental pH range (3-11) and large adsorption capacity (arsenate adsorption (Impellitteri et al., 2003)) demonstrate that ruthenium oxides may be superior to other metal oxide sorbents in specific environments that would otherwise promote dissolution of iron oxides.

TABLES

Table 2-1 Point of Zero charge and proton acidity constant for amorphous and crystalline ruthenium oxide

Solid	IEP	PZNPC	pKa_1	pKa_2
$RuO_2 \cdot 1.1H_2O$	4.22±0.15	4.20±0.10	-3.08±0.29	-4.82±0.10
RuO_2	5.15±0.12	5.27±0.12	-4.77±0.32	-8.62±0.17

Table 2-2 Standard Reduction Potentials for select Ru species, oxalate, and ascorbate

Redox Couple	E^0 (V)	Source
$Ru^{IV}O_2 + 4H^+ + e^- \rightleftharpoons Ru^{3+} + 2H_2O$	0.41	(Zen et al., 2001)
$Ru^{IV}O_2 \bullet 2H_2O + 4H^+ + e^- \rightleftharpoons Ru^{3+} + 4H_2O$	0.84*	(Rard, 1985; Xue and Osseoasare, 1989)
$RuOH_2^{2+} + e^- \rightleftharpoons Ru^{3+} + 2OH^-$	0.86	(Williams and Yandell, 1982; Xyla et al., 1992)
$2CO_2 + 2e^- \rightleftharpoons C_2O_4^{2-}$	-0.63	(Sparks, 2003; Xyla et al., 1992)
$\text{Dehydroascorbate} + H^+ + 2e^- \rightleftharpoons \text{Ascorbate}$	-0.40	(Sparks, 2003; Williams and Yandell, 1982)

*Calculated from thermodynamic data E^0

Table 2-3 Dissolution rate of $RuO_2 \cdot 1.10H_2O$ and other Fe oxides in the presence of oxalate and ascorbate.

Solid	pH	Ligand	Concentration (mM)	Rate Constant $\mu mol\ m^{-2}\ h^{-1}$	Source
$RuO_2 \cdot 1.1H_2O$	3	Oxalate	5.0	$4.21*10^{-4} \pm 5.1*10^{-5}$	This Study
RuO_2	3		5.0	$4.43*10^{-4} \pm 5*10^{-5}$	This Study
Hematite	3		1.0	0.018	(Zinder et al., 1986)
Hematite	3		0.05	0.021	(Banwart et al., 1989)
Goethite	3		5.0	0.0023	(Eick et al., 1999)
Goethite	2.6		5.0	0.0024	(Cornell and Schindler, 1987)
Silica	7		20	0.009	(Bennett and Casey, 1993)
$RuO_2 \cdot 1.1H_2O$	3	Ascorbate	5.0	$0.0015 \pm 2*10^{-4}$	This Study
Fe(III)hydroxide	4		48	0.0025	(Deng, 1997)
Hematite	3		0.1	0.148	(Suter et al., 1991)
Hematite	3		0.1	0.148	(Banwart et al., 1989)
Goethite	3		1.0	0.0654	(Zinder et al., 1986)

FIGURES

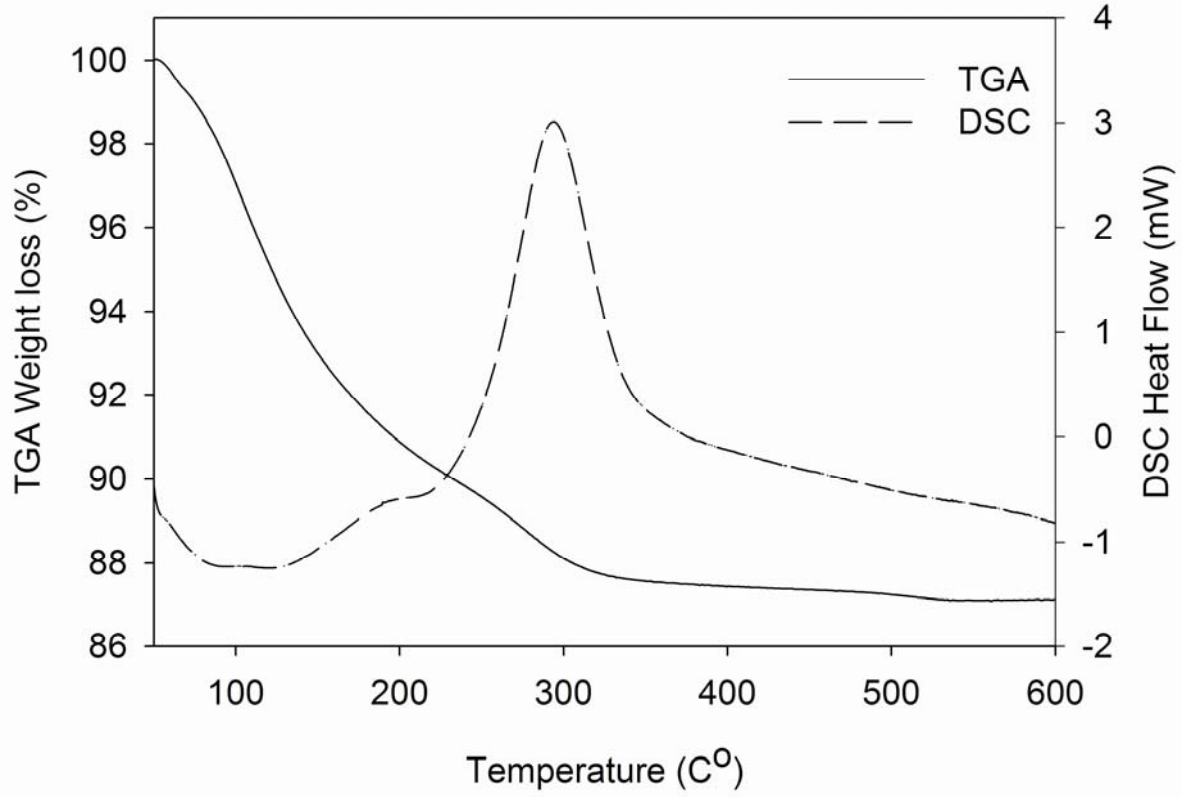

Figure 2-1 TGA and DSC plots for the amorphous ruthenium oxide material

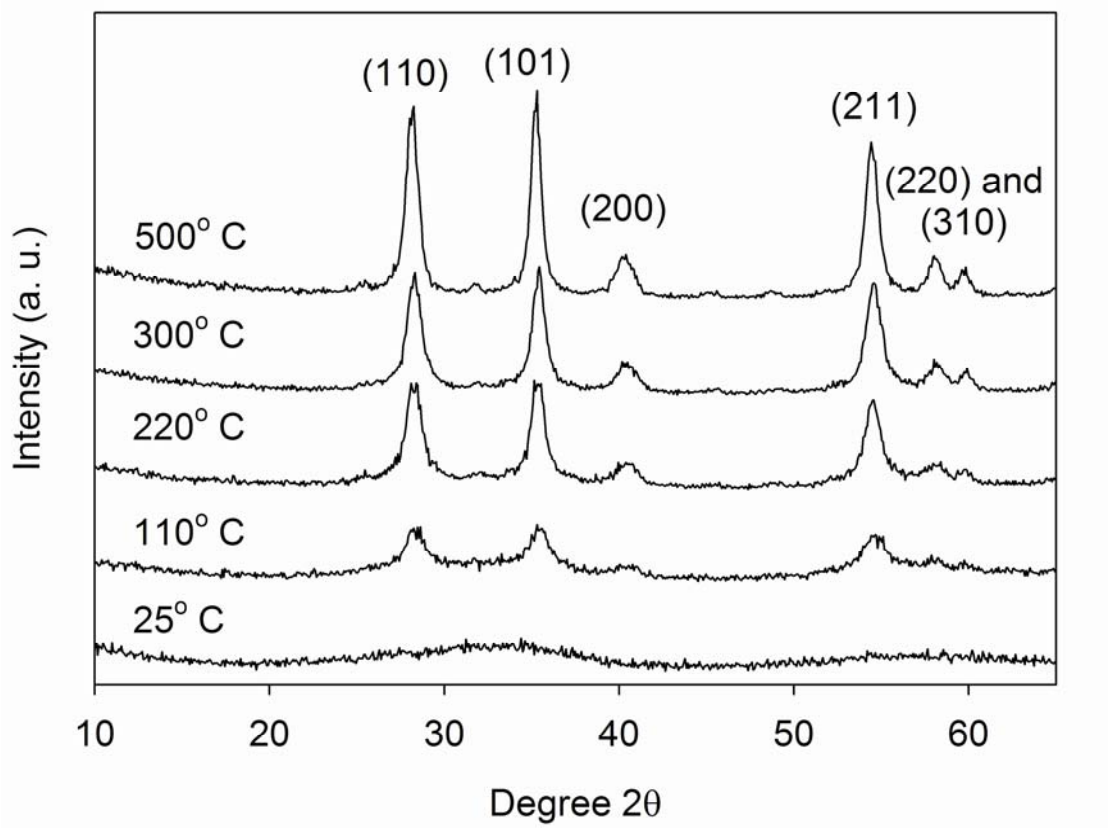

Figure 2-2 X-Ray diffraction spectra for Ru-oxides annealed at various temperatures. Values in parentheses refer to the Miller Indices.

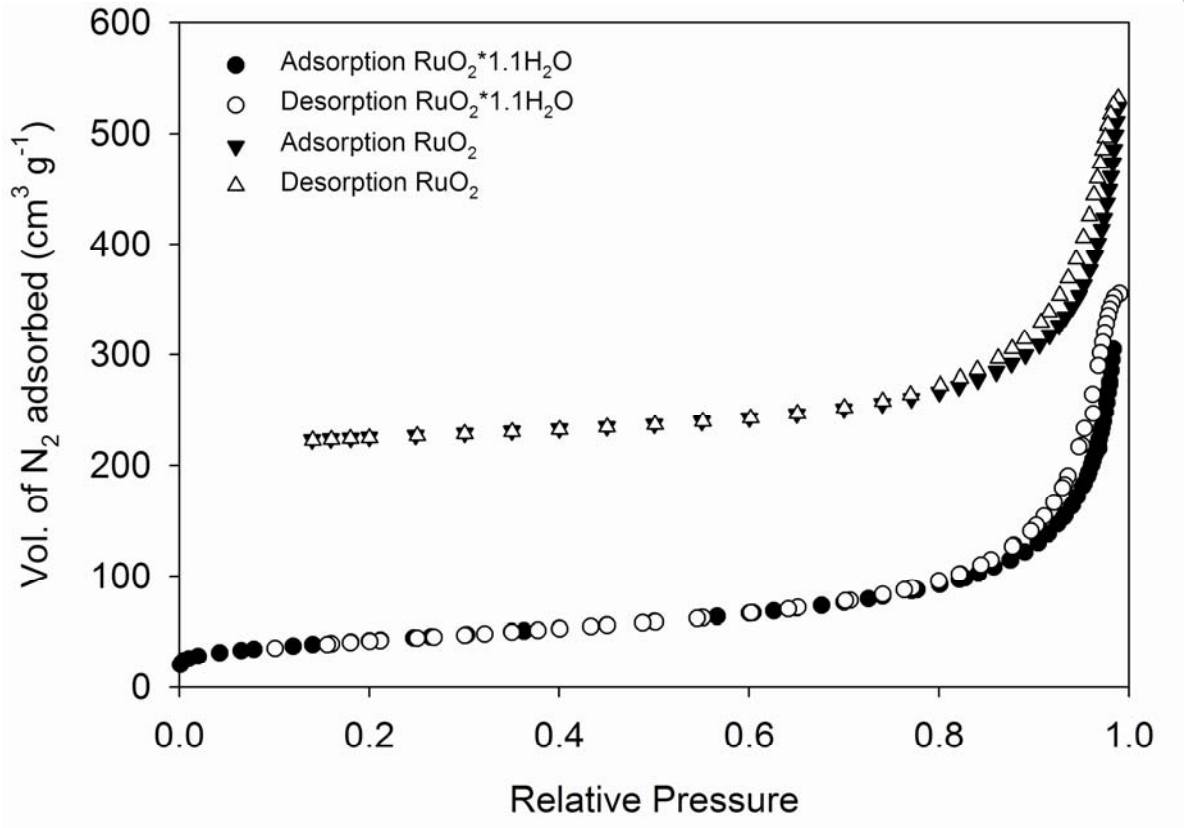

Figure 2-3 Nitrogen adsorption and desorption isotherms for the amorphous and crystalline ruthenium oxides. The crystalline ruthenium adsorption/desorption isotherms are off-set by 200 cm^3 g^{-1}.

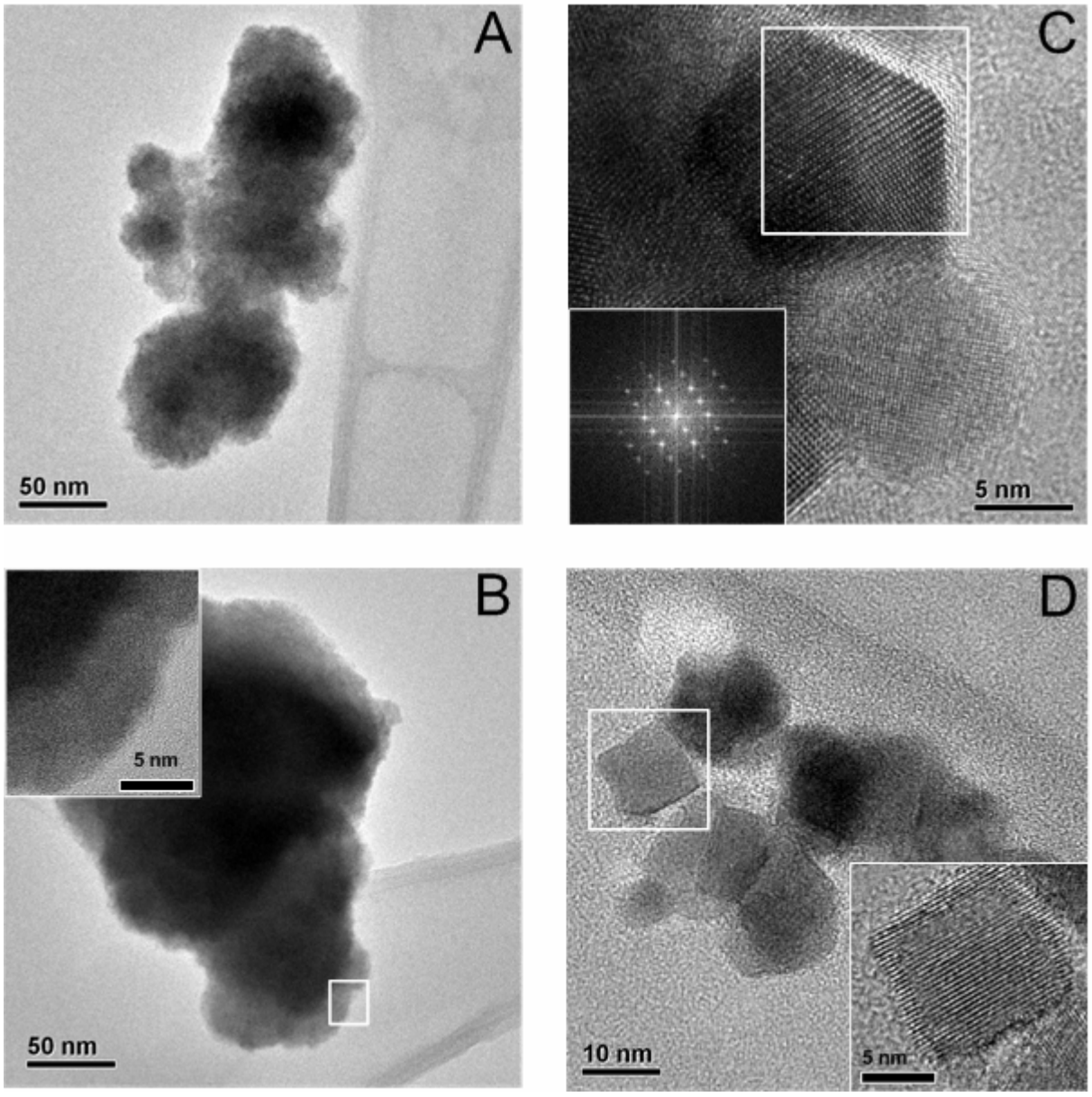

Figure 2-4 High Resolution TEM Images of RuO_2•1.1H_2O and RuO_2. (A) evaporated RuO_2•1.1H_2O. (B) evaporated RuO_2•1.1H_2O, inset contains magnification of the area enclosed by the white box. (C) Evaporated RuO_2 showing lattice fringes, inset contains the Fourier transform of the area enclosed by the white box. (D) Evaporated RuO_2 aggregate, inset contains magnification of the area enclosed in the white box.

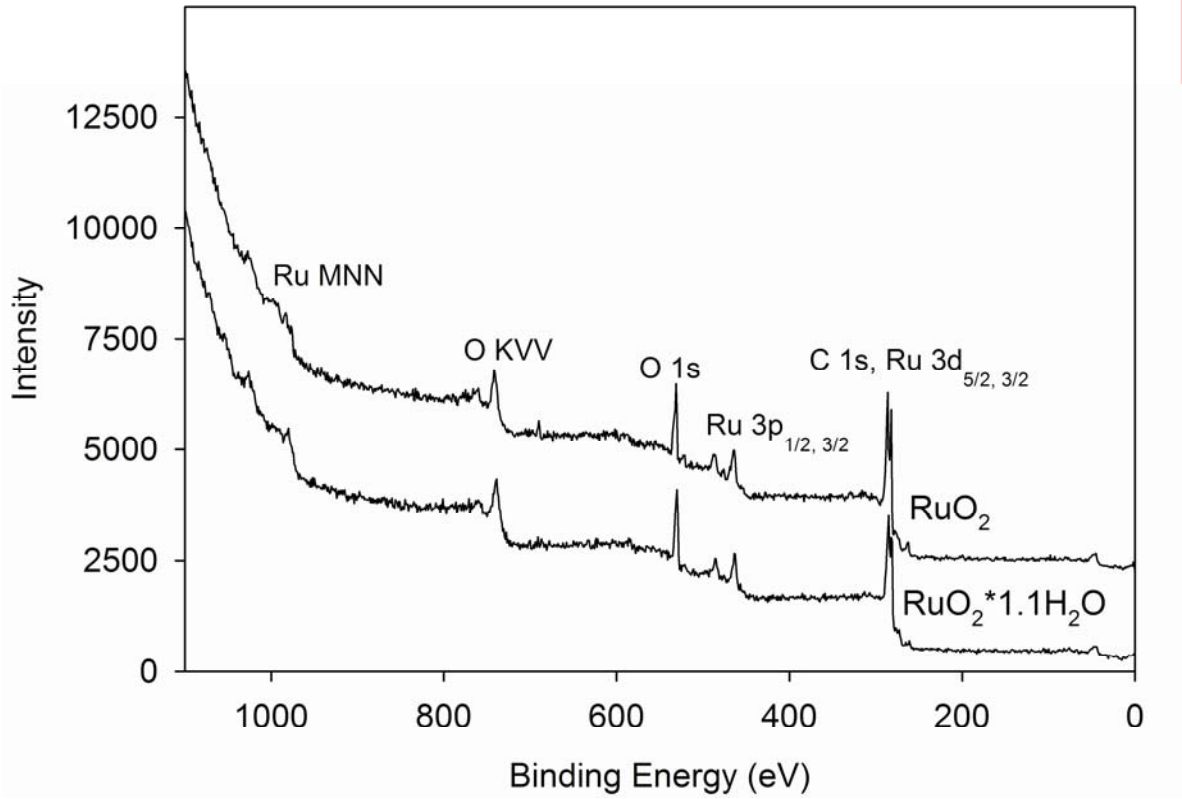

Figure 2-5 XPS broad scan of RuO_2 and RuO_2•1.1H_2O. The two spectra are offset for comparison purposes.

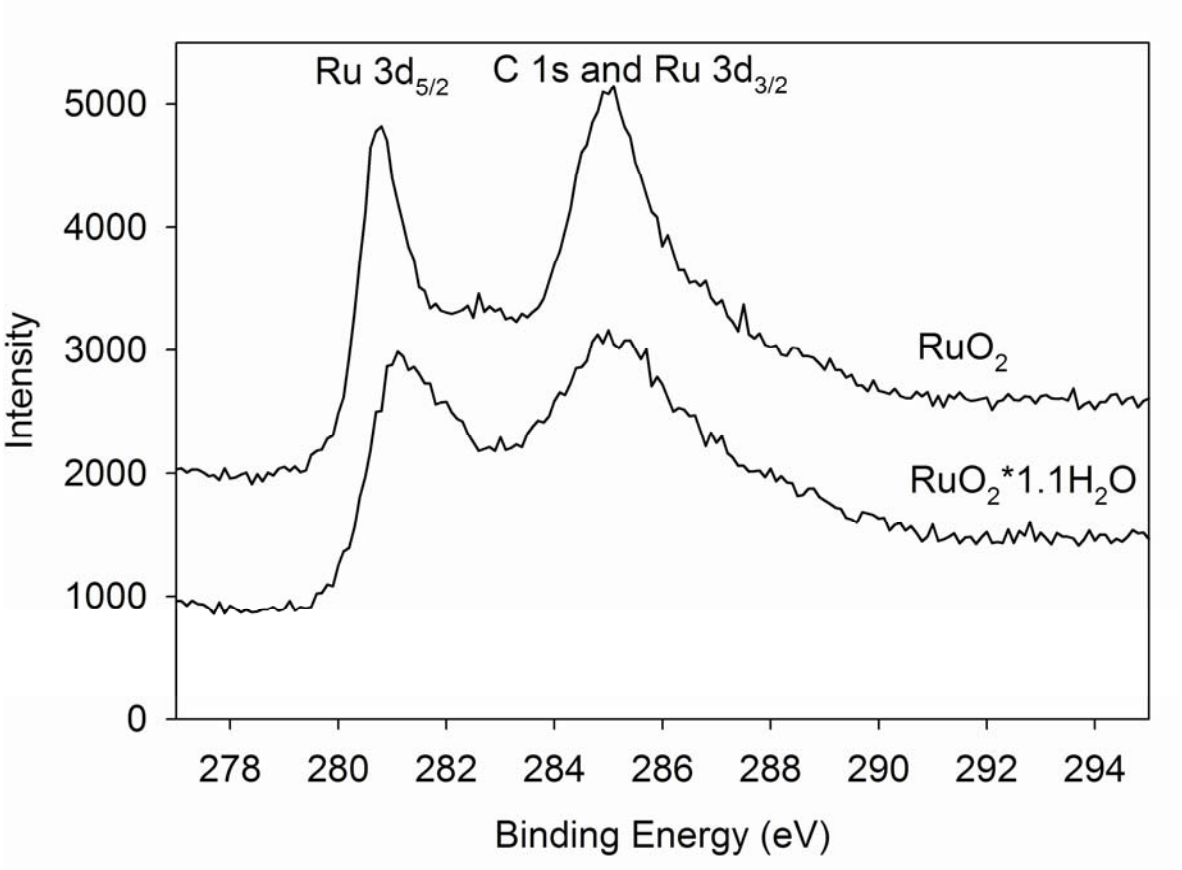

Figure 2-6 XPS narrow scans of Ru 3d doublet for RuO_2 and RuO_2•1.1H_2O. The two spectra are offset for comparison purposes and have not been background corrected.

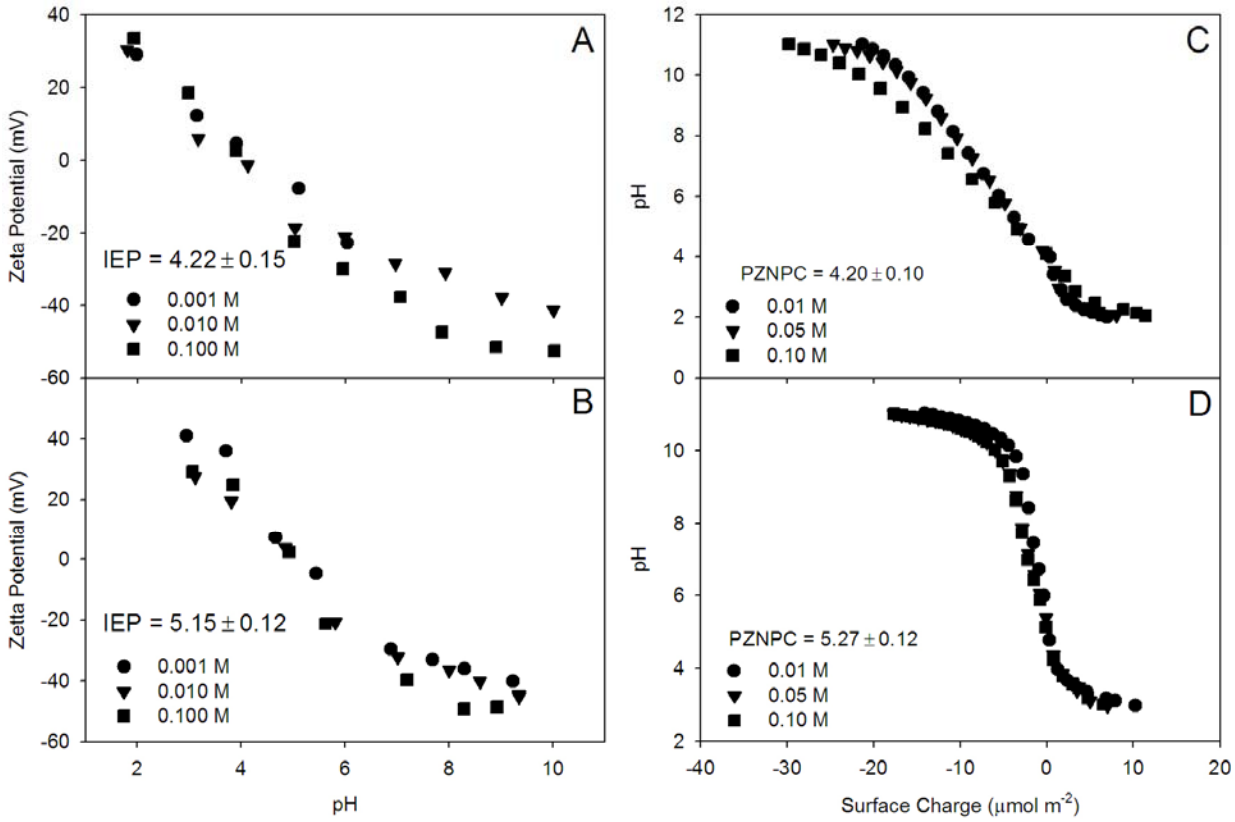

Figure 2-7 Surface charging of ruthenium oxides as a function of pH as determined by zeta potential measurement and proton titrations. (A) Zeta potential measurements for amorphous ruthenium oxide. (B) Zeta potential measurements for crystalline ruthenium oxide. (C) Surface charge of amorphous ruthenium oxide determined from proton titration data. (D) Surface charge of crystalline ruthenium oxide determined from proton titration data.

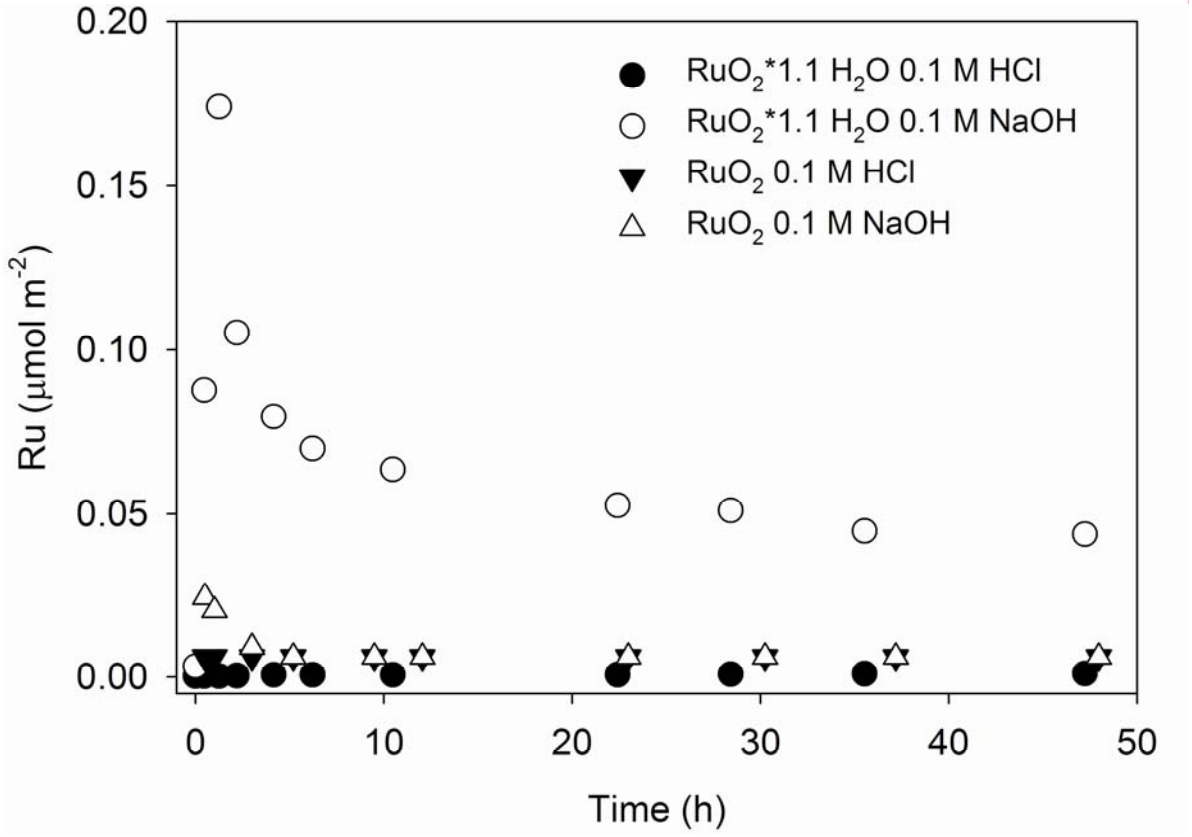

Figure 2-8 Proton promoted dissolution of RuO_2•1.1H_2O and RuO_2.

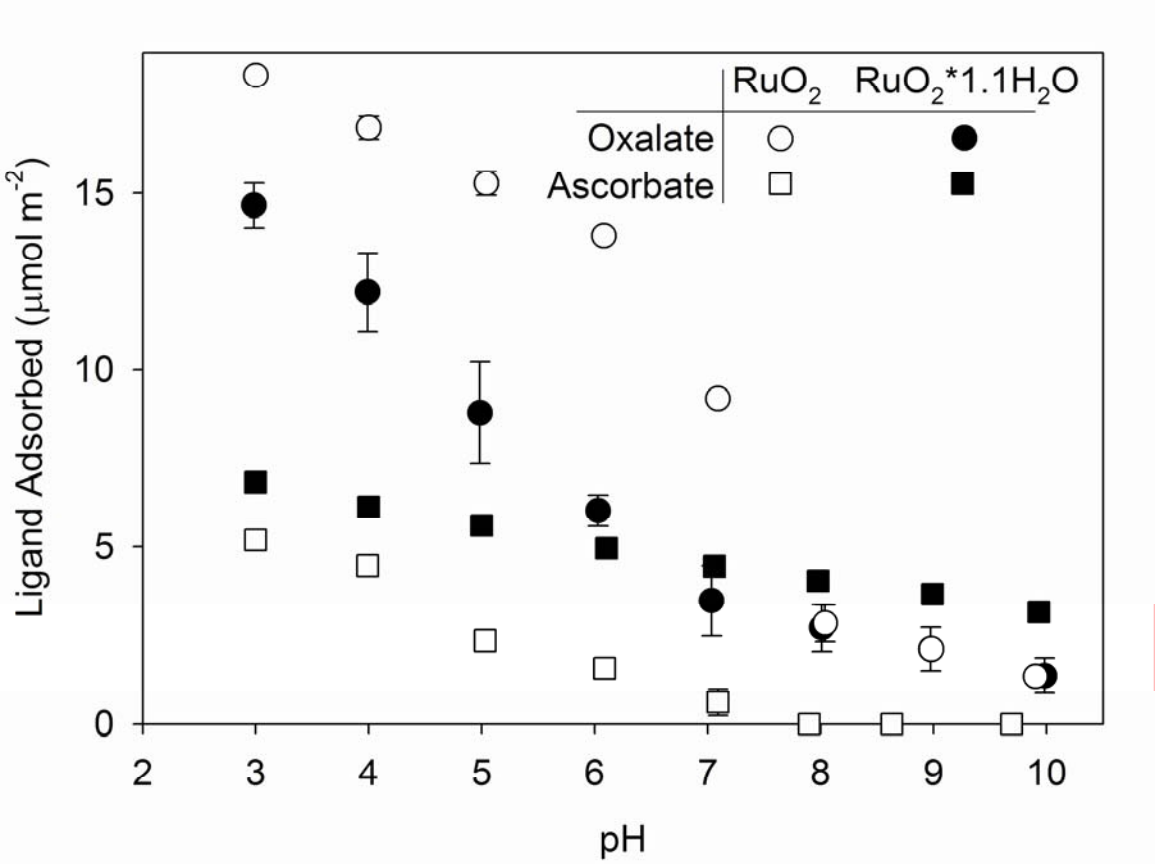

Figure 2-9 pH adsorption edge of oxalate and ascorbate on RuO_2•$1.1H_2O$ and RuO_2.

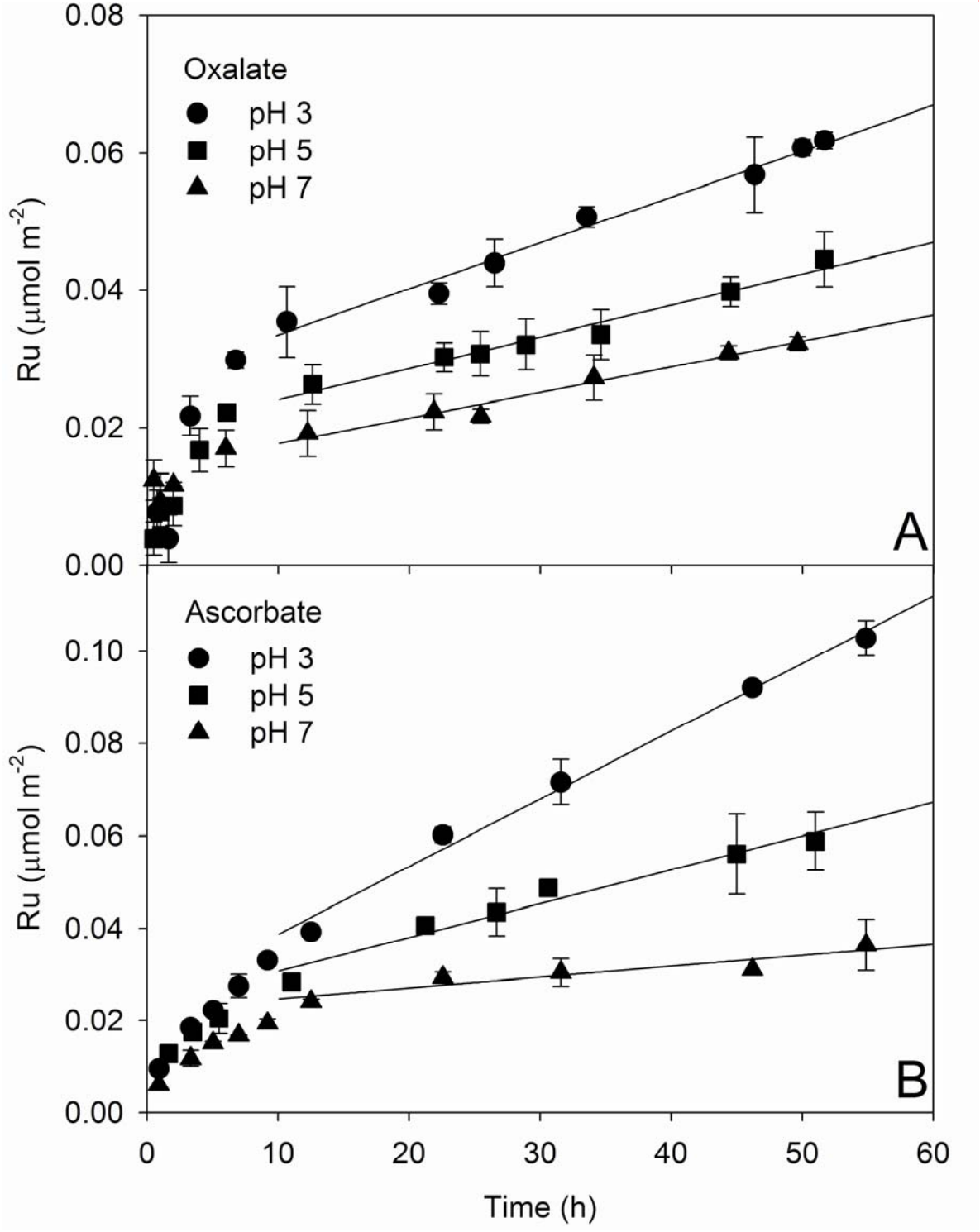

Figure 2-10 Dissolution of RuO_2•1.10H_2O by oxalate and ascorbate at pH 3, 5, and 7. (A) Oxalate promoted dissolution. (B) Ascorbate promoted dissolution. Lines indicate the portion of the dissolution data from which rates constants were calculated.

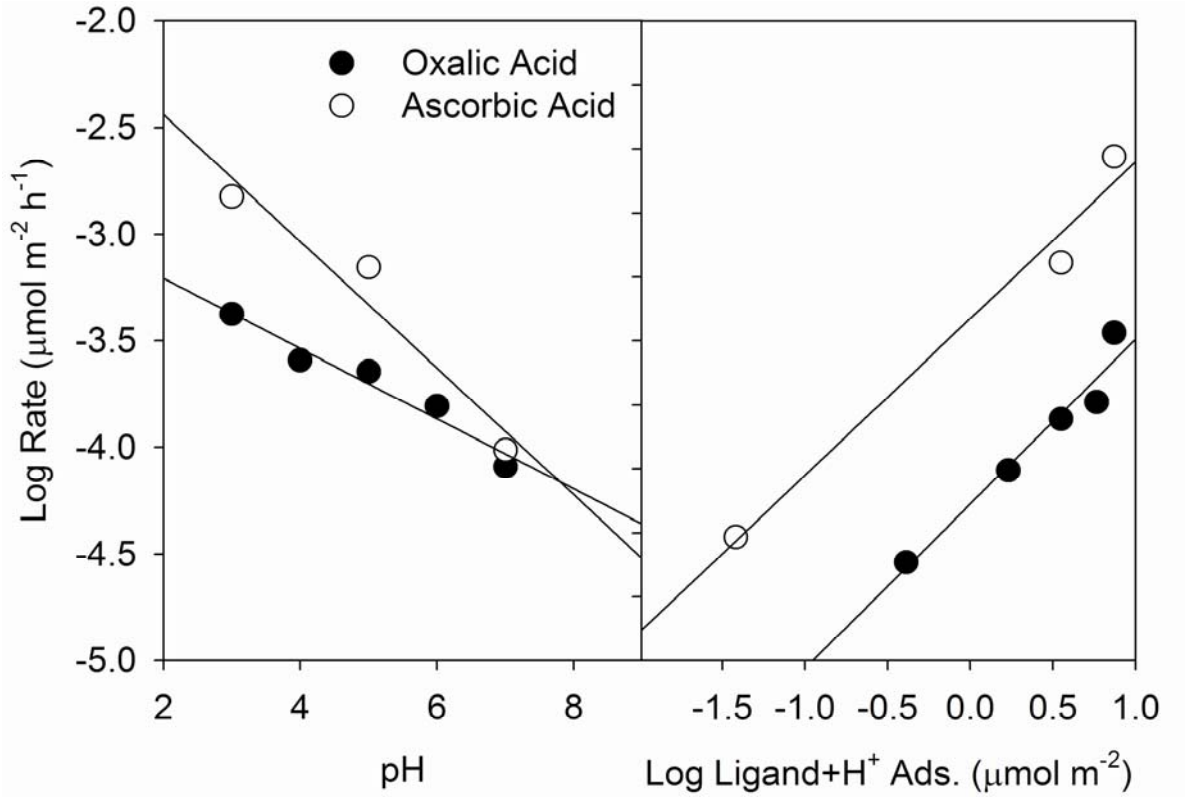

Figure 2-11 RuO_2•1.1H_2O dissolution rate as a function of pH and surface concentration of the adsorbed ligand.

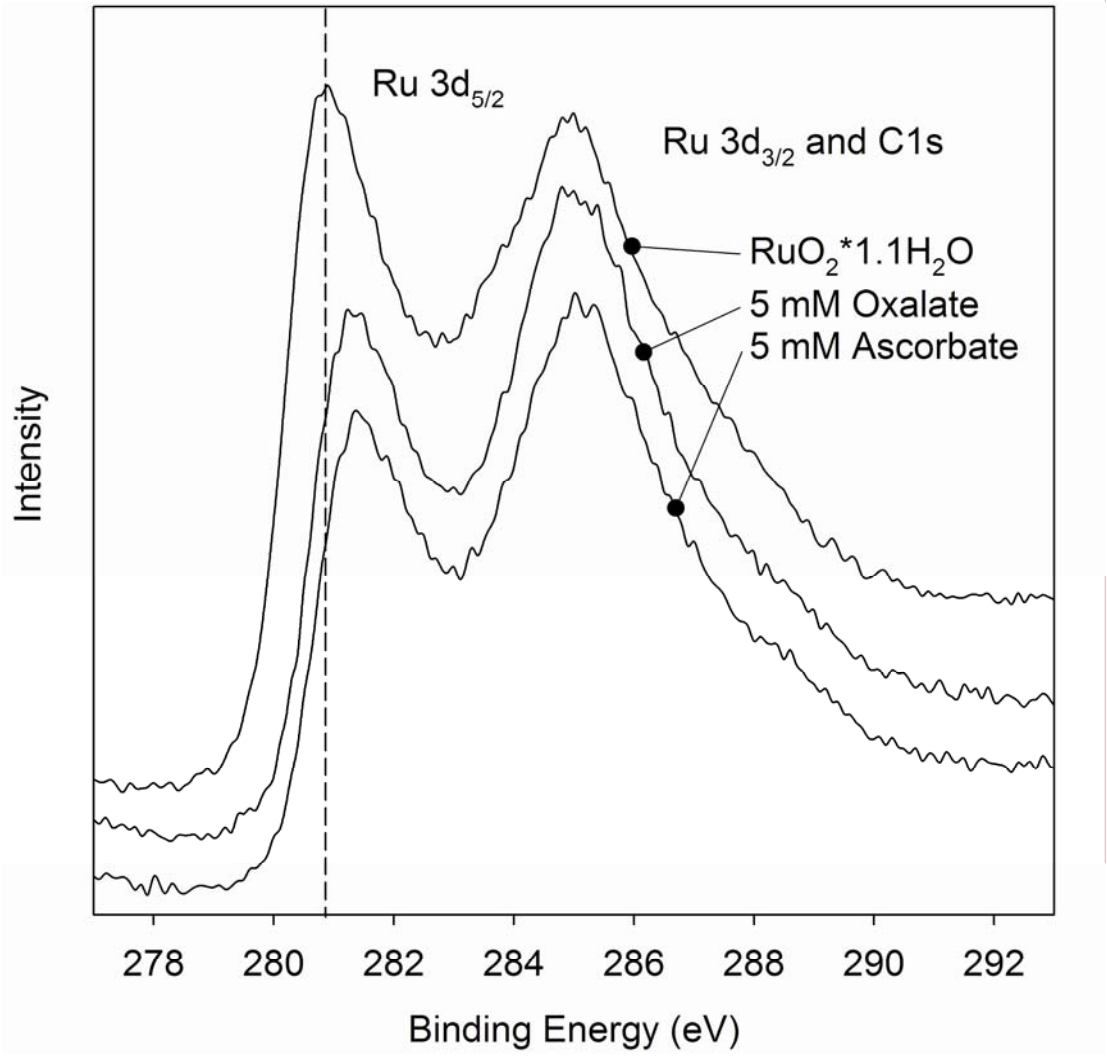

Figure 2-12 XPS narrow scans for Ru 3d doublet of RuO_2•1.1H_2O before and after dissolution in the presence of 5 mM oxalate and ascorbate. XPS spectra are offset for comparative purposes.

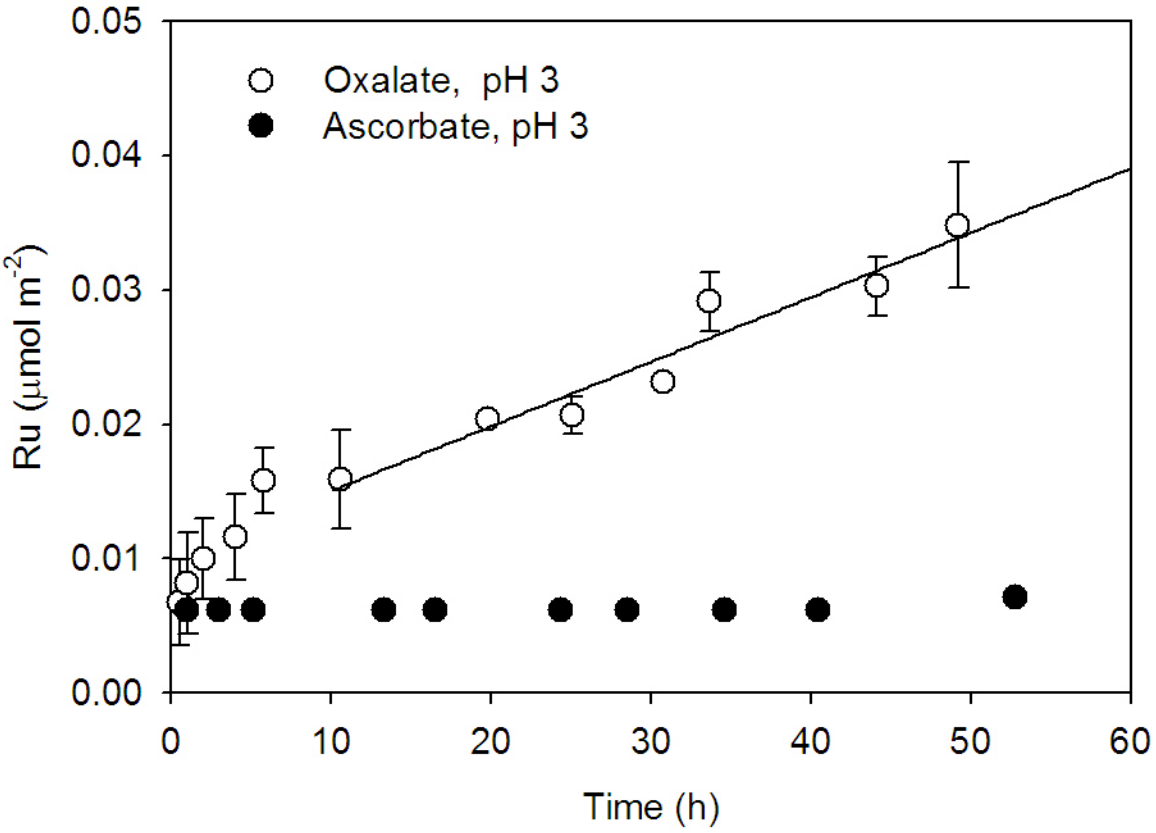

Figure 2-13 RuO_2 dissolution in the presence of 5 mM oxalate and ascorbate at pH 3.

REFERENCES

Afonso, M.D., P.J. Morando, M.A. Blesa, S. Banwart, and W. Stumm. 1990. The Reductive Dissolution of Iron-Oxides by Ascorbate - the Role of Carboxylate Anions in Accelerating Reductive Dissolution. Journal of Colloid and Interface Science 138:74-82.

Atkins, P., T. Overton, J. Rourke, M. Weller, F. Armstrong, P. Salvador, M. Hagerman, T. Spiro, and E. Stiefel. 2006. Shiver & Atkins Inorganic Chemistry. 4th ed. W. H. Freeman and Co., New York, NY.

Banwart, S., S. Davies, and W. Stumm. 1989. The Role of Oxalate in Accelerating the Reductive Dissolution of Hematite (Alpha-Fe_2O_3) by Ascorbate. Colloids and Surfaces 39:303-309.

Basame, S.B., D. Habel-Rodriguez, and D.J. Keller. 2001. Morphology and surface reconstruction on RuO2 single crystals. Applied Surface Science 183:62-67.

Bennett, P.C., and W. Casey. 1993. Chemistry and mechanisms of low-temperature dissolution of silicates by organic acids p. 162-200, *In* E. D. Pittman and M. D. Lewan, eds. Organic Acids in Geological Processes. Springer-Verlag, Berlin.

Bennett, P.C., and W. Casey. 1994. Chemistry and mechanisms of low temperature dissolution of silicates by organic acids, p. 162-200, *In* E. D. Pittman and M. D. Lewan, eds. organic Acids in Geological Processes. Springer-Verlag, New York. New York.

Bhaskar, S., P.S. Dobal, S.B. Majumder, and R.S. Katiyar. 2001. X-ray photoelectron spectroscopy and micro-Raman analysis of conductive RuO2 thin films. Journal of Applied Physics 89:2987-2992.

Chen, L.L., D. Guay, F.H. Pollak, and F. Levy. 1997. AFM observation of surface activation of ruthenium oxide electrodes during hydrogen evolution. Journal of Electroanalytical Chemistry 429:185-192.

Cornell, R.M., and P.W. Schindler. 1987. Photochemical dissolution of goethite in acid/oxalate solution. Clays and Clay Minerals 35:347-352.

Cornell, R.M., A.M. Posner, and J.P. Quirk. 1976. Kinetics and Mechanisms of Acid Dissolution of Goethite Alpha-FeOOh). Journal of Inorganic & Nuclear Chemistry 38:563-567.

Deng, Y.W. 1997. Effect of pH on the reductive dissolution rates of iron(III) hydroxide by ascorbate. Langmuir 13:1835-1839.

Dobson, K.D., and A.J. McQuillan. 1999. In situ infrared spectroscopic analysis of the adsorption of aliphatic carboxylic acids to TiO2, ZrO2, Al2O3, and Ta2O5 from aqueous solutions. Spectrochimica Acta Part a-Molecular and Biomolecular Spectroscopy 55:1395-1405.

Eick, M.J., J.D. Peak, and W.D. Brady. 1999. The effect of oxyanions on the oxalate-promoted dissolution of goethite. Soil Science Society of America Journal 63:1133-1141.

Froment, P., M.J. Genet, and M. Devillers. 1999. Surface reduction of ruthenium compounds with long exposure to an X-ray beam in photoelectron spectroscopy. Journal of Electron Spectroscopy and Related Phenomena 104:119-126.

Fu, R.Q., Z.R. Ma, and J.P. Zheng. 2002. Proton NMR and dynamic studies of hydrous ruthenium oxide. Journal of Physical Chemistry B 106:3592-3596.

Furrer, G., and W. Stumm. 1986. The Coordination Chemistry of Weathering .1. Dissolution Kinetics of Delta-Al_2O_3 and Beohmite. Geochimica Et Cosmochimica Acta 50:1847-1860.

Galizzioli, D., F. Tantardini, and S. Trasatti. 1974. Ruthenium dioxide: a new electrode material. I. Behavior in acid solutions of inert electrolytes Journal of Applied Electrochemistry 4:57-67.

Hiemstra, T., W.H. van Riemsdijk, and G.H. Bolt. 1989a. Multisite proton adsorption modeling at the solid/solution interface of (hydr)oxides: A new approach
I. Model description and evaluation of intrinsic reaction constants. Journal of Colloid and Interface Science 133:91-104.

Hiemstra, T., J.M.C. De Wit, and W.H. van Riemsdijk. 1989b. Multisite proton adsorption modeling at the solid/solution interface of (hydr)oxides: a new approach
II. Application to various important (hydr)oxides. Journal of Colloid and Interface Science 133:105-115.

Hrbek, J., D.G. Vancampen, and I.J. Malik. 1995. The Early Stages of Ruthenium Oxidation. Journal of Vacuum Science & Technology a-Vacuum Surfaces and Films 13:1409-1412.

Hu, C.C., and Y.H. Huang. 2001. Effects of preparation variables on the deposition rate and physicochemical properties of hydrous ruthenium oxide for electrochemical capacitors. Electrochimica Acta 46:3431-3444.

Huang, J.H., and J.S. Chen. 2001. Material characteristics and electrical property of reactively sputtered RuO2 thin films. Thin Solid Films 382:139-145.

Hug, S.J., and B. Sulzberger. 1994. In-situ Fourier-transform infrared spectroscopic evidence for the formation of several different surface complexes of oxalate on TiO2 in the aqueous-phase. Langmuir 10:3587-3597.

Hug, S.J., and D. Bahnemann. 2006. Infrared spectra of oxalate, malonate and succinate adsorbed on the aqueous surface of rutile, anatase and lepidocrocite measured with in situ ATR-FTIR. Journal of Electron Spectroscopy and Related Phenomena 150:208-219.

Iembo, A., F. Fuso, E. Arimondo, C. Ciofi, G. Pennelli, G.M. Curro, F. Neri, and M. Allegrini. 1997. Pulsed laser deposition and characterization of conductive RuO2 thin films. Journal of Materials Research 12:1433-1436.

Impellitteri, C.A., K.G. Scheckel, and J.A. Ryan. 2003. Sorption of arsenate and arsenite on RuO2•xH(2)O: A spectroscopic and macroscopic study. Environmental Science & Technology 37:2936-2940.

Ji, L., J. Lin, and H.C. Zeng. 2001. Thermal processes of volatile RuO2 in nanocrystalline Al2O3 matrixes involving gamma>alpha phase transformation. Chemistry of Materials 13:2403-2412.

Kaga, Y., Y. Abe, M. Kawamura, and K. Saski. 1999. Thermal stability of RuO2 Thin Films and effects of annealing ambient on their reduction process. Japanese Journal of Applied Physics 38:3689-3692.

Kim, H., I.R. de Moraes, G. Tremiliosi, R. Haasch, and A. Wieckowski. 2001. Chemical state of ruthenium submonolayers on a Pt(111) electrode. Surface Science 474:L203-L212.

Kosmulski, M. 2001. Chemical Properties of Material Surfaces Marcel Dekker, Inc., New York.

Kotz, R., H.J. Lewerenz, and S. Stucki. 1983. XPS studies of oxygen evolution on Ru and RuO_2 anodes. Journal of the Electrochemical Society 130:825-829.

Lasaga, A.C. 1981. Rate laws of chemical reactions, p. 1-66, *In* A. C. Lasaga and R. J. Kirkpatrick, eds. Reviews in Mineralogy, Vol. 8. Mineralogical Society of America,
Washington, DC.

Lasaga, A.C. 1998. Kinetic Theory in the Earth Sciences Princeton University Press, Princeton, NJ.

Lister, T.E., Y. Chu, W. Cullen, H. You, R.M. Yonco, J.F. Mitchell, and Z.U. Nagy. 2002a. Electrochemical and X-ray scattering study of well defined RuO2 single crystal surfaces. Journal of Electroanalytical Chemistry 524-525:201-218.

Lister, T.E., Y. Chu, W. Cullen, H. You, R.M. Yonco, J.F. Mitchell, and Z. Nagy. 2002b. Electrochemical and X-ray scattering study of well defined RuO2 single crystal surfaces. Journal of Electroanalytical Chemistry 524-525:201-218.

Long, J.W., K.E. Swider, C.I. Merzbacher, and D.R. Rolison. 1999. Voltammetric characterization of ruthenium oxide-based aerogels and other RuO2 solids: The nature of capacitance in nanostructured materials. Langmuir 15:780-785.

Lyons, M.E.G., and L.D. Burke. 1987. Mechanism of oxygen reactions at porous oxide Electrodes .1. Oxygen evolution at RuO2 and Ruxsn1-XO2 electrodes in alkaline-solution under vigorous electrolysis conditions. Journal of the Chemical Society-Faraday Transactions I 83:299-321.

Machesky, M.L., D.J. Wesolowski, D.A. Palmer, and M.K. Ridley. 2001. On the temperature dependence of intrinsic surface protonation equilibrium constants: An extension of the revised MUSIC model. Journal of Colloid and Interface Science 239:314-327.

Malek, J., A. Watanabe, and T. Mitsuhashi. 1996. Crystallization kinetics of amorphous RuO2. Thermochimica Acta 283:131-142.

McKenzie, K.J., and F. Marken. 2002. Electrochemical characterization of hydrous ruthenium oxide nanoparticle decorated boron-doped diamond electrodes. Electrochemical and Solid State Letters 5:E47-E50.

McKeown, D.A., P.L. Hagans, L.P.L. Carette, A.E. Russell, K.E. Swider, and D.R. Rolison. 1999. Structure of hydrous ruthenium oxides: Implications for charge storage. Journal of Physical Chemistry B 103:4825-4832.

Nagy, K.L. 1995. Dissolution and precipitation kinetics of sheet silicates, p. 173-234, *In* A. F. Whaite and S. L. Brantley, eds. Chemical weathering Rates of Silicate Minerals, Vol. 31. Mineralogical Society of America, Washington, D.C.

National Institute of Standards and Technology, U.S. 2002. NIST X-ray Photoelectron Spectroscopy Database: version 2.0 [Online]. Available by National Institute of Science and Technology http://www.nist.gov/srd/nist20.htm (posted 2003; verified 10-7).

Over, H., Y.D. Kim, A.P. Seitsonen, S. Wendt, E. Lundgren, M. Schmid, P. Varga, A. Morgante, and G. Ertl. 2000. Atomic-scale structure and catalytic reactivity of the RuO2(110) surface. Science 287:1474-1476.

Panias, D., M. Taxiarchou, I. Paspaliaris, and A. Kontopoulos. 1996. Mechanisms of dissolution of iron oxides in aqueous oxalic acid solutions. Hydrometallurgy 42:257-265.

Panic, V., A. Dekanski, S. Milonjic, R. Atanasoski, and B. Nikolic. 2000. The influence of the aging time of RuO2 and TiO2 sols on the electrochemical properties and behavior for the chlorine evolution reaction of activated titanium anodes obtained by the sol-gel procedure. Electrochimica Acta 46:415-421.

Panic, V., A. Dekanski, G. Wang, M. Fedoroff, S. Milonjic, and B. Nikolic. 2003. Morphology of RuO2-TiO2 coatings and TEM characterization of oxide sols used for their preparation. Journal of Colloid and Interface Science 263:68-73.

Park, J.H., and O.O. Park. 2002. Morphology and electrochemical behavior of ruthenium oxide thin film deposited on carbon paper. Journal of Power Sources 109:121-126.

Pauling, L. 1929. The principals determining the structure of complex ionic crystals. Journal of the American Chemical Society 51:1010-1026.

Predota, M., A.V. Bandura, P.T. Cummings, J.D. Kubicki, D.J. Wesolowski, A.A. Chialvo, and M.L. Machesky. 2004. Electric double layer at the rutile (110) surface. 1. Structure of surfaces and interfacial water from molecular dynamics by use of abinitio potentials. Journal of Physical Chemistry B 108:12049-12060.

S. Srinivasan, et al. (ed.) 1987. The Electrochemical Society, Pennington, NJ. The Elctrochemical Society INC.

Rard, J.A. 1985. Chemistry and Thermodynamics of Ruthenium and Some of Its Inorganic-Compounds and Aqueous Species. Chemical Reviews 85:1-39.

Ridley, M.K., M.L. Machesky, D.J. Wesolowski, and D.A. Palmer. 2004. Modeling the surface complexation of calcium at the rutile-water interface to 250 degrees C. Geochimica Et Cosmochimica Acta 68:239-251.

Rouquerol, F., J. Rouquerol, and K. Sing. 1999. Adsorption by Powders and & Porous Solids Academic Press, San Diego.

Scheckel, K.G., C.A. Impellitteri, and J.A. Ryan. 2004. Lead adsorption by ruthenium oxide: A macroscopic and spectroscopic study. Environmental Science & Technology 38:2836-2842.

Schwertmann, U., and R.M. Cornell. 2000. The Iron Oxides: Structures, Properties, Reactions, Occurences and Uses. 2nd ed. VCH, Weinheim, FR of Germany.

Sparks, D.L. 2003. Environmental Soil Chemistry. 2nd ed. Academic Press, Amsterdam.

Sunol, J.J., M.E. Bonneau, L. Roue, D. Guay, and R. Schulz. 2000. XPS surface study of nanocrystalline Ti-Ru-Fe materials. Applied Surface Science 158:252-262.

Suter, D., S. Banwart, and W. Stumm. 1991. Dissolution of hydrousiron(III) oxides by reductive mechanisms. Langmuir 7:809-813.

Trasatti, S. 1991. Physical Eelectrochemistry of ceramic oxides. Electrochimica Acta 36:225-241.

Trasatti, S. 1992. *In* G. H. and T. C. W, eds. Advances in Electrochemical Science and Engineering, Vol. 2. VCH, New York, NY.

Trasatti, S. 1994. *In* J. Lipkowski and P. N. Ross, eds. The Electrochemistry of Novel Materials. VCH, New York.

Trasatti, S., and G. Buzzanca. 1971. Ruthenium dioxide: a new interesting electrode material. Solid state structure and electrochemical behavior. Journal of Electroanalytical Chemistry 29:A1-A5.

Varshal, G.M., I.Y. Koshcheeva, M.V. Akhmanova, and V.A. Dorofeeva. 1983. Hydrolysis of ruthenium(IV) in perchlorate solutions. Journal of Analytical Chemistry of the USSR 38:1395-1403.

Wang, J.H., C.Y. Fan, Q. Sun, K. Reuter, K. Jacobi, M. Scheffler, and G. Ertl. 2003. Surface coordination chemistry: dihydrogen versus hydride complexes on RuO2(110). Angewandte Chemie-International Edition 42:2151-2154.

Williams, N.H., and J.K. Yandell. 1982. Outer-sphere electron-transfer reactions of ascorbate anions. Australian Journal of Chemistry 35:1133-1144.

Xue, T., and K. Osseoasare. 1989. Heterogeneous equilibria in the Ru-H2o, Ru-Cl-H2o and Ru-S-H2o systems. Journal of the Less-Common Metals 152:103-114.

Xyla, A.G., B. Sulzberger, G.W. Luther, J.G. Hering, P. Vancappellen, and W. Stumm. 1992. Reductive dissolution of manganese(III,IV) (hydr)oxides by oxalate - the effect of pH and light. Langmuir 8:95-103.

Zen, J.M., A.S. Kumar, and J.C. Chen. 2001. Electrochemical behavior of lead-ruthenium oxide pyrochlore catalyst: redox characteristics in comparison with that of ruthenium dioxide. Journal of Molecular Catalysis a-Chemical 165:177-188.

Zheng, J.P., and Y. Xin. 2002. Characterization of RuO2•xH(2)O with various water contents. Journal of Power Sources 110:86-90.

Zheng, J.P., and C.K. Huang. 2002. Electrochemical behavior of amorphous and crystalline ruthenium oxide electrodes. Journal of New Materials For Electrochemical Systems 5:41-46.

Zheng, J.P., P.J. Cygan, and T.R. Jow. 1995. Hydrous ruthenium oxide as an electrode material for electrochemical capacitor. Journal of the Electrochemistry Society 142:2699-2703.

Zinder, B., G. Furrer, and W. Stumm. 1986. The coordination chemistry of weathering .2. dissolution of Fe(III) oxides. Geochimica et Cosmochimica Acta 50:1861-1869.

ARSENATE ADSORPTION BY AMORPHOUS AND CRYSTALLINE RUTHENIUM OXIDES

ABSTRACT

The adsorption of arsenate on hydrous and crystalline ruthenium (Ru) oxides was investigated as a function of initial arsenate concentration, pH, and suspension density. Arsenate pH adsorption edges were similar in nature to those for arsenate adsorption on iron and aluminum oxides with maximum adsorption occurring at low pH. Arsenate is believed to form an inner-sphere complex with the Ru-oxide surface. Evidence for the inner-sphere complex is attributed to hydroxyl production upon the addition of arsenate to Ru-oxide suspensions and a shift in the point of zero charge to a lower pH upon addition of arsenate. At arsenate concentrations below 3 mM adsorption isotherms exhibited L-type Langmuir isotherm characteristics. At arsenate concentrations exceeding 3 mM the adsorption isotherm became linear, indicating either diffusion of arsenate into the crystal structure or the precipitation of a secondary phase. At concentrations below 3 mM arsenate the adsorption capacity of hydrous oxide ($RuO_2 \cdot xH_2O$) exceeded the crystalline material (RuO_2). Proton titrations indicate the differences were related to the quantity of reactive functional groups. At arsenate concentrations exceeding 3 mM the reverse was true. The increased adsorption capacity of RuO_2, at elevated arsenate concentrations, is believed to be related to the formation of secondary phase. Arsenate adsorption/desorption cycles indicated arsenate forms a strong inert surface complex with Ru-oxide surface not readily desorbed by 0.05 M NaOH.

INTRODUCTION

Arsenic contamination of groundwater and drinking water has been the subject of numerous scientific investigations examining the distribution, bonding, and partitioning between the solid/solution interface. Much of the research has been in response to arsenic's acute toxicity (NRC, 1999, 2001; USEPA, 2001) and the well documented and extensive contamination of groundwater, in Southeast Asia resulting in the poisoning of millions (Nordstrom, 2002; Smedley and Kinniburgh, 2002; Smith et al., 2002; Stollenwerk, 2003; Welch et al., 2000). The mobility, bioavailability, and toxicity of arsenic are related to its oxidation state. Arsenic most commonly occurs in soils and natural waters as a weakly acidic oxyanion in the form of arsenate (As(V); H_3AsO_4) in oxidized environments or arsenite (As(III); H_3AsO_3) under reducing conditions. However, research has demonstrated that arsenate may persist for extended periods of time in anoxic environments due to slow kinetics and biological transformations (Inskeep et al., 2002). Both arsenic species adsorb strongly to common soil and aquifer minerals (Sadiq, 1997). Furthermore, under oxidizing conditions sorption of arsenic by soil and aquifer colloids is the predominant means by which arsenic is sequestered (Sadiq, 1997; Singh, 2006; Smedley and Kinniburgh, 2002). Two of the most commonly used remediation techniques for removing and/or reducing arsenic concentrations in groundwater and drinking water utilize the strong affinity arsenic has for mineral colloid surfaces (Clifford and Ghurye, 2002). Arsenic adsorption to metal oxides, and (co)precipitation and coagulation of arsenic with iron(II) have both been used successfully to treat and remove arsenic from groundwater and drinking water (Clifford and Ghurye, 2002). The three most predominant metal (hydr)oxides used and researched for

remediation of elevated arsenic concentrations in drinking water and ground water are aluminum, manganese and iron (Arai et al., 2001; Bang et al., 2005; Beaulieu and Savage, 2005; Dixit and Hering, 2003; Farquhar et al., 2002; Goldberg and Johnston, 2001; Halter and Pfeifer, 2001; Lee et al., 2003; Manning et al., 1998; Meng et al., 2000; Su and Puls, 2001; Tournassat et al., 2002; Waychunas et al., 1993). Of these iron has received the most attention due to its natural abundance and its ability to adsorb large quantities of arsenic.

Recently, Impellitteri et al. (2003) investigated hydrous ruthenium oxide ($RuO_2 \bullet xH_2O$) as a potential metal oxide for arsenic adsorption. Their research examined arsenic adsorption and oxidation at pH 7 and demonstrated the increased sorption capacity of hydrous ruthenium oxide (amorphous Ru-oxide) compared to traditional metal oxide sorbents. Additionally, the authors demonstrated the rapid and complete oxidation of arsenite (As(III) to arsenate (As(V)) during adsorption. In the current study we further evaluate the effectiveness of ruthenium oxide as a potential metal oxide adsorbent for arsenate. The current objectives are: (1) determine the influence of pH, initial oxyanion concentration, and suspension density on arsenate adsorption over the pH range of 3 to 10; (2) evaluate changes in the surface charge of $RuO_2 \bullet x0H_2O$ and RuO_2 upon arsenate adsorption; and (3) determine the potential to desorb arsenate from $RuO_2 \bullet x0H_2O$ and RuO_2.

MATERIALS AND METHODS

Ruthenium Oxide Characterization

Crystalline (RuO_2) and amorphous ($RuO_2 \bullet xH_2O$) ruthenium oxide used in the current study were obtained from a Ruthenium(IV) oxide hydrate Premion® (99.99% pure metal basis) from Alfa Aesar (Ward Hill, MA). The ruthenium oxide hydrate was purged under positive pressure N_2 gas for 5 days to remove sorbed argon from the packaging process. Thermogravimetric and calorimetric analysis (DuPont Instruments Hi-Res TGA 2950 and DSC 2910, New Castle, DE) of the solid phase were used to determine the quantity of structural water associated with the amorphous phase and the temperature at which conversion from the amorphous material to crystalline material occurred. Results from the thermal analysis indicated 1.1 moles of water per mole of material yielding the chemical formula $RuO_2 \bullet 1.1H_2O$ for the amorphous material. Thermal analysis also indicated that amorphous material underwent a phase transformation to crystalline ruthenium oxide (RuO_2) at approximately 300^o C. After purging with N_2 gas $RuO_2 \bullet 1.1H_2O$ was used in the adsorption studies without any further treatments. The crystalline material was prepared by heating $RuO_2 \bullet 1.1H_2O$ to 500^o C for 24 hours in a muffle furnace. X-ray diffraction (Scintag® XDS 2000 X-ray Diffraction Spectrophotometer, Scintag Inc., Sunnyvale, CA) and differential scanning calorimetry data indicated a full conversion of $RuO_2 \bullet 1.1H_2O$ to crystalline RuO_2 with a rutile crystal structure. Specific surface area (SSA) of the samples was measured by a 5 point Brunauer-Emmet-Teller (BET) sorption isotherm using a Micromoretics ASAP2010 Surface Area Analyzer (Norcross, GA). The SSA was 100 and 50 $m^2\ g^{-1}$ for the$RuO_2 \bullet 1.1H_2O$ and RuO_2, respectively. Nitrogen adsorption isotherms indicated 15 $m^2\ g^{-1}$ of micro-porous surface area for $RuO_2 \bullet 1.1H_2O$ and less than 1 $m^2\ g^{-1}$ RuO_2. The point of zero charge (PZC) for the two solids was 4.2±0.1 and 5.6±0.1 for the $RuO_2 \bullet 1.1H_2O$ and RuO_2, respectively. The PZC was determined by measurement of the isoelctric point (IEP) using a Zetasizer 3000HSa (Malvern Instruments, Southborogh, MA). Proton titrations of amorphous and crystalline Ru-oxide conducted in 0.01, 0.05 and 0.1 M NaCl with a 5 g L^{-1} suspension density indicated the surface concentration of titratable functional

groups for each solid was 50 and 20 μmol m^{-2}, respectively. Titratable functional groups were defined by the micromole of acid and base consumed or produced by the solid phase during a titration from pH 2 to 11.

Batch Adsorption Experiments

Arsenate adsorption on ruthenium oxide was examined as a function of pH, arsenate concentration, ruthenium oxide crystallinity, and suspension density. Experiments were conducted in duplicate at a constant ionic strength (0.01 M NaCl) using a pH-monitored stirred-batch reactor. For the adsorption experiments an appropriate quantity of N_2 sparged ruthenium oxide was weighed into a 500 mL glass beaker to which 350 mL of 0.01 M NaCl was added. The suspension was dispersed for ~2min using an ultrasonic dimembrator. The beaker was placed in a water jacketed reaction vessel kept at 25° C, stirred using a Teflon coated magnetic stir bar, and kept under positive pressure with N_2 gas to eliminate CO_2. The suspension was allowed to hydrate for a period of 24 h while the pH was adjusted to the appropriate value using a Brinkman® 716 Stat-Trino pH stat (Brinkman Instruments, Westbury, NY) (with either 0.1 M HCl or NaOH). After the hydration period an appropriate quantity of a pH adjusted 100 mM arsenate stock solution (made from a reagent grade sodium arsenate salt) was added to the reactor to achieve the desired arsenate concentration. The total volume was brought to 400 mL and a pH stat was used to maintain the appropriate pH. After three hours a 10 mL sample was removed and filtered through a 0.05 μm Millipore nitrocellulose filter (Billerica, MA) and the quantity of 0.1 M HCl added was recorded. The filtrate was analyzed by inductively coupled plasma atomic emission spectroscopy (ICP-AES) (SpectroFlame FTMOA85D, Spectro Analytical Instruments, Fitchburg, MA). The detection limit on the SpectroFlame ICP-AES for As and Ru was 10 and 12 μg L^{-1}, respectively. The quantity of oxyanion adsorbed was determined by subtracting the initial oxyanion concentration from the measured concentration.

Arsenate pH adsorption edges were conducted over a broad pH range (3-10) for 2 suspension densities (0.5 and 2 g L^{-1}). For the 0.5 g L^{-1} suspension density three initial arsenate concentrations were investigated 0.040, 0.120, 0.240 mM (3.00, 9.00, and 18.50 mg L^{-1}). For the 2 g L^{-1} suspension density one arsenate concentration was investigated 0.961 mM (72 mg L^{-1}). Adsorption experiments started at pH 10 and preceded to pH 3 to avoid hysteresis effects associated with arsenate desorption with increasing pH. After the addition of arsenate to the reactor the pH was adjusted to 10 and the system was allowed to equilibrate for 3 h. The equilibration time period was based on previous research (Impellitteri et al., 2003). After the equilibration time period two 10 mL samples were removed from the reactor for solution and zeta potential analysis. After sampling, the volume of titrant was recorded and the suspension was lowered one pH unit with 0.1 M HCl and allowed to re-equilibrate.

Arsenate adsorption isotherms were conducted at two different suspension densities (0.5 and 2 g L^{-1}). The 0.5 g L^{-1} suspension density was conducted at pH 4, 5, and 6 over a range of arsenate concentrations from 0.0131 to 0.667 mM (1 to 50 mg L^{-1}), while the 2.0 g L^{-1}, suspension density was conducted at pH 5 from 0.167 to 33.368 mM (12.5-2500 mg L^{-1}). In between arsenate additions, the suspension was allowed to equilibrate for three hours. After three hours, two 10 mL samples were removed for solution analysis and zeta potential analysis.

Zeta Potential Analysis

Zeta potentials were calculated from microelectrophoresis measurements collected using a Malvern Zetasizer 3000HSa (Malvern Instruments, Southborogh, MA). Based on preliminary data, the voltage applied to the capillary cell was set at 100 mV and a Henry function ($f(K_a)$) of 1.5 to 1.23 was used to calculate zeta potential. The pH of each sample was measured prior to zeta potential measurement to account for any drift in pH. The reported zeta potential values are the average of 10 microelectrophoresis measurements. The standard deviation for all zeta potential measurements was less 1.5 mV.

Arsenate Adsorption/Desorption Cycles

Three separate arsenate adsorption and desorption cycles were conducted for the $RuO_2 \cdot 1.1H_2O$ and RuO_2. Initially, 23 mg of Ru-oxide was weighed into a 50 mL glass beaker, to which 25 mL of pH 5 adjusted 0.01 M NaCl was added. The resulting suspension was sonicated for ~2 min. The suspension was filtered on to a 0.22 μm Millipore nitrocellulose filter enclosed in a glass filter tower. The suspension was placed under a controlled vacuum pressure that resulted in a flow rate of 0.75 mL min^{-1}. After filtration, two 15 mL aliquots of a 4 mg L^{-1} arsenate solution (adjusted to pH 5) were added to the filter tower and leached through the previously deposited Ru-oxide at the same flow rate. Each 15 mL sample was analyzed separately for As and Ru using ICP-AES. After collection of the second arsenate adsorption sample, the Ru-oxide material was washed with 3 mL of pH 5 adjusted 0.01 M NaCl to remove entrained arsenate. The washing process was repeated five times, and the resulting leachate (total of 15 mL) was collected and analyzed for As and Ru. After the addition of the 0.01 M NaCl, the Ru-oxide was leached twice with 15 mL of 0.05 M NaOH to promote arsenate desorption. Each 15 mL leachate sample was analyzed separately. After the addition of NaOH, the oxide material was washed using the same procedure previously outlined. The entire process (adsorption, wash, desorption, wash) was repeated three times for the amorphous and crystalline material.

RESULTS AND DISCUSSION

pH Adsorption Edges

The pH adsorption edges for arsenate (three concentrations) on $RuO_2 \cdot 1.1H_2O$ and RuO_2 are presented in Figure 3-1. The adsorption edge is similar to arsenate adsorption on other oxides with maximum adsorption occurring at low pH. However, unlike most pH adsorption data reported for arsenate adsorption on amorphous and crystalline iron and aluminum oxides, there is no detectable adsorption above pH 9 (Dixit and Hering, 2003; Goldberg and Johnston, 2001; Halter and Pfeifer, 2001; Jain and Loeppert, 2000; Manning et al., 1998; Meng et al., 2000; Swedlund and Webster, 1999). Throughout the pH adsorption edge there was a net production of hydroxyls. Typically a net increase in hydroxyl ion concentration during an adsorption reaction is associated with a ligand exchange mechanism where a surface hydroxyl group is replaced by an oxygen of the adsorbing oxyanion resulting in a inner-sphere bond (McBride, 1994; Sparks, 1999; Sposito, 1989). The adsorption capacity of RuO2 was substantially less than $RuO_2 \cdot 1.1H_2O$ as arsenate concentration increased from 0.040 to 0.240 mM (Figure 3-1A). At pH 3 and 4 $RuO_2 \cdot 1.1H_2O$ removed more than 98% of the 0.040 mM (3

mg L^{-1}) arsenate which resulted in surface concentrations of 3.00 mg g^{-1} (0.45 μmol m^{-2}) (Figure 3-1B). The complete removal of 3 mg L^{-1} of arsenate by 0.5 grams of RuO_2•1.1H_2O was equal to or slightly less than the mass of ferrihydrite and much less than the mass of amorphous aluminum oxide required to removed an equal quantity of arsenate (Clifford and Ghurye, 2002; Dixit and Hering, 2003; Halter and Pfeifer, 2001; Jain and Loeppert, 2000; Manning et al., 1998; O'Reilly et al., 2001; Swedlund and Webster, 1999).

Figure 3-2 presents arsenate adsorption on RuO_2•1.1H_2O at two different suspension densities. The ratio of arsenate (mM) to mass of ruthenium (g) is the same for both data sets, yet the 2 g L^{-1} suspension sequesters a greater concentration of arsenate with decreasing pH. The difference between the surface concentrations highlights the importance of suspension density in evaluating adsorption data and developing effective arsenate remediation strategies.

Arsenate Adsorption Isotherms

Adsorption of arsenate as a function of solution concentration was evaluated in order to determine the adsorption maximum for the Ru-oxide surface. Arsenate adsorption isotherms were conducted at various pH values, and suspension densities. Figure 3-3 shows the adsorption isotherms for arsenate at three pH values for the 0.5 g L^{-1} suspension density. The maximum solution concentration of arsenate that results in complete removal of the aqueous phase was 3.2 mg L^{-1} RuO_2•1.1H_2O at pH 4 (Figure 3-3A, inset). The amorphous material had a much greater adsorption capacity compared to the RuO_2 (Figure 3-3A). Even on a surface normalized basis (Figure 3B) the adsorption capacity of RuO_2•1.1H_2O exceeds the adsorption capacity of the RuO_2 by 3.3 μmol m^{-2} or 251 mg m^{-2} which translates to the adsorption of an additional 0.0125 g of arsenate. The differences in the adsorption maximum of the two phases are typical of the differences seen between the adsorption capacities of amorphous and crystalline materials due a reduction in surface area and reactive surface site density. The difference between the densities of reactive functional groups was determined from acid base titrations during zeta potential analysis of the bare Ru-oxide surface. Titration data indicated that there were 50 μmol m^{-2} of titratable functional groups for RuO_2•1.1H_2O and 20 μmol m^{-2} RuO_2, demonstrating the increased number of reactive surface groups per meter squared available for arsenate adsorption.

In addition to the 0.5 g L^{-1} suspension density an arsenate adsorption isotherm was conducted on a 2 g L^{-1} suspension density with initial arsenate concentrations up to 33.3 mM (2500 mg L^{-1}) (Figure 3-4). At low arsenate concentrations RuO_2•1.1H_2O sequesters a greater quantity of arsenate as was demonstrated for the 0.5 g L^{-1} suspension density (Figure 3-4, inset). However, as arsenate concentrations continue to increase, the adsorption capacity of the RuO_2 began to exceed the adsorption capacity of RuO_2•1.1H_2O. Both of the solids exhibit a linear growth when arsenate surface concentrations exceed 4.0 and 2.3 μmol m^{-2} for RuO_2•1.1H_2O and RuO_2, respectively. Two theories have been proposed for the linear portions of the adsorption isotherms observed on oxide surfaces, diffusion or penetration of the ions into the crystal or amorphous material, and the formation of a secondary precipitate (Hingsten et al., 1972; Krauskopf and Bird, 1995; McBride, 1994). Diffusion of arsenate into RuO_2•1.1H_2O structure is a possibility, but not for RuO_2 where it is more likely arsenate forms a secondary phase on the Ru-oxide surface due to the absence of any micro-porosity. The precipitation of a secondary phase also seems likely due to the presence of over 30 μmol m^{-2} of adsorbed arsenate on a surface with 20 μmol m^{-2} of titratable functional groups. Recent research has suggested that secondary or precipitated arsenate phases on aluminum and iron oxide surfaces results from

precipitation of amorphous metal arsenates involving the oxide metal cation. These phases resemble scorodite ($FeAsO_4 \bullet H_2O$) and esperanzaite ($NaCa_2Al_2(AsO_4)_2F_4(OH) \bullet H_2O$) crystalline metal arsenate oxides (Beaulieu and Savage, 2005; Jia et al., 2006). The presence or absence of a secondary arsenate phase alone cannot be confirmed from macroscopic data, but requires molecular level information gathered using microscopic or spectroscopic techniques.

Direct comparison of arsenate adsorption on Ru-oxides and published data on common Fe, Mn, and Al oxides is difficult due to the nature of the adsorption reaction. Ultimately the quantity of ion adsorbed will be a function of pH, initial adsorbate concentration, oxide surface morphology, solid:solution ratio and potentially ionic strength. Normalizing the data for mineral or oxide relative to SSA helps to alleviate the problem but still makes direct comparisons difficult. A broad survey of the literature evaluating arsenate adsorption onto various natural and engineered materials indicates the sorption capacity of Ru-oxide exceeds most other materials (Table 3-1). Three different initial concentrations of arsenate, spanning three orders of magnitude, and the corresponding surface concentration are listed for the current study, to enable a more appropriate comparison with literature data. For all three arsenate concentrations the quantity of arsenate adsorbed to the Ru-oxide phase was equal to or exceeded literature values demonstrating the large sorption capacity of Ru-oxides, compared to iron, aluminum, and manganese oxides.

Zeta Potential Analysis

Changes in the surface potential of oxide minerals at a specific pH or a shift in the oxides point of zero charge (PZC) due to adsorbing cations and anions can be used as an indirect method for elucidating reaction mechanisms. A decrease in the surface potential of $RuO_2 \bullet 1.1H_2O$ and RuO_2 with the addition arsenate would suggest the formation of an inner-sphere complex. The decrease in the surface potential or (PZC) results from the adsorption of ions with protonizable functional groups. The adsorbed complex can undergo protonation/deprotonation reactions that will contribute to particle charge and surface potential (Anderson and Malotky, 1979). In addition to providing indirect information on oxyanion bonding mechanism, zeta potential measurements can be used to determine the stability of the oxide suspension and the potential for oxide flocculation (Kosmulski, 2001; Stumm, 1992). Zeta potential measurements for $RuO_2 \bullet 1.1H_2O$ and RuO_2 were collected from pH 3 to 10, in the presence of 0.00, 0.040, 0.120, and 0.24 mM arsenate (Figure 3-5). The isoelectric point (IEP) or PZC of the two Ru-oxides in the absence of arsenate was 4.2 and 5.6 for the amorphous and crystalline material, respectively. The increase in the PZC from the amorphous to the crystalline phase is a common feature of iron and aluminum oxides and represents a decrease in the acidity of surface functional groups (Kosmulski, 2001). The addition of arsenate to either Ru-oxide phase resulted in a decrease in the PZC, suggesting that arsenate forms an inner-sphere complex with Ru-oxide. The continued decrease in the PZC with successive additions of arsenate provides an additional line of evidence for the formation of an inner sphere surface complex.

The barren RuO_2 surface (no arsenate) exhibits a more negative shear plane potential at pH values greater than 6, compared to the crystalline surface with arsenate adsorbed (Figure 3-5). This is in contrast to the shear plane potential for $RuO_2 \bullet 1.1H_2O$ and the general oxyanion adsorption trends as a function of oxyanion surface concentration (i.e. increased negative shear plane potential with increasing oxyanion surface concentration) (Kosmulski, 2001). The reason for the increased negative potential for the barren surface is not readily understood, but may be

related to the oxidation of ruthenium from the electric field applied by the instrument at high pH. Ruthenium oxides have received an enormous amount of attention in material science due to their ability to act as electrode catalysts for multi-electron reactions by readily undergoing reversible redox reactions. The transition between oxidation states (Ru(III) ↔ Ru(IV) ↔ Ru(VI)) is a function of numerous factors including crystallinity, embathing solution, and applied electric potential. In basic media the transition between Ru(IV) and Ru(VI) in crystalline Ru-oxides is reversible and occurs at applied potentials between -50 and -100 mV(Lister et al., 2002; McKenzie and Marken, 2002). Ru-oxides typically contain small quantities of Ru(VI) due to coordinatively unsaturated sites (cus) formed during the crystallization process (Kotz et al., 1983; Over et al., 2000; Rard, 1985). The application of the applied potential during zeta potential analysis may have caused Ru(IV) oxidation and subsequent Ru(VI) reduction resulting in the development of an increased negative surface potential. The absence of the Ru oxidation step has been reported for Ru-oxides embathed in phosphate buffer solutions due to phosphate adsorption (McKenzie and Marken, 2002). The same inhibitory affect may result from arsenate adsorption.

Arsenate Adsorption Desorption Cycles

Arsenate adsorption and desorption cycles on $RuO_2 \cdot 1.1H_2O$ and RuO_2 were conducted to evaluate arsenate desorption by hydroxyls for beneficial reuse of the material. The Ru-oxides were subjected to three consecutive adsorption/desorption cycles. Sodium hydroxide was used as the desorbent based on the results of the pH adsorption isotherms which indicated little to no arsenate adsorption above pH 9 for either material (Figure 3-1). The surface concentration of arsenate increased with each adsorption cycle, indicating the Ru-oxide surface was not saturated with respect to arsenate over the three adsorption/desorption cycles (Figure 3-6A). In contrast to the adsorption data, the quantity of arsenate desorbed by hydroxyls decreased for each cycle of $RuO_2 \cdot 1.1H_2O$, and remained fairly constant for RuO_2 after the first cycle (Figure 3-6B).

During the first desorption cycle there was a small quantity of Ru present in the leachate (Figure 3-6C). The mass of ruthenium collected in the leachate accounted for 0.05 mg and 0.12 mg of the initial 23 mg of $RuO_2 \cdot 1.1H_2O$ and RuO_2 deposited on the filter paper. For $RuO_2 \cdot 1.1H_2O$ there is a relationship between the quantity of Ru and As in the leachate (Figure 3-6B and C). The relationship between the two ion concentrations suggests that the arsenate release was due to dissolution $RuO_2 \cdot 1.1H_2O$, and not to desorption by hydroxyls. For RuO_2 there is an initial spike in Ru concentration in the first desorption cycle 5 times greater than the amorphous Ru-oxide. The reason for the increased in the crystalline material as compared to the amorphous material is not clear, but may be related to ultra fine particles created during the crystallization process or oxidation of cus-Ru formed during heating of $RuO_2 \cdot 1.1H_2O$. The spike in the Ru concentration does provide a source of Ru available for precipitation of a secondary phase. The lack of any significant quantity of arsenate material suggests that the adsorbed complex is stable and fairly inert to changes in pH over short time periods. Preliminary data evaluating a longer hydroxyl contact time indicates that over a several hour period hydroxide is able to effectively desorb arsenate from the amorphous Ru-oxide.

SUMMARY

The current study evaluated the potential use of Ru-oxides as a sorbent material for arsenate. Results from the adsorption/desorption studies and zeta potential measurements suggests arsenate forms a strong inert inner-sphere complex with Ru-oxides. The formation of an inner-sphere complex is supported by: (1) hydroxyl production upon introduction of arsenate to amorphous and crystalline Ru-oxide suspensions between pH 3 and 9, (2) a decrease in the PZC of both Ru-oxides after the addition of arsenate as determined by zeta potential measurements, and (3) the inability to desorb with hydroxyls in a pH environment not conducive for arsenate adsorption.

At initial arsenate solution concentrations below 3 mM (225 mg L^{-1}) $RuO_2 \bullet 1.1H_2O$ exceeded the adsorption capacity of RuO_2 on a surface area basis. At concentrations exceeding 3 mM the reverse was true. Both the amorphous and crystalline phase exhibited a linear growth for the 2g L^{-1} suspension density at surface concentrations exceeding 2.7 and 1.1 μmol m^{-2}, respectively. Diffusion of arsenate in to the crystal structure is suspected for $RuO_2 \bullet 1.1H_2O$, and the formation of a secondary precipitate is suspected for RuO_2. Data presented in the current study demonstrate that Ru-oxides have a large sorption capacity for arsenate. The material would appear to be most effective used under acidic conditions due to the relatively low PZC of $RuO_2 \bullet 1.1H_2O$ and RuO_2, 4.2 and 5.6, respectively.

TABLES

Table 3-1 Comparison of the surface normalized adsorption capacity of various solid phases with respect to arsenate adsorption. Experimental values for the initial arsenate solution concentration, suspension density, and pH are provided for comparative purposes.

Initial As Conc. (mM)	As Sorbed (μmol m^{-2})	suspension density	pH	Solid Phase	Reference
33.00	34.72	2.0	5	Ruthenium Oxide	This Study
33.00	31.35	2.0	5	Hydrous Ruthenium Oxide	This Study
3.00	3.80	2.0	5	Ruthenium Oxide	This study
3.00	4.02	2.0	5	Hydrous Ruthenium oxide	This study
0.25	1.00	0.5	3	Ruthenium Oxide	This Study
0.25	2.33	0.5	3	Hydrous Ruthenium Oxide	This study
32.00	31.00	0.011	6	12 nm Magnetite	(Mayo et al., 2007)
0.02	13.00	0.0	6.8	Iron Coagulation	(Meng et al., 2000)
130.00	12.37	10.0	4.2	Ferrihydrite	(Raven et al., 1998)
26.70	6.11	0.5	4.2	Ferrihydrite	(Dixit and Hering, 2003)
1.33	3.79	24.4	9.5	Zero Valent Iron	(Su and Puls, 2001)
12.50	3.70	0.5	4.2	Goethite	(Dixit and Hering, 2003)
1.00	3.16	1.0	3	Ferrihydrite	(Grafe et al., 2002)
600.00	2.63	150.0	5.5	Goethite	(Sun and Doner, 1996)
0.40	2.39	1.6	6	Goethite	(Lenoble et al., 2002)
3.00	2.25	10.0	6	Goethite	(O'Reilly et al., 2001)
0.27	2.06	2.5	3	Goethite	(Manning and Goldberg, 1996)
2.67	1.65	40.0	5	Kaolinite	(Mohapatra et al., 2007)
0.27	1.55	2.5	3	Gibbsite	(Manning and Goldberg, 1996)
0.70	1.40	5.0	5	γ Aluminum Oxide	(Arai et al., 2001)
0.40	1.36	1.6	6	Ferrihydrite	(Lenoble et al., 2002)
2.67	1.19	40.0	5	Illite	(Mohapatra et al., 2007)
N/A	0.76	N/A	7	Mn Substituted Goethite	(Lakshmipathiraj et al., 2006)
2.67	0.64	40.0	5	Smectite	(Mohapatra et al., 2007)
0.30	0.57	2.4	4.7	Brinessite	(Foster et al., 2003)
N/A	0.17	N/A	N/A	Fe^{2+} Impregnated Meso-Carbocarbon	(Gu and Deng, 2007)

N/A, indicates data was not included in the publication.

FIGURES

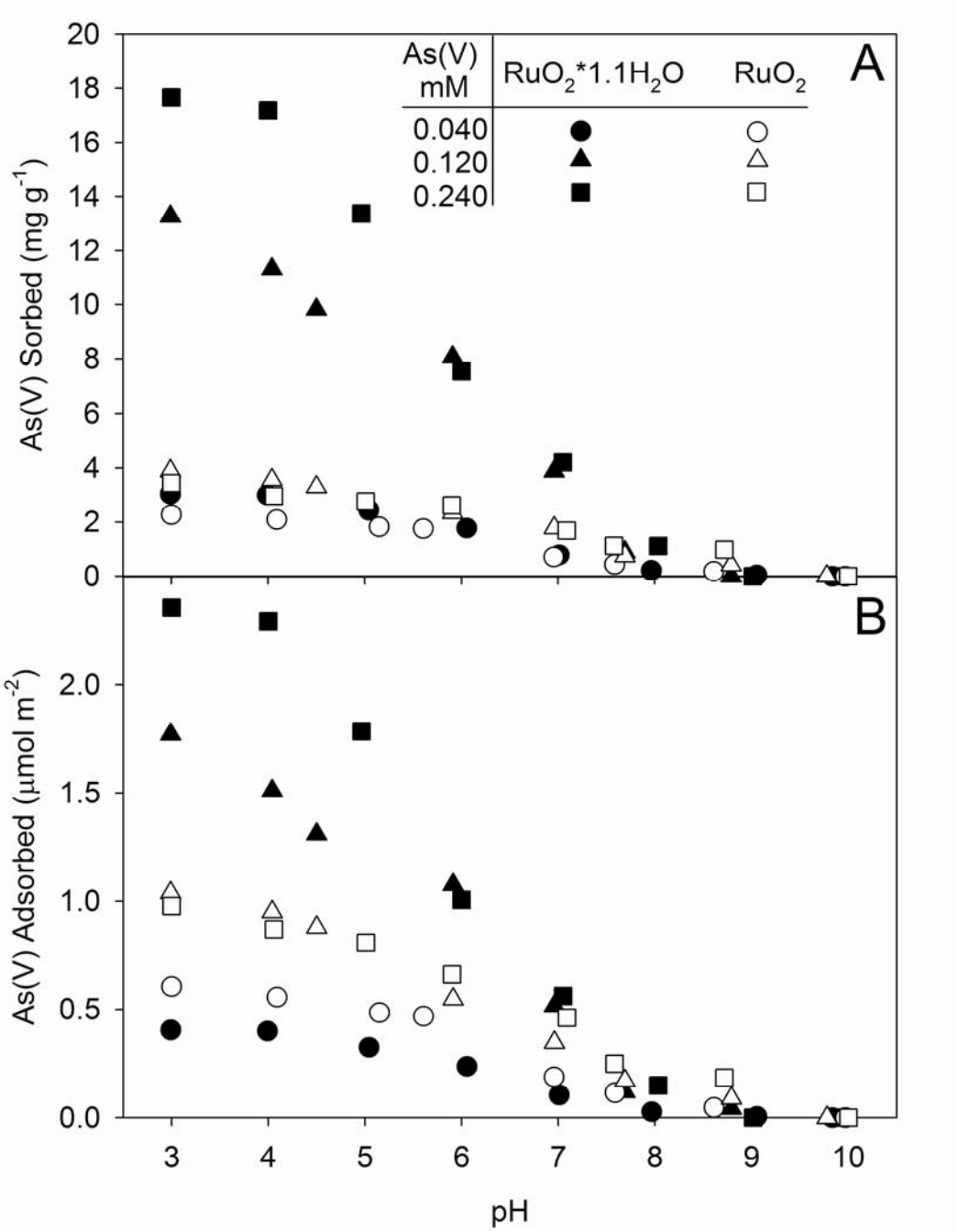

Figure 3-1 Arsenate adsorption edges on RuO_2•1.1H_2O and RuO_2 at three initial arsenate concentrations. (A) Mass of arsenate sorbed per gram of solid. (B) Surface concentration of arsenate. Suspension density 0.5 g L^{-1}.

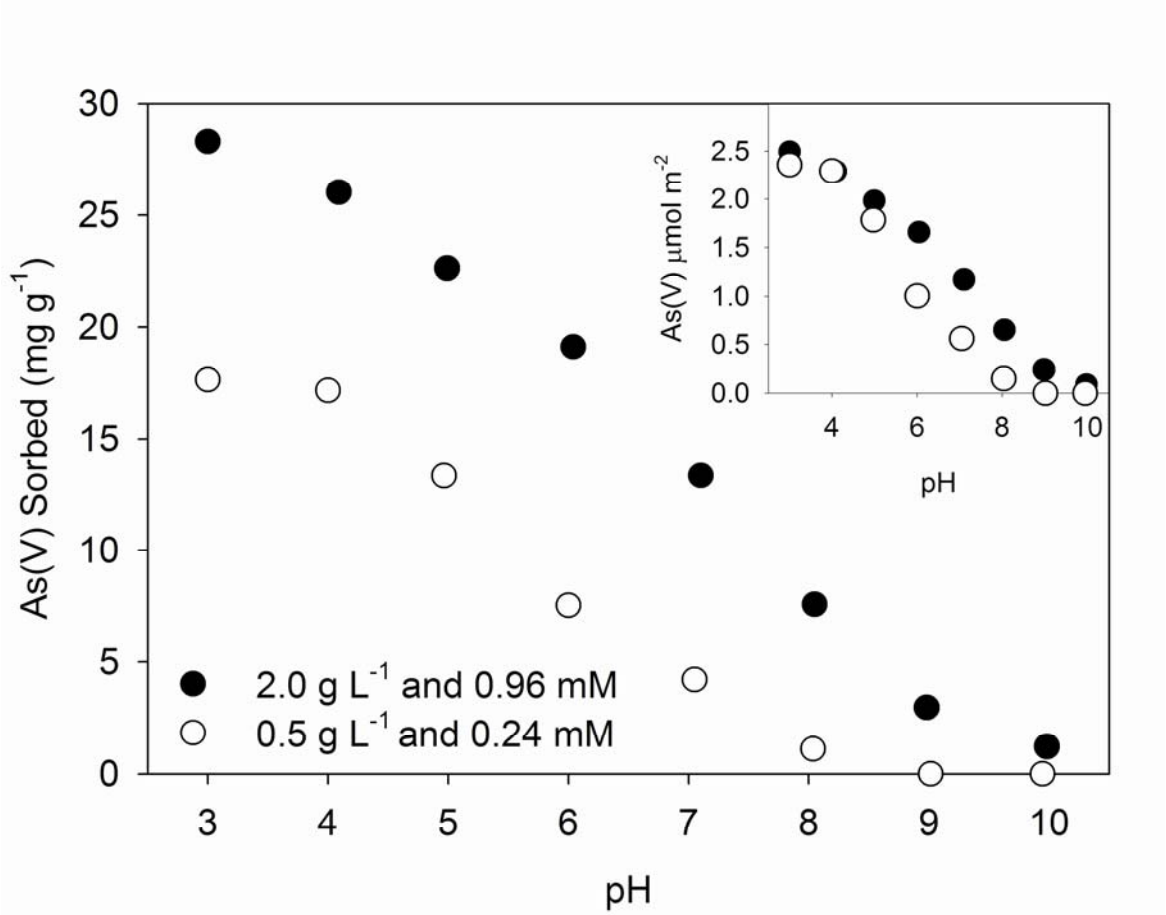

Figure 3-2 Arsenate adsorption edges on RuO_2•1.1H_2O at two different suspension densities. Inset shows surface concentration of arsenate.

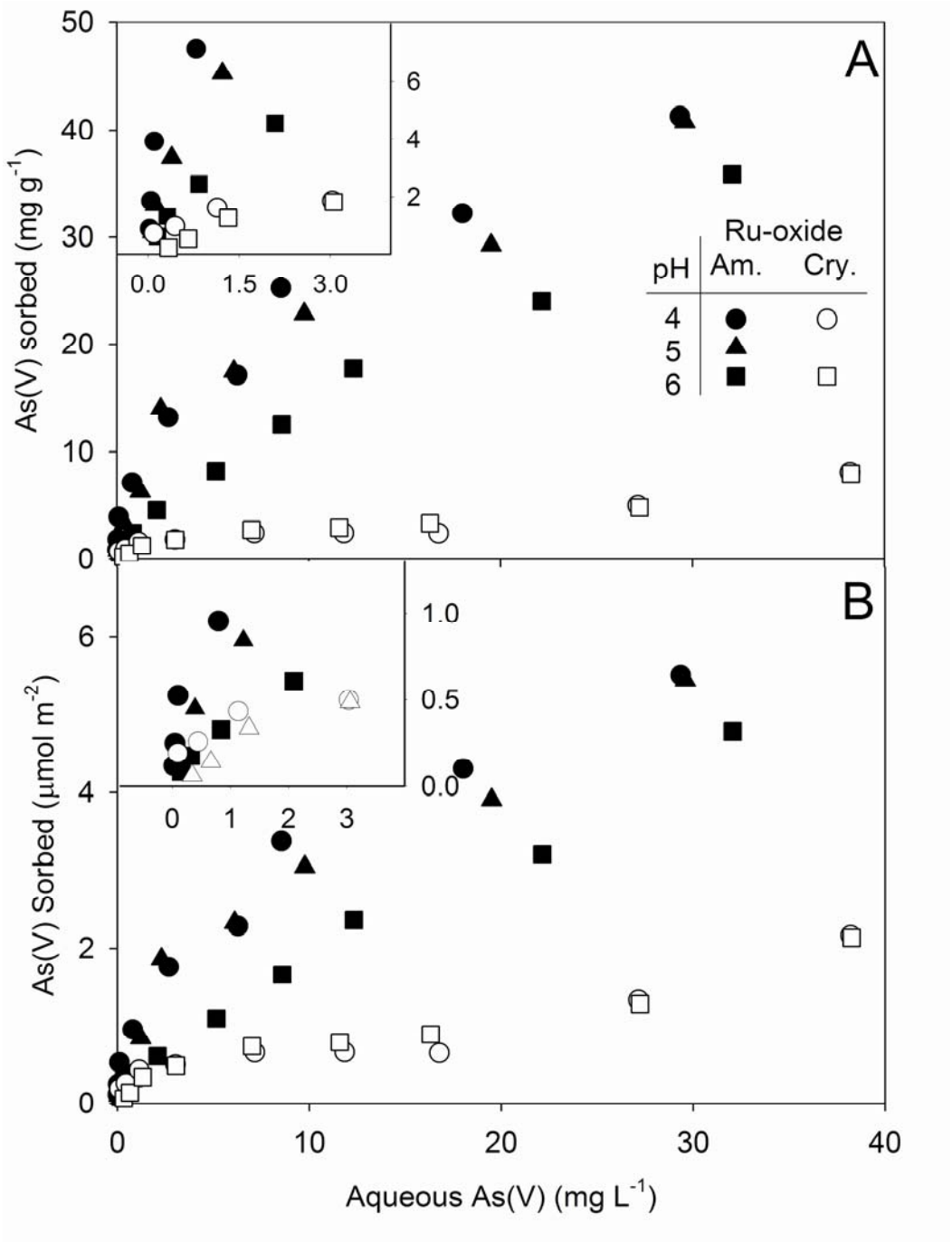

Figure 3-3 Arsenate adsorption isotherms for the 0.5 g L^{-1} suspension density for RuO_2•1.1H_2O(Am.) and RuO_2 (Cry.) at various pH values. (A) Adsorption isotherm for arsenate. (B) Surface area normalized adsorption isotherm. Inset for A and B shows the adsorption isotherm from 0 to 3 mg L^{-1} arsenate, axes the same

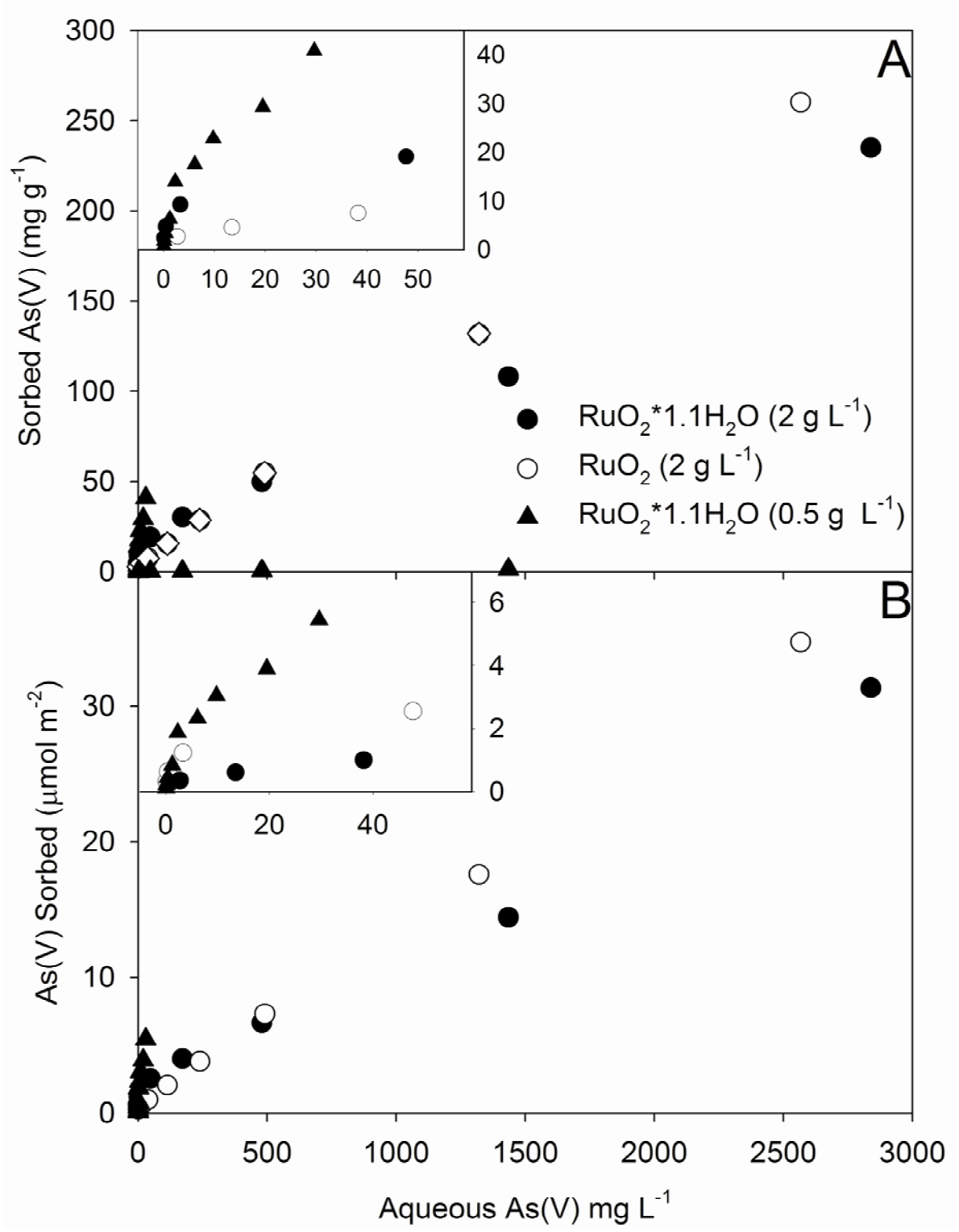

Figure 3-4 Arsenate adsorption isotherm for 0.5 and 2.0 g L^{-1} suspension density at pH 5. (A) Mass basis and (B) Surface area normalized basis. Inset figures show lower solution concentration sorption data, axes are the same.

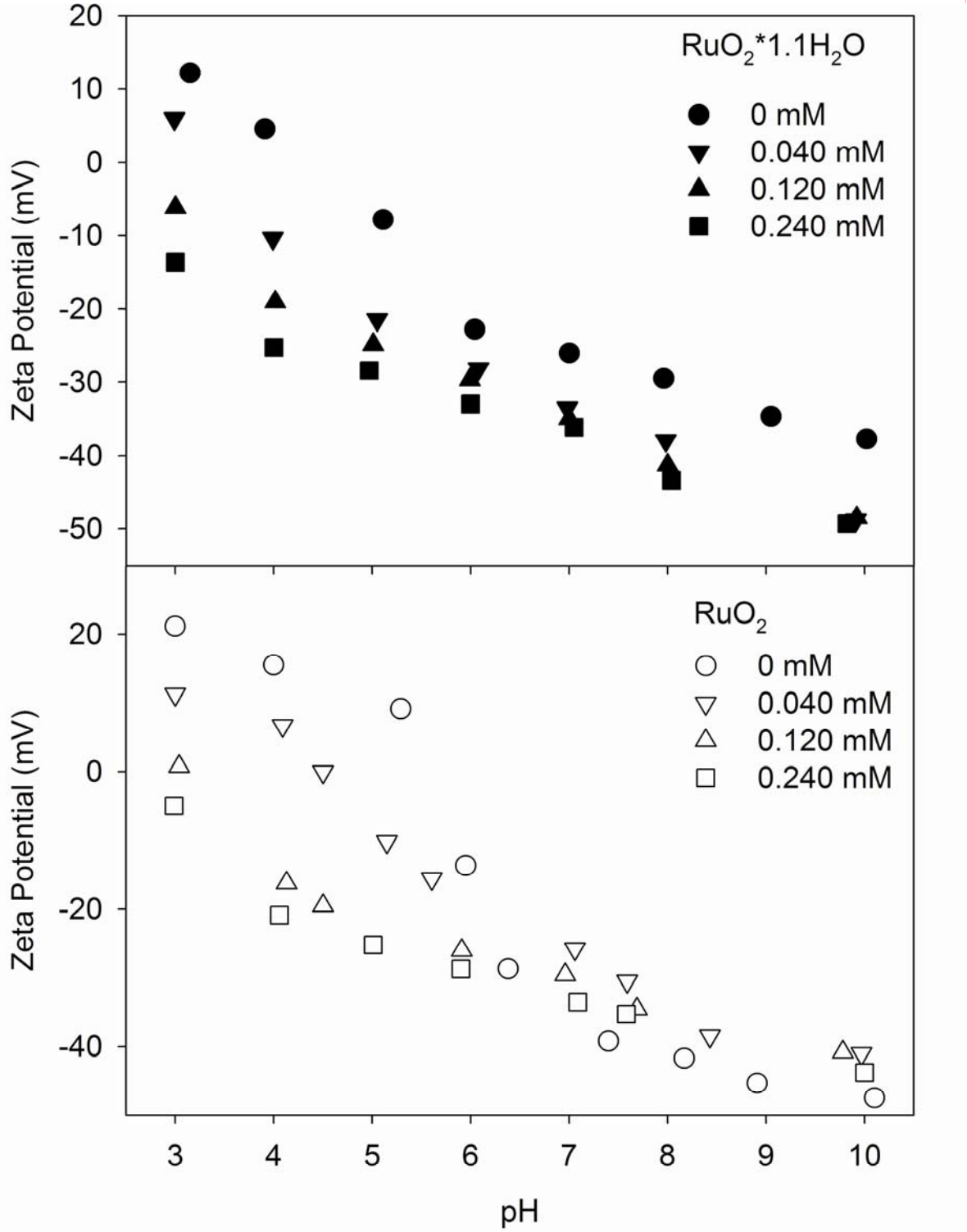

Figure 3-5 Zeta potential measurements for arsenate adsorption edges on RuO_2•1.1H_2O and RuO_2. Suspension density 0.5 g L^{-1}.

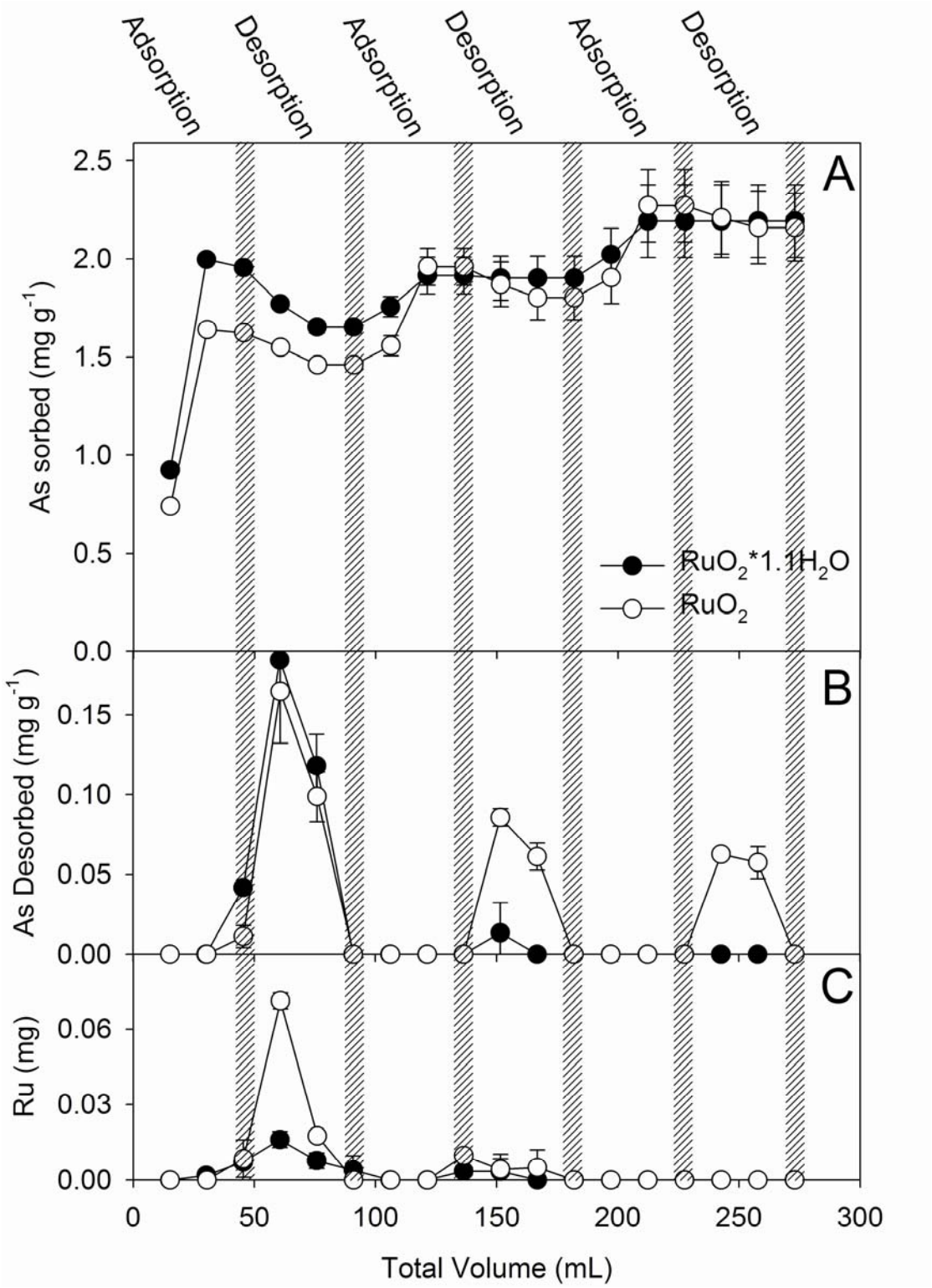

Figure 3-6 Arsenate adsorption and desorption cycles on RuO_2•1.1H_2O and RuO_2. Grey area refers to 15 mL 0.01 M NaCl wash to remove entrained Aresenate and Hydroxyls. Data corrected for the entrained concentration of arseante following an adsorption or desorption cycle. (A) Surface concentration of arsenate. (B) Mass of arsenate desorbed by 0.005 M NaOH. (C) Mass of ruthenium leached or dissolved.

REFERENCES

Anderson, M.A., and D.T. Malotky. 1979. The adsorption of protolyzable anions in hydrous oxides at the isoelectric pH. Journal of Colloid and Interface Science 72:413-427.

Arai, Y., E.J. Elzinga, and D.L. Sparks. 2001. X-ray absorption spectroscopic investigation of arsenite and arsenate adsorption at the aluminum oxide-water interface. Journal of Colloid and Interface Science 235:80-88.

Bang, S., M.D. Johnson, G.P. Korfiatis, and X.G. Meng. 2005. Chemical reactions between arsenic and zero-valent iron in water. Water Research 39:763-770.

Beaulieu, B.T., and K.S. Savage. 2005. Arsenate adsorption structures on aluminum oxide and phyllosilicate mineral surfaces in smelter-impacted soils. Environmental Science & Technology 39:3571-3579.

Clifford, D.A., and G.L. Ghurye. 2002. Metal-oxide adsorption, ion exchange, and coagulation-microfiltration for arsenic removal from water, *In* W. T. Frankenberger, ed. Environmental Chemistry of Arsenic. Marcel Dekker, Inc., New York.

Dixit, S., and J.G. Hering. 2003. Comparison of arsenic(V) and arsenic(III) sorption onto iron oxide minerals: Implications for arsenic mobility. Environmental Science & Technology 37:4182-4189.

Farquhar, M.L., J.M. Charnock, F.R. Livens, and D.J. Vaughan. 2002. Mechanisms of arsenic uptake from aqueous solution by interaction with goethite, lepidocrocite, mackinawite, and pyrite: An X-ray absorption spectroscopy study. Environmental Science & Technology 36:1757-1762.

Foster, A.L., G.E. Brown, Jr., and G.A. Parks. 2003. X-ray absorption fine structure study of As(V) and Se(IV) sorption complexes on hydrous Mn oxides. Geochimica et Cosmochimica Acta 67:1937-1953.

Goldberg, S., and C. Johnston. 2001. Mechanisms of arsenic adsorption on amorphous oxides evaluated using macroscopic measurements, vibrational spectroscopy, and surface complexation modeling. Journal of Colloid and Interface Science 234:204-216.

Grafe, M., M.J. Eick, P.R. Grossl, and A.M. Saunders. 2002. Adsorption of arsenate and arsenite on ferrihydrite in the presence and absence of dissolved organic carbon. Journal of Environmental Quality 31:1115-1123.

Gu, Z.M., and B.L. Deng. 2007. Use of iron-containing mesoporous carbon (IMC) for arsenic removal from drinking water. Environmental Engineering Science 24:113-121.

Halter, W.E., and H.R. Pfeifer. 2001. Arsenic(V) adsorption onto alpha-Al2O3 between 25 and 70 degrees C. Applied Geochemistry 16:793-802.

Hingsten, F.J., A.M. Posner, and J.P. Quirk. 1972. Anion adsorption by goethite and gibbsite I. The role of the proton in determining adsorption envelopes. Journal of Soil Science 23:177-192.

Impellitteri, C.A., K.G. Scheckel, and J.A. Ryan. 2003. Sorption of arsenate and arsenite on RuO2•xH(2)O: A spectroscopic and macroscopic study. Environmental Science & Technology 37:2936-2940.

Inskeep, W.P., T.R. McDermott, and S.E. Fendorf. 2002. As(V)/(III) cycling in soils and natural waters: chemical and microbiological processes, *In* W. T. Frankenberger, ed. Environmental Chemistry of Arsenic. Marcel Dekker, Inc., New York.

Jain, A., and R.H. Loeppert. 2000. Effect of competing anions on the adsorption of arsenate and arsenite by ferrihydrite. Journal of Environmental Quality 29:1422-1430.

Jia, Y.F., L.Y. Xu, Z. Fang, and G.P. Demopoulos. 2006. Observation of surface precipitation of arsenate on ferrihydrite. Environmental Science & Technology 40:3248-3253.

Kosmulski, M. 2001. Chemical Properties of Material Surfaces Marcel Dekker, Inc., New York.

Kotz, R., H.J. Lewerenz, and S. Stucki. 1983. XPS studies of oxygen evolution on Ru and RuO_2 anodes. Journal of the Electrochemical Society 130:825-829.

Krauskopf, K.B., and D.K. Bird. 1995. Introduction to Geochemistry. 3rd ed. McGraw-Hill,Inc, New York, NY.

Lakshmipathiraj, P., B.R.V. Narasimhan, S. Prabhakar, and G.B. Raju. 2006. Adsorption studies of arsenic on Mn-substituted iron oxyhydroxide. Journal of Colloid and Interface Science 304:317-322.

Lee, Y., I.H. Um, and J. Yoon. 2003. Arsenic(III) oxidation by iron(VI) (ferrate) and subsequent removal of arsenic(V) by iron(III) coagulation. Environmental Science & Technology 37:5750-5756.

Lenoble, V., O. Bouras, V. Deluchat, B. Serpaud, and J.C. Bollinger. 2002. Arsenic adsorption onto pillared clays and iron oxides. Journal of Colloid and Interface Science 255:52-58.

Lister, T.E., Y. Chu, W. Cullen, H. You, R.M. Yonco, J.F. Mitchell, and Z. Nagy. 2002. Electrochemical and X-ray scattering study of well defined RuO2 single crystal surfaces. Journal of Electroanalytical Chemistry 524-525:201-218.

Manning, B.A., and S. Goldberg. 1996. Modeling competitive adsorption of arsenate with phosphate and molybdate on oxide minerals. Soil Science Society of America Journal 60:121-131.

Manning, B.A., S.E. Fendorf, and S. Goldberg. 1998. Surface structures and stability of As(III) on goethite: evidence for inner sphere complexes. Environmental Science and Technology 32:2383-2388.

Mayo, J.T., C. Yavuz, S. Yean, L. Cong, H. Shipley, W. Yu, J. Falkner, A. Kan, M. Tomson, and V.L. Colvin. 2007. The effect of nanocrystalline magnetite size on arsenic removal. Science and Technology of Advanced Materials 8:71-75.

McBride, M.B. 1994. Environmental Chemistry of Soils Oxford Press, New York.

McKenzie, K.J., and F. Marken. 2002. Electrochemical characterization of hydrous ruthenium oxide nanoparticle decorated boron-doped diamond electrodes. Electrochemical and Solid State Letters 5:E47-E50.

Meng, X.G., S. Bang, and G.P. Korfiatis. 2000. Effects of silicate, sulfate, and carbonate on arsenic removal by ferric chloride. Water Research 34:1255-1261.

Mohapatra, D., D. Mishra, G.R. Chaudhury, and R.P. Das. 2007. Arsenic(V) adsorption mechanism using kaolinite, montmorillonite and illite from aqueous medium. Journal of Environmental Science and Health Part a-Toxic/Hazardous Substances & Environmental Engineering 42:463-469.

Nordstrom, D.K. 2002. Public health - Worldwide occurrences of arsenic in ground water. Science 296:2143-2145.

O'Reilly, S.E., D.G. Strawn, and D.L. Sparks. 2001. Residence time effects on arsenate adsorption/desorption mechanisms on goethite. Soil Science Society of America Journal 65:67-77.

Over, H., Y.D. Kim, A.P. Seitsonen, S. Wendt, E. Lundgren, M. Schmid, P. Varga, A. Morgante, and G. Ertl. 2000. Atomic-scale structure and catalytic reactivity of the RuO2(110) surface. Science 287:1474-1476.

Rard, J.A. 1985. Chemistry and Thermodynamics of Ruthenium and Some of Its Inorganic-Compounds and Aqueous Species. Chemical Reviews 85:1-39.

Raven, K.P., A. Jain, and R.H. Loeppert. 1998. Arsenite and arsenate adsorption on ferrihydrite: Kinetics, equilibrium, and adsorption envelopes. Environmental Science & Technology 32:344-349.

Sadiq, M. 1997. Arsenic Chemistry in soils: an overview of thermodynamic predictions and field observations. Water, Air, and Soil Pollution 93:117-136.

Singh, A.K. 2006. Chemistry of arsenic in groundwater of Ganges-Brahmaputra river basin. Current Science 91:599-606.

Smedley, P.L., and D.G. Kinniburgh. 2002. A review of the source, behavior and distribution of arsenic in natural waters. Applied Geochemistry 17:517-568.

Smith, A.H., P.A. Lopipero, M.N. Bates, and C.M. Steinmaus. 2002. Public health - Arsenic epidemiology and drinking water standards. Science 296:2145-2146.

Sparks, D.L. 1999. Soil Physical Chemistry CRC Press, Boca Raton.

Sposito, G. 1989. The Chemistry of Soils Oxford University Press, New York.

Stollenwerk, K.G. 2003. Arsenic in Groundwater Kluwer Academic Publishers, Boston.

Stumm, W. 1992. Chemistry of the solid water interface John Wiley and Sons, New York.

Su, C.M., and R.W. Puls. 2001. Arsenate and arsenite removal by zero valent iron: Kinetics, redox transformation, and implications for in situ groundwater remediation Environmental Science & Technology 35:1487-1492.

Sun, X., and H.E. Doner. 1996. An investigation of arsenate and arsenite bonding structures on goethite by FTIR. Soil Science

161 12.

Swedlund, P.J., and J.G. Webster. 1999. Adsorption and polymerisation of silicic acid on ferrihydrite, and its effect on arsenic adsorption. Water Research 33:3413-3422.

Tournassat, C., L. Charlet, D. Bosbach, and A. Manceau. 2002. Arsenic(III) oxidation by birnessite and precipitation of manganese(II) arsenate. Environmental Science & Technology 36:493-500.

Waychunas, G.A., B.A. Rea, C.C. Fuller, and J.A. Davis. 1993. Surface-chemistry of ferrihydrite .1. EXAFS studies of the geometry of coprecipitated and adsorbed arsenate. Geochimica Et Cosmochimica Acta 57:2251-2269.

Welch, A.H., D.B. Westjohn, D.R. Helsel, and R.B. Wanty. 2000. Arsenic in ground water of the United States: Occurrence and geochemistry. Ground Water 38:589-604.

ARSENATE ADSORPTION ON RUTHENIUM OXIDES: A SPECTROSCOPIC AND KINETIC INVESTIGATION

ABSTRACT

Arsenate adsorption on amorphous (RuO_2•$1.1H_2O$) and crystalline (RuO_2) ruthenium oxides was evaluated using spectroscopic and kinetic methods to elucidate the adsorption mechanism. Extended x-ray absorption fine structure spectroscopy (EXAFS) was used to determine the local coordination environment of adsorbed arsenate. Pressure-jump relaxation spectroscopy was used to investigate the kinetics of arsenate adsorption/desorption on ruthenium oxides. Chemical relaxations resulting from the induced pressure change were monitored via electrical conductivity detection. EXAFS data were collected for two initial arsenate solution concentrations, 3 and 33 mM at pH 5. The collected spectra indicated a similar coordination environment for arsenate adsorbed to RuO_2•$1.1H_2O$ for both arsenate concentrations. In contrast the EXAFS spectra of RuO_2 indicated a difference in the local bonding environments for the crystalline material with increasing arsenate concentration. Data analysis indicated that both mono- and bidentate surfaces complexes were present on both RuO_2•$1.1H_2O$ and RuO_2. Relaxation spectra from the pressure-jump experiments of both ruthenium oxides resulted in a double relaxation event. A two step reaction mechanism for arsenate adsorption is proposed resulting in the formation of a bidentate surface complex. Analysis of the kinetic and spectroscopic data suggested that while there were two relaxation events, arsenate adsorbed to ruthenium oxide surfaces through both mono- and bidentate surface complexes.

INTRODUCTION

Arsenic most commonly occurs in soils and natural waters as a weakly acidic oxyanion in the form of arsenate (As(V); H_3AsO_4) in oxidized environments or arsenite (As(III); H_3AsO_3) under reducing conditions. However, research has demonstrated that arsenate may persist for extended periods of time in anoxic environments due to slow kinetics and biological transformations (Inskeep et al., 2002). Both arsenic species adsorb strongly to common soil and aquifer minerals (Sadiq, 1997). Furthermore, under oxidizing conditions sorption of arsenic by soil and aquifer colloids is the predominant means by which arsenic is sequestered (Sadiq, 1997; Singh, 2006; Smedley and Kinniburgh, 2002). The interaction of arsenic with metal (hydr)oxide surfaces is of critical importance in determining its mobility and bioavailability.

Nano and atomic scale investigations are important for understanding the physical and chemical basis for macroscopic measurements involving the potential toxicity of arsenic. At the same time, molecular and atomic scale data provide critical information for the development of physically realistic and accurate chemical models. Previous atomic scale research has demonstrated that arsenate specifically adsorbs to metal oxide surfaces forming an inner-sphere surface complex , while arsenite forms both outer- and inner-sphere complexes (Arai et al., 2001; Farquhar et al., 2002; Fendorf et al., 1997; Goldberg and Johnston, 2001; Manning et al., 1998; Manning et al., 2002; Sun and Doner, 1996; Tournassat et al., 2002; Waychunas et al., 1993). The speciation and stability of the adsorbed complex is a function of pH, surface concentration, and (hydr)oxide crystal structure (Arai et al., 2001; Farquhar et al., 2002; Fendorf et al., 1997;

Foster et al., 2003; Goldberg and Johnston, 2001; Manceau, 1995; Sherman and Randall, 2003; Sun and Doner, 1996; Waychunas et al., 1995; Waychunas et al., 1993).

In addition to determining the speciation and the stability of adsorbed arsenic, the ability of oxide surfaces to catalyze the oxidation of arsenite (As(III)) to arsenate (As(V)) is of interest due to the increased mobility and toxicity of arsenite (Frankenberger, 2002). Extensive research has demonstrated the ability of manganese oxides to oxidize arsenite to arsenate (Foster et al., 2003; Fuller et al., 1993; Oscarson et al., 1980; Oscarson et al., 1981; Tournassat et al., 2002). Recently, Impellitteri et al. (Impellitteri et al., 2003) evaluated arsenite oxidation on hydrous ruthenium oxide ($RuO_2 \cdot xH_2O$). The authors demonstrated the rapid and complete oxidation of arsenite (As(III) to arsenate (As(V)) during adsorption. Furthermore, the oxidized arsenate was sequestered by the ruthenium hydroxide. In the previous chapter the macroscopic adsorption behavior of arsenate was examined on amorphous and crystalline ruthenium oxides and results demonstrated the large adsorption capacity of the ruthenium oxides over a wide range in pH, and arsenate concentrations. In the current study we evaluate the arsenate adsorption mechanism on ruthenium oxides. The specific objectives are to: (1) determine the local coordination environment of arsenate adsorbed to $RuO_2 \cdot 1.1H_2O$ and RuO_2 using EXAFS, (2) evaluate the adsorption/desorption kinetics of arsenate on $RuO_2 \cdot 1.1H_2O$ and RuO_2 using pressure-jump relaxation spectroscopy, and (3) develop a plausible adsorption mechanism for arsenate adsorbed to $RuO_2 \cdot 1.1H_2O$ and RuO_2 based on the spectroscopic and kinetic data presented.

MATERIAL AND METHODS

Ruthenium Oxide Characterization

Crystalline (RuO_2) and amorphous ($RuO_2 \cdot 1.1H_2O$) ruthenium oxide used in the current study were obtained from a Ruthenium(IV) oxide hydrate Premion® (99.99% pure metal basis) from Alfa Aesar (Ward Hill, MA). The ruthenium oxide hydrate was purged under positive pressure N_2 gas for 5 days to remove sorbed argon from the packaging process. Thermogravimetric and calorimetric analysis (DuPont Instruments DSC 2910 and Hi-Res TGA 2950, New Castle, DE) of the solid phase were used to determine the quantity of structural water associated with the amorphous phase and the temperature at which conversion from the amorphous material to crystalline material occurred. Results from the thermal analysis indicated 1.1 moles of water per mole of material yielding the chemical formula $RuO_2 \cdot 1.1\ H_2O$ for the amorphous material. Thermal analysis also indicated that $RuO_2 \cdot 1.1H_2O$ underwent a phase transformation to crystalline ruthenium oxide (RuO_2) at approximately 300^o C. After purging $RuO_2 \cdot 1.1H_2O$ was used in the adsorption studies without any further treatments. The crystalline material was prepared by heating the $RuO_2 \cdot 1.10H_2O$ to 500^o C for 24 hours in a muffle furnace. X-ray diffraction (Scintag® XDS 2000 X-ray Diffraction Spectrophotometer, Scintag Inc., Sunnyvale, CA) and differential scanning calorimetry data indicated a full conversion of the amorphous material to crystalline RuO_2 with a rutile crystal structure. Specific surface area (SSA) of the samples was determined by a five point Brunauer-Emmet-Teller (BET) sorption isotherm using a Micromoretics ASAP2010 Surface Area Analyzer (Norcross, GA). The measured SSA for both oxides was 100 and 50 $m^2\ g^{-1}$ for the $RuO_2 \cdot 1.1H_2O$ and RuO_2, respectively. Nitrogen adsorption isotherms indicated 15 $m^2\ g^{-1}$ of micro-porous surface area for the amorphous material and less than 1 $m^2\ g^{-1}$ for the crystalline Ru-oxide. The point of zero charge (PZC) was determined by micro-electrophoresis measurements using a Malvern 3000HSa (Malvern Instruments, Southborogh, MA). For the two solids the PZC was 4.2±0.1 and 5.6±0.1

for RuO_2•1.1H_2O and RuO_2, respectively. The quantity of titratable functional groups was 50 and 20 μmol m^{-2} for the amorphous and crystalline ruthenium oxides, respectively. Titratable functional groups were determined by proton titrations conducted at 0.05, 0.01, and 0.10 M NaCl.

Batch Adsorption Experiments

Samples analyzed by EXAFS or p-jump were prepared from arsenate adsorption isotherms on RuO_2•1.1H_2O and RuO_2. Adsorption isotherms for EXAFS samples were conducted at pH 5 in a 2 g L^{-1} suspension, while p-jump adsorption isotherms were conducted at pH 4, 5, and 6 in a 0.1 and 0.5 g/L^{-1} suspension for RuO_2•1.1H_2O and RuO_2, respectively. Different suspension densities were used to achieve optimal results from the EXAFS and p-jump experiments. Chemical relaxation techniques require a stable suspension for proper data collection and analysis, while EXAFS analysis requires solid concentrations large enough to produce prominent backscattering frequencies. The range of arsenate concentrations investigated was 0.167 to 33 mM (12.5 to 2500 mg L^{-1}) and 0.013 to 0.667 mM (1 to 50 mg L^{-1}) for EXAFS and p-jump analysis, respectively. Briefly, experiments were conducted in duplicate at a constant ionic strength (0.01 M NaCl) using a pH-monitored stirred-batch reactor. An appropriate quantity of N_2 sparged ruthenium oxide was weighed into a 500 mL glass beaker to which 350 mL of 0.01 M NaCl was added. The suspension was dispersed for ~2 min using an ultrasonic dimembrator. The beaker was placed in a water jacketed reaction vessel kept at 25^o C, stirred using a Teflon coated magnetic stir bar, and kept under positive pressure with N_2 gas to eliminate CO_2. The suspension was allowed to hydrate for a period of 24 h while the pH was adjusted to the appropriate value using a Brinkman® 716 Stat-Trino pH stat (Brinkman Instruments, Westbury, NY) (with either 0.1 M HCl or NaOH). After the hydration period an appropriate quantity of a pH adjusted 100 mM arsenate stock solution (made from a reagent grade sodium arsenate salt) was added to the reactor to achieve the desired arsenate concentration. The total volume was brought to 400 mL and a pH stat was used to maintain the appropriate pH. After three hours two 10 mL samples were removed. The first sample was filtered through a 0.05 μm Millipore nitrocellulose filter (Billerica, MA) for solution analysis. The second sample was used for either pressure-jump or EXAFS analysis. Filtrate collected from the adsorption isotherms was analyzed by inductively coupled plasma atomic emission spectroscopy (ICP-AES) (SpectroFlame FTMOA85D, Spectro Analytical Instruments, Fitchburg, MA). The detection limit on the SpectroFlame ICP-AES for As and Ru was 10 and 12 μg L^{-1}, respectively. The quantity of oxyanion adsorbed was determined by subtracting the initial oxyanion concentration from the measured concentration.

Extended X-ray Absorption Fine Structure Spectroscopy

Samples analyzed by extended x-ray absorption fine structure spectroscopy (EXAFS) were filtered through a 0.05 μm Millipore filter and washed three times with 10 mL of pH adjusted 0.01 M NaCl to remove any entrained arsenate not associated with the surface. The resulting paste was stored moist in between two filter papers in a sealed plastic dime bag (3.8 x 5 cm) at 5 ^{o} C until analysis. No more than 12 h prior to analysis the samples were transferred to a 0.25 mm thick polycarbonate sample holder affixed with Kapton® tape on both sides to hold the sample in place and prevent drying. Arsenic K-edge spectra (11, 867 eV) were collected at beamline 10-ID (Materials Research Collaborative Access Team) and 20-BM (Pacific Northwest Consortium Collaborative Access Team) at the Advanced Photon Source at Argonne National

Laboratory, Argonne, IL. EXAFS spectra were collected in fluorescence mode using an Ar filled Lytle detector with a 3 μm thick Z-1 filter to reduce unwanted x-ray fluorescence. The electron storage ring operated at 7 GeV. The light source was equipped with a Si 111 monochromator with the horizontal slit set at 6 mm and the vertical at 2.3 mm. Scans were collected from 11,699 to 12, 867 eV.

The collected spectra were analyzed using the Athena and Artemis software programs in the computer package IFEFFIT (Ravel and Newville, 2005). At least three individual spectra were averaged followed by subtraction of the background through the pre-edge region using the Autobk algorithm (Newville et al., 1993). The averaged spectra were normalized to an atomic absorption of one, and the EXAFS signal was extracted from the spectra. The data was converted from energy to photoelectron momentum (**k**-space) and weighted by $\mathbf{k}^3$. EXAFS spectra were calculated over a typical **k**-space range with a Hanning window and 1.0 width Gaussian wings. Fourier transforms (FT) were performed to obtain the radial distribution function (RDS) in **R**-space. Plotted **R**-space (Å) data are not phase shift corrected, the true distances are between 0.3 and 0.5 Å longer than the distances shown. The spectra were fit with the FEFF8 computer code which uses ab initio calculations to determine phase shift and amplitude functions for single and multiple atomic scattering paths. Each spectrum was fit by isolating the first shell (As-O) to estimate the change in the threshold energy between theory and experiment (ΔE_o). The value of ΔE_o was determined using an atomic cluster of Arsenic pentoxide (As_2O_5). Only tetraherally coordinated As-O paths were used. The number of scattering atoms was set to four, the amplitude reduction factor (S_{O2}) was constrained to be with in the range of 0.95 to 1.05, and the Dybe-Waller factor (σ^2) was set to 0.5. For the remaining fits ΔE_o was set to the best first shell fit (7.29 ± 1.7 eV and 2.24 ± 1.28 eV for the amorphous and crystalline materials, respectively). The scattering paths used to fit the EXAFS data were selected based on potential surface complexes determined by geometrically estimating potential scattering paths using a theoretical crystal structure of RuO_2 and the computer program Crystal Maker® (Crystal Maker Software Ltd., Cambridge, England, 2004). The atomic distances for As-O and As-Ru in mono-and bidentate surface complexes were calculated using known As-O and Ru bond distances, and hypothetical arsenate surface complexes. Surface complexes that resulted in O-As-O tetrahedral angles in excess of 120° were not considered. Spectra were fit with single scattering theoretical phase shift and amplitude functions calculated with FEFF8. The scattering paths were generated from two atomic clusters As_2O_5 and a RuO_2 rutile structure. The arsenic pentaoxide was used to generate scattering paths for the first shell. The second shell of arsenic was fit with a 10% As substituted RuO_2 rutile structure. The ΔE_o was fixed for both atomic clusters. The first shell fitting was done in R-space and the second shell fitting in q-space. The final fitting of the spectra was done on Fourier Transformed $\mathbf{k}^1$, $\mathbf{k}^2$, and $\mathbf{k}^3$ weighted spectra in R-space. The scattering path distance of As-O and As-Ru were initially fixed to the calculated nearest neighbor distances (R) to determined estimates of $S_{(O2)}$ and σ^2. Finally the spectra were simultaneously fit using the estimated parameters, to achieve a best fit.

Pressure-Jump Relaxation Spectroscopy

The pressure-jump relaxation spectrometer (p-jump) used in the current study was manufactured by DIA-LOG Co. (Düsseldor, Germany) and is similar in design to the model described in detail by Sparks et al.(Sparks et al., 1996). The p-jump apparatus is comprised of two parts: 1) a system for pressure induction consisting of a pressure autoclave, sample and

reference electrodes; and 2) a system for conductivity detection that includes a wheatstone bridge, oscilloscope, digitizer, and DIA-LOG computer software for data collection.

Briefly a typical p-jump involves filling the sample cells (~1 mL) with the mineral plus adsorbate suspension and the reference cell with the suspension filtrate or supernatant. Sample cells are covered with a thin Teflon membrane, tightly sealed, and inserted in the pressure autoclave. The Teflon membrane covering each cell becomes part of the inner wall of the autoclave. The pressure chamber was sealed with a thin strip of brass foil (~80 μm thick) specifically milled to rupture at 13.5 MPa (133 atm). The sample cells were connected to two arms of a wheatstone bridge through BNC cables. The other two arms were attached to variable resistors and capacitors. The variable resistors and capacitors were used to balance the resistance between the reference and sample. After balancing the cell the pressure within the chamber was increased by forcing water into the chamber with a mechanical hand pump. The pressure within the chamber is transferred to the sample and reference cells through the Teflon membrane. As the pressure increases the chemical equilibrium in the sample cell shifts and the wheatstone bridge becomes unbalanced. At 13.5 MPa the brass foil ruptures triggering a piezoelectric capacitor which captures changes in conductivity as the system immediately relaxes (60 μsec) to ambient conditions. Data obtained from changes in conductivity as the system relaxes were digitized to create a relaxation curve and displayed on a computer screen. The DIA-LOG software enabled for the co-addition of multiple relaxations to reduce signal to noise ratios and improve data reliability. For each sample between 40 and 50 relaxation curves were averaged prior to data analysis. The averaged relaxation curves were analyzed using the computer program ORIGIN 5.0 (Microcal^{TM}, Nothhampton, MA, 1998). The program was used to determine the value of τ, the time it takes for the relaxation to reach $1/e$ of the initial relative amplitude, for each relaxation (Bernasconi, 1976).

RESULTS AND DISCUSSION

Extended X-Ray Absorption Spectroscopy Analysis

Extended x-ray absorption fine structure spectroscopy was used to determine the local coordination of arsenate adsorbed to Ru-oxides. Analysis of the local coordination environment provided information on the arsenate bonding mechanism and surface speciation. Spectra were collected for both solids at a pH value of 5 and two arsenic surface concentrations (3.3 and 33 mM). The arsenate surface concentrations correspond to As:Ru mole ratios of 0.1 and 1.0. These same data points are indicated by arrows in Figure 4-1. Visual inspection of the $\chi(k)\mathbf{k}^3$ data and the corresponding radial distribution functions indicate a similar local coordination environments for arsenate adsorbed to $RuO_2 \cdot 1.1H_2O$ at both arsenate concentrations (Figure 4-2). Additionally, the 3 mM data for the RuO_2 is very similar to the amorphous material suggesting a similar bonding environment. The 33 mM arsenate adsorbed to RuO_2 differs from the other spectra suggesting a change in the arsenate coordination environment and bonding geometry. The similarities between $RuO_2 \cdot 1.1H_2O$ and RuO_2 Ru-oxide EXAFS spectra for the 3 mM arsenate probably results from the low surface coverage of arsenate (Figure 4-1). Differences in the EXAFS spectra for the 33 mM arsenate are most likely related to changes in the Ru-oxide structure.

The similarity in the bonding environments between the two arsenate concentrations for $RuO_2 \cdot 1.1H_2O$ highlight the large quantity of reactive functional groups and the structural

disorder of the material compared to the crystalline oxide (Figure 4-2). The structure or atomic arrangement associated with amorphous ruthenium oxides was determined by McKeown et al. (McKeown et al., 1999) using Ru k-edge EXAFS data. The results indicate that hydrous ruthenium oxides, with a structural molar water content near 1.5 (RuO_2•$1.5H_2O$), are comprised of twisting unconnected edge linked Ru octahedron chains linked through two equatorial oxygen ligands. Analysis of the structure reveals that all of the six coordinating oxygen ligands have at least one available bonding orbital for participation in protonation and ligand exchange reactions. The existence of potentially six chemically reactive functional groups per Ru atom reveals the origin of the large quantity of functional groups and the homogeneity of bonding environments for arsenate at both surface concentrations.

The EXAFS data analysis revealed minimal changes in As-O bond length for arsenate sorbed to either Ru-oxide as compared to As-O bond lengths in aqueous arsenate (H_3AsO_4) and scorodite ($FeAsO_4$•H_2O) (Table 4-1). The minimal variation in As-O bond distance regardless of the immediate molecular environment (solution, adsorbate, bulk crystal) have been reported for arsenate and is attributed to the strength of the As-O bond (Arai et al., 2001; Beaulieu and Savage, 2005; Fendorf et al., 1997; Manning et al., 2002; Sherman and Randall, 2003; Waychunas et al., 1993).

EXAFS data analysis of the amorphous Ru-oxide FT spectra beyond the first shell of oxygen resulted from backscattering induced by a Ru atom at 3.38±0.02 Å (Figure 4-3). The coordination number (CN) determined from the data fit was 2.1±0.36 (Table 4-1) suggesting the formation of an inner-sphere bidentate surface complex. Scattering distances calculated for possible arsenate surface complexes using an ideal (110) and (101) Ru-oxide terminal crystal planes indicated that As-Ru scattering distances for potential bidentate surface complexes were 2.06, 3.11, and 3.38 Å for arsenate bound to either equatorial, axial, or bridging equatorial oxygen atoms, respectively (Figure 4-3). The terms equatorial and axial refer to the position of the oxygen ligands in the Ru octahedron (Figure 4-4). In addition to the bidentate complex, a monodentate complex bound to a shared equatorial oxygen atom was identified with two As-Ru scattering distances of 3.35 Å (Figure 4-4). Quantum mechanical modeling of arsenate adsorption on iron oxides predicts bidentate surface complexes to be the most energetically favorable surface complex, and the same relationship is expected for Ru-oxides suggesting the identified As-Ru back scattering is related to a bidentate surface complex (Sherman and Randall, 2003). For the 33 mM arsenate the surface normalized concentration is 31 μmol m^{-2}, for RuO_2•$1.1H_2O$. Assuming only a bidentate surface complex, the quantity of arsenate adsorbed exceeds the number of titratable functional groups identified during oxide characterization (50 μmol m^{-2}). Therefore the possibility of both mono- and bidentate types of surface complexes at higher arsenate loading cannot be ruled out.

As previously discussed RuO_2 3 mM arsenate $\mathbf{k}^3$ data and the subsequent FT displayed a strong resemblance to RuO_2•$1.1H_2O$. EXAFS data analysis of RuO_2 indicated a similar CN, scattering distances, and Debye-Waller factors (σ^2) compared to RuO_2•$1.1H_2O$ (Table 4-1). The bridging bidentate complex proposed for RuO_2•$1.10H_2O$ was not considered for RuO_2 since the bridging complex could only occur between octahedral chains (McKeown et al., 1999). Neither of the two predominant terminal crystal planes (110 and 101) for RuO_2 contain Ru octahedron arrangements suitable for the formation of a bidentate bridging surface complex (Huang and Chen, 2001; Ji et al., 2001; Lister et al., 2002). Without the presence of a suitable Ru octahedral arrangement the As-Ru back scattering at 3.38 Å for RuO_2 is attributed only to the formation of a monodentate binuclear arsenate surface complex (Figure 4-4).

Three As-Ru scattering distances were identified for the 33 mM arsenate adsorbed to RuO_2. The scattering distances occurred at 2.06, 3.21, and 3.71 Å, indicating the presence of possibly three different types of surface complexes (Table 4-1 and Figure 4-3 and 4-4). The scattering distances determined in the EXAFS analysis were compared with distances calculated for several arsenate adsorption complexes using the ideal RuO_2 crystal planes discussed previously. The scattering distances identified in the FT $\mathbf{k}^3$ data correspond to three potential surface complexes: equatorial bidentate (2.06 Å, Ru1), axial bidentate (3.21 Å, Ru2), and axial monodentate (3.71 Å, Ru3) (Ru1-3 refer to the identified peaks in Figure 4-3 and Table 4-1). The equatorial bidentate complex was not originally included in the fit due to the short distance between As and Ru. However, attempts to fit the EXAFS data with either O or As were unsuccessful, or resulted in error terms exceeding those predicted for the equatorial bidentate complex. The presence of the equatorial monodentate complex associated with the 3 mm arsenate was not present (absence of a 3.38 Å peak). The reason for the change in the surface speciation of arsenate with increasing arsenate is not clear. The surface normalized arsenate concentration for 33 mM arsenate is 34.7 μmol m^{-2}, well in excess of the 20 μmol m^{-2} of titratable functional groups. The magnitude of the arsenate surface concentration suggests either the formation of a secondary phase, diffusion of arsenate into the crystal structure, or the presence of residual amorphous material not converted during the heat treatment. X-ray diffraction and differential scanning calorimetry data for RuO_2 did not indicate the presence of an amorphous phase, nor did N_2 gas adsorption isotherms indicate any substantial hysteresis, a characteristic property of materials containing meso- or micro-pores (Rouquerol et al., 1999). The formation of a secondary phase appears to be the most likely explanation for the elevated arsenate surface concentration. While Ru-oxides are extremely insoluble, several researchers have proposed that saturation of Fe and Al oxide surfaces by oxyanions results in the liberation of Fe and Al from the solid phase (Stumm, 1992). If the same process occurred for arsenate adsorption on RuO_2 the liberated Ru could be incorporated into a secondary precipitate, increasing the total adsorption capacity of the material. Additionally, in the previous chapter a soluble fraction of the Ru-oxide was identified during arsenate desorption by hydroxyls indicating a potential source for Ru. A ruthenium substituted scorodite structure was used to model the EXAFS data, but the overall fit, and error terms greatly exceed those of the oxide structure. The axial monodentate complex (Ru3 Table 4-1 and Figure 4-3) might be associated with arsenate bound to liberated Ru as it represents a bonding geometry similar to other metal arsenate. Further investigation of the system employing the use of Ru K-edge EXAFS data could lead to clarification of the potential mechanism involved in arsenate adsorption at elevated concentrations.

Pressure-Jump Relaxation Spectroscopy

Pressure jump relaxation (p-jump) studies were conducted to: 1) determine the arsenate adsorption/ desorption rates, 2) calculate equilibrium constants associated with arsenate adsorption on Ru-oxides and 3) further elucidate the mechanism of arsenate adsorption on Ru-oxides. Pressure-jump experiments were evaluated at pH values of 4, 5, and 6 and pH 4 and 6 for arsenate adsorption isotherms on $RuO_2 \bullet 1.1H_2O$ and RuO_2. The suspension densities of the two oxides were 0.2 and 0.5 g L^{-1} for the $RuO_2 \bullet 1.1H_2O$ and RuO_2, respectively. The suspension densities of the two oxides were varied to achieve an equal number of titratable functional groups for both oxide surfaces (0.25 mmol L^{-1}). The initial arsenate solution concentration was

varied from 0.0167 to 0.66 mM arsenate (1 to 50 mg L^{-1}).The pH range and initial solution concentrations were chosen to associate relaxation signals with adsorption and desorption reactions. A double relaxation event was observed for arsenate adsorption on both Ru-oxides over the entire concentration and pH range investigated (Figure 4-5). The double relaxation is associated with a fast relaxation (τ_1) followed by a slow relaxation (τ_2) (Bernasconi, 1976). For both Ru-oxides there was an increase in the value of τ_1 with increasing arsenate concentration, while the value of τ_2 remained fairly constant (Figure 4-5). A similar trend of increasing τ_1 with increasing chromate concentration was noted by Grossl et al. (Grossl et al., 1997) who investigated chromate and arsenate adsorption/desorption on goethite. The value of RuO_2 τ_1^{-1} and τ_2^{-1} exceeded those of $RuO_2 \bullet 1.1H_2O$ indicating an increase in the rate of arsenate adsorption/desorption.

Grossl et al. (Grossl et al., 1997) proposed that the double relaxation event was a two step process resulting in the formation of a bidentate inner-sphere surface complex. They attributed the first relaxation (τ_1) to the initial ligand exchange reaction followed by a slower relaxation (τ_2) associated with the second ligand exchange reaction resulting in the bidentate complex. The validity of the proposed reaction mechanism can be determined using a theoretical reaction scheme involving a two elementary reaction steps (Bernasconi, 1976).

$$A + B \underset{k_{-1}}{\overset{k_1}{\rightleftharpoons}} C \underset{k_{-2}}{\overset{k_2}{\rightleftharpoons}} D \qquad (4\text{-}1)$$

In Eq. 4-1 the fast τ is associated with k_1 and k_{-1} and the slow τ is associated with k_2 and k_{-2}. For the current study Equation 4-1 can be rewritten as:

$$2RuO + H_2AsO_4^- \underset{k_{-1}}{\overset{k_1}{\rightleftharpoons}} (RuO)RuOAsO_2(OH)^- + OH^- \underset{k_{-2}}{\overset{k_2}{\rightleftharpoons}} (2RuO)AsO_2^{-2} + OH^- \qquad (4\text{-}2)$$

Linearized rate equations, developed for Equation 4-1 relating the τ^{-1} relaxation values to reactant concentration, were used to test the validity of the proposed mechanism. The two linearized rate equations were (Bernasconi, 1976):

$$\tau_1^{-1} + \tau_2^{-1} = k_1([RuO]+[H_2AsO_4^-])+k_{-1} + k_2 + k_{-2} \qquad (4\text{-}3)$$

$$\tau_1^{-1} * \tau_2^{-1} = k_1(k_2 + k_{-2}) * ([RuO]+[H_2AsO_4^-])+k_{-1} * k_{-2} \qquad (4\text{-}4)$$

In Equation 4-3 and4-4, [ ] refer to molar concentrations. A plot of the reactant concentration as a function of $\tau_1+\tau_2$ and $\tau_1*\tau_2$ should yield a straight line if the proposed mechanism is plausible (Bernasconi, 1976). Plots of equations 4-3 and 4-4 yielded straight lines suggesting that the proposed mechanism was plausible (Figure 4-6 and 4-7). The forward and reverse rate constants for both reaction steps (monodentate, bidentate) were obtained from the slope and y-intercept of the linear regression line for each solid in Figures 4-6 and 4-7. The slope of the lines were equal to k_1 and $k_1*(k_2+k_{-2})$ and the y-intercepts were equal to $k_{-1}+k_2+k_{-2}$ and $k_{-1}*k_{-2}$ for Figure 4-6 and 4-7, respectively. Equilibrium constants for each elementary reaction were calculated from the fundamental relationship between kinetics and thermodynamics (Sparks et al., 1996) (Eq. 4- 5)

$$K_{eq} = \frac{k_1}{k_{-1}} \qquad (4\text{-}5)$$

The overall equilibrium constant for the formation of a bidentate surface complex (K_{As}) was calculated using an equation presented by Liu and Huang (Liu and Huang, 2001)

$$K_{As} = \frac{K_1 * k_2}{k_{-2}} \qquad (4\text{-}6)$$

Results from the linear regression of the rate data indicated that the initial uptake (k_1) of arsenate by RuO_2•$1.1H_2O$ exceed the rate of RuO_2 while the reverse was true for the desorption step (k_{-1}) (Table 4-2). Additionally, the overall magnitude of the equilibrium constant increased for the RuO_2. The increased rate of arsenate adsorption on RuO_2•$1.1H_2O$ is not surprising due to the increased surface roughness or heterogeneity (analogous to increased chemical reactivity) compared to RuO_2 (Hochella, 1990). The same is true for the reduced desorption rate constant for RuO_2•$1.1H_2O$ where steric factors would contribute to a reduced rate of desorption. Surface complexation modeling of arsenate adsorption on ferrihydrite and goethite has also indicated an increased stability of arsenate adsorbed to crystalline materials leading to an increase in the magnitude of the equilibrium constant (Dixit and Hering, 2003).

The second step of the reaction for RuO_2•$1.1H_2O$ indicates the rate of the desorption reaction (k_{-2}) exceeds the adsorption rate (k_2) (Table 4-2). This leads to a negative log K value and indicates that a monodentate complex may be slightly preferred over a bidentate complex (Grossl et al., 1997). The similarity in the forward and reverse rate constants for the second step of RuO_2 indicates the possible presence of both mono-and bidentate surface complexes (Table 4-2).

Proposed Arsenate adsorption Mechanism

The range of arsenate solution concentrations investigated in the p-jump experiments encompasses surface concentrations representative of the 3 mM EXAFS experiments. Elevated concentrations were not investigated due to the possible presence of a secondary arsenate phase, and the difficulty in interpreting relaxation spectra that encompassed three or more relaxations (Bernasconi, 1976). Kinetic data from the pressure-jump relaxation experiments indicated arsenate forms both mono- and bidentate inner-sphere surface complexion on RuO_2•$1.1H_2O$ and RuO_2. This is in excellent agreement with the EXAFS results for the 3 mM arsenate concentration.

Analysis of the EXAFS data collected for the RuO_2•$1.1H_2O$ indicated two potential arsenate surface complexes, a binuclear bridging bidentate complex and a binuclear equatorial monodentate complex. Data collected from the p-jump experiments support this conclusion. Furthermore, the kinetic data obtained from the p-jump experiments indicates the monodentate complex may be preferred. RuO_2 a single monodentate surface complex was identified during the EXAFS data analysis, a binuclear equatorial monodentate complex. In contrast, the p-jump data suggest that both mono- and bidentate surface complexes may be present. The discrepancy between the two studies could be related to several possibilities including a failure to identify a second surface complex in the EXAFS data, a low proportion of bidentate surface complexes, or the presence of terminal crystal plains not considered in the theoretical calculations. EXAFS data from the 33 mM concentration did indicate the presence of a bidentate surface complex. Therefore, it is not unreasonable to expect that bidentate complexes may be present at lower arsenate surface concentrations as the p-jump data suggests.

Based on the results from the spectroscopic and kinetic studies, two arsenate adsorption mechanisms are proposed. The first mechanism is comprised of a single step where arsenate undergoes a ligand exchange mechanism with a Ru-oxide hydroxyl group resulting in the formation of a monodentate inner-sphere complex (Equation 4-7 and Figure 4-8).

$$RuO^- + H_2AsO_4^- \underset{k_{-1}}{\overset{k_1}{\rightleftharpoons}} RuOAsO_2(OH)^- + OH^- \qquad (4\text{-}7)$$

The second mechanism is comprised of a two step reaction where arsenate first undergoes a ligand exchange reaction with a surface hydroxyl group to form a monodentate complex, followed by a second ligand exchange reaction resulting in the formation of a bidentate inner-sphere complex (Equation 4-7 and Figure 4-8).

$$2RuO + H_2AsO_4^- \underset{k_{-1}}{\overset{k_1}{\rightleftharpoons}} (RuO)RuOAsO_2(OH)^- + OH^- \underset{k_{-2}}{\overset{k_2}{\rightleftharpoons}} (2RuO)AsO_2^- + OH^- \quad (4\text{-}8)$$

The proposed mechanisms are appropriate only when arsenate surface concentrations are less than 20 and 50 μmol m^{-2} for $RuO_2 \cdot 1.10H_2O$ and RuO_2, respectively.

For the elevated arsenate surface concentrations, the two proposed reaction mechanisms provide a plausible adsorption mechanism for arsenate adsorbed to $RuO_2 \cdot 1.1H_2O$, but fail to explain adsorption data for RuO_2 where arsenate surface concentrations (34 μmol m^{-2}) exceed the quantity of reactive functional groups. Any plausible adsorption mechanism would need to incorporate a means by which the excess arsenate is retained by the Ru-oxide surface. Further evaluation of the local Ru coordination environment or positive identification of a secondary phase may provide the additional information required.

TABLES

Table 4-1 Structural parameters developed from EXAFS analysis of arsenate adsorption on RuO_2•1.1H_2O and RuO_2.

Material	Shell	CN		R		s2		3rd[§]	
RuO_2•1.1H_2O	As-O	4.00	0.05	1.70	0.005	0.002	0.0002		
	As-Ru	2.10	0.10	3.38	0.02	0.008	0.001	0.0007	0.0002
RuO_2 (0.1)	As-O	4.00	0.05	1.68	0.005	0.002	0.0002		
	As-Ru	1.84	0.12	3.38	0.04	0.008	0.002	0.0008	0.0002
RuO_2 (1.0)	As-O	4.00	0.20	1.68	0.016	0.002	0.0002		
	As-Ru1	0.96	0.24	2.06	0.0117	0.005	0.001	0.0003	0.00012
	As-Ru2	1.71	0.10	3.21	0.02	0.008	0.002		
	As-Ru3	0.54	0.40	3.70	0.0225	0.005	0.002		
Scordite[†]	As-O	4		1.70		0.004			
	As-Fe	2		3.31		0.007			
	As-Fe	2		3.41		0.007			
H_3AsO_4[‡]	As-O	4		1.69		0.004			

§Third Cumulate for Ru

†Sherman and Randall (Sherman and Randall, 2003)

‡Arai et al. (Arai et al., 2001)

Table 4-2 Calculated rate constants and subsequent equilibrium constants for arsenate adsorption on RuO_2•1.1H_2O and RuO_2. K_1 and K_2 refer to the equilibrium constant calculated from the forward and reverse rate constants for each reaction step. K_{As} refers to the overall equilibrium constant for the formation of a bidentate arsenate surface complex.

	Amorphous	Crystalline
k_1 (L mol^{-1} sec^{-1})	$10^{5.73}$	$10^{5.30}$
k_{-1} (sec^{-1})	$10^{1.86}$	$10^{2.02}$
Log K_1	3.87	3.28
k_2 (L mol^{-1} sec^{-1})	$10^{0.49}$	$10^{0.77}$
k_{-2} (sec^{-1})	$10^{1.15}$	$10^{0.61}$
Log K_2	-0.66	0.16
Log K_{As}	3.21	3.44

FIGURES

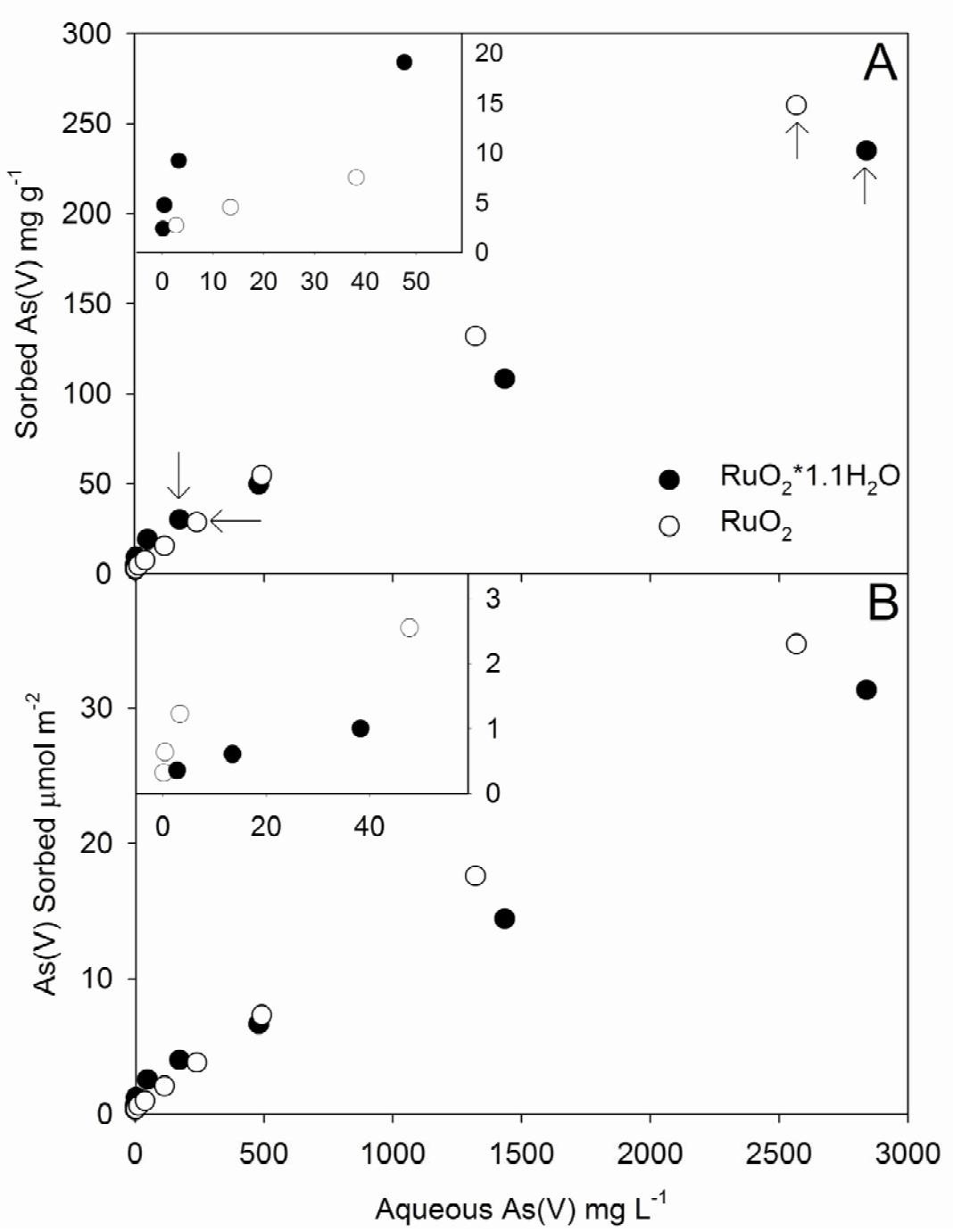

Figure 4-1 Arsenate adsorption isotherm for the pH 5 2 g L^{-1} suspension density. (A) Arsenate adsorption on a mass basis and (B) Arsenate adsorption normalized for surface area. Inset shows lower solution concentration data, same axes. Arrows indicate samples analyzed by EXAFS.

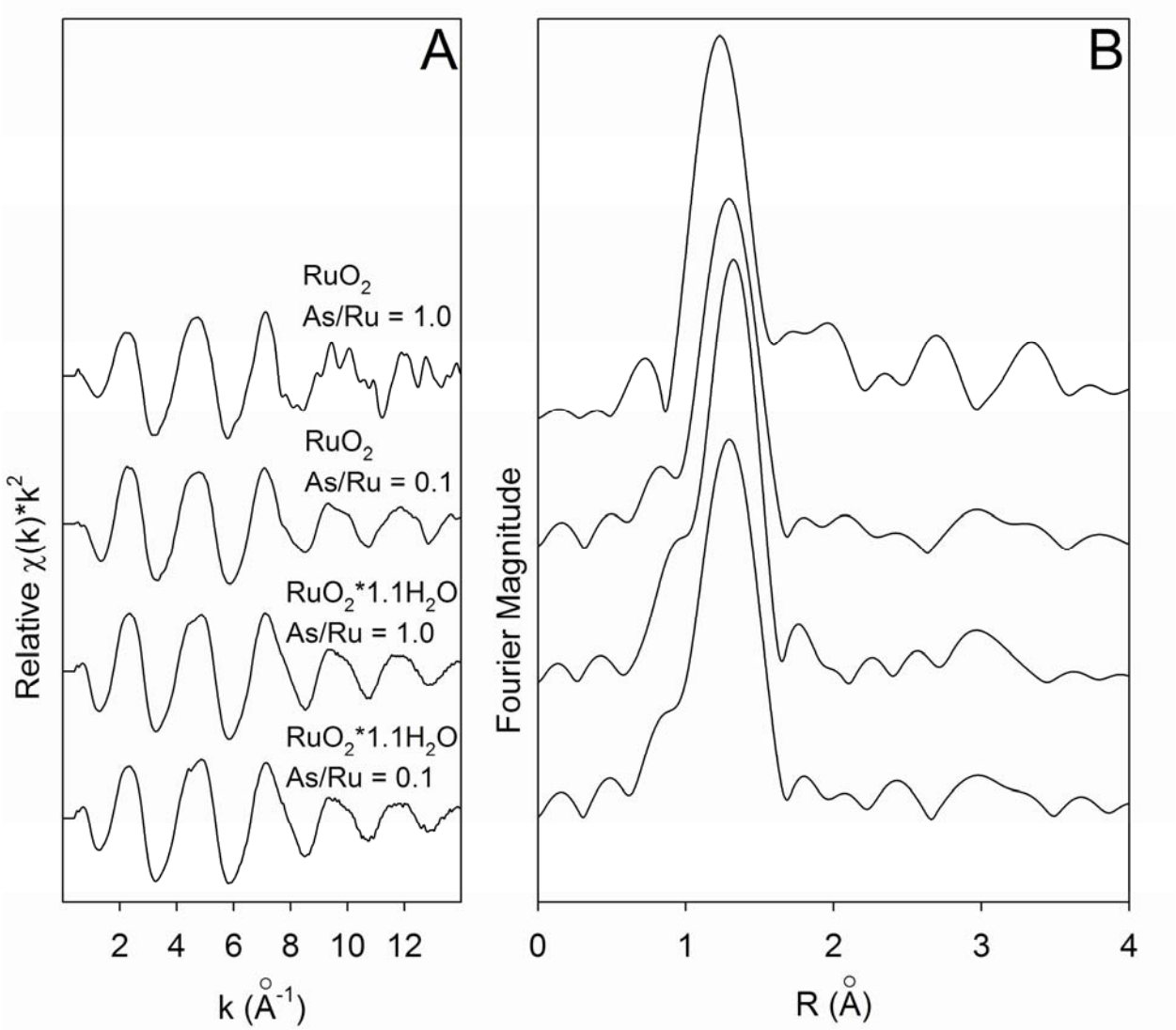

Figure 4-2 (A) Experimental As K-edge data. (B) Radial distribution functions obtained from the Fourier transform of the EXAFS data. Peaks represent atomic distances (uncorrected for phase shifts) between As and nearby atoms. Data are displayed in the same order as A.

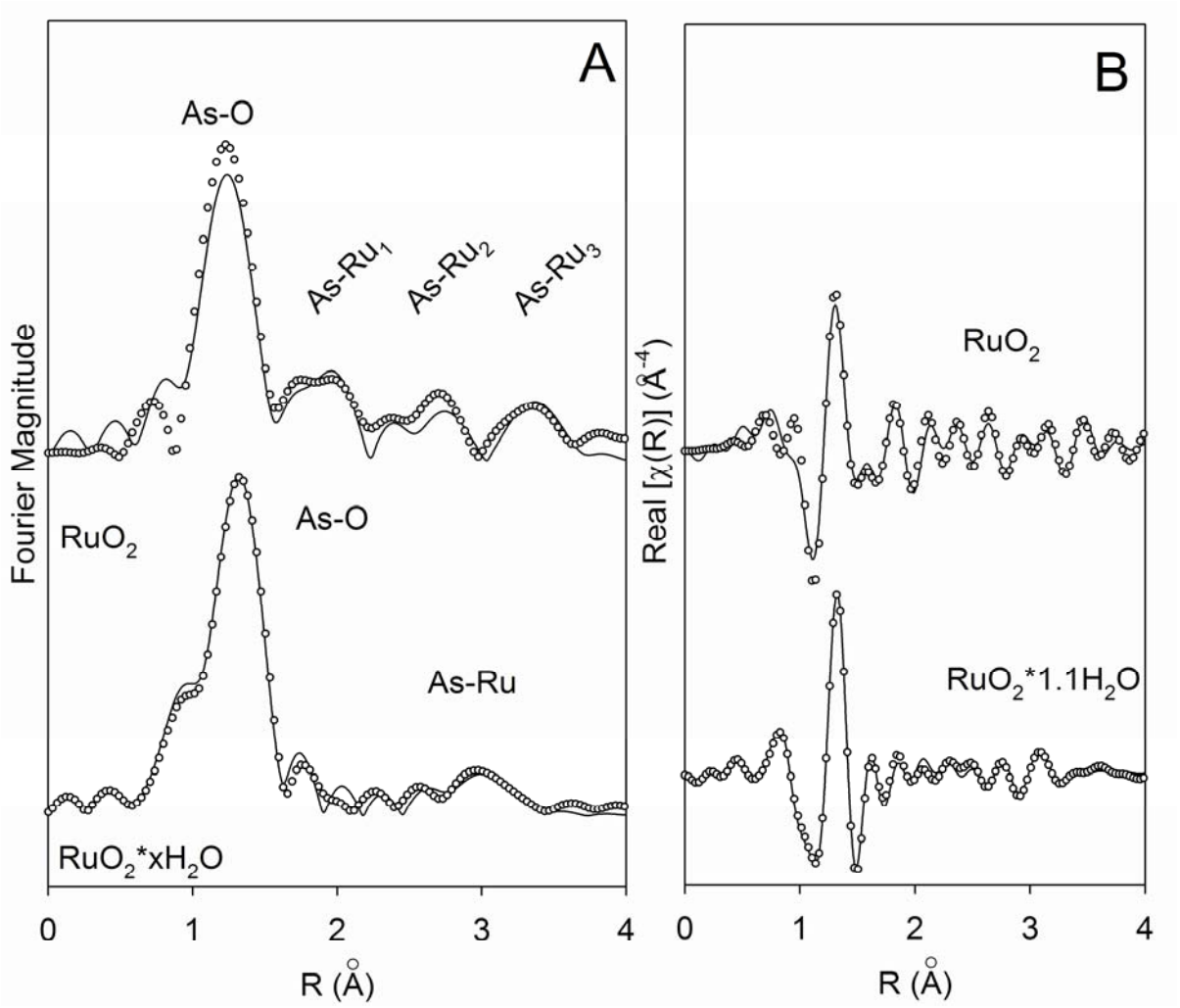

Figure 4-3 (A) Radial distribution functions for the 1.0 As:Ru adsorption ratio for RuO_2•1.1H_2O and RuO_2 (B) The real portion of the radial distribution functions for the complex FT depicted in A. Peaks in the FT associated with As-Ru scattering are indicated. Ru1-3 refers to the different adsorption complexes. The best fit parameter values are listed in Table 4-2. The symbols in the figure represent the data points and the lines represent the best fit from theoretical backscattering events.

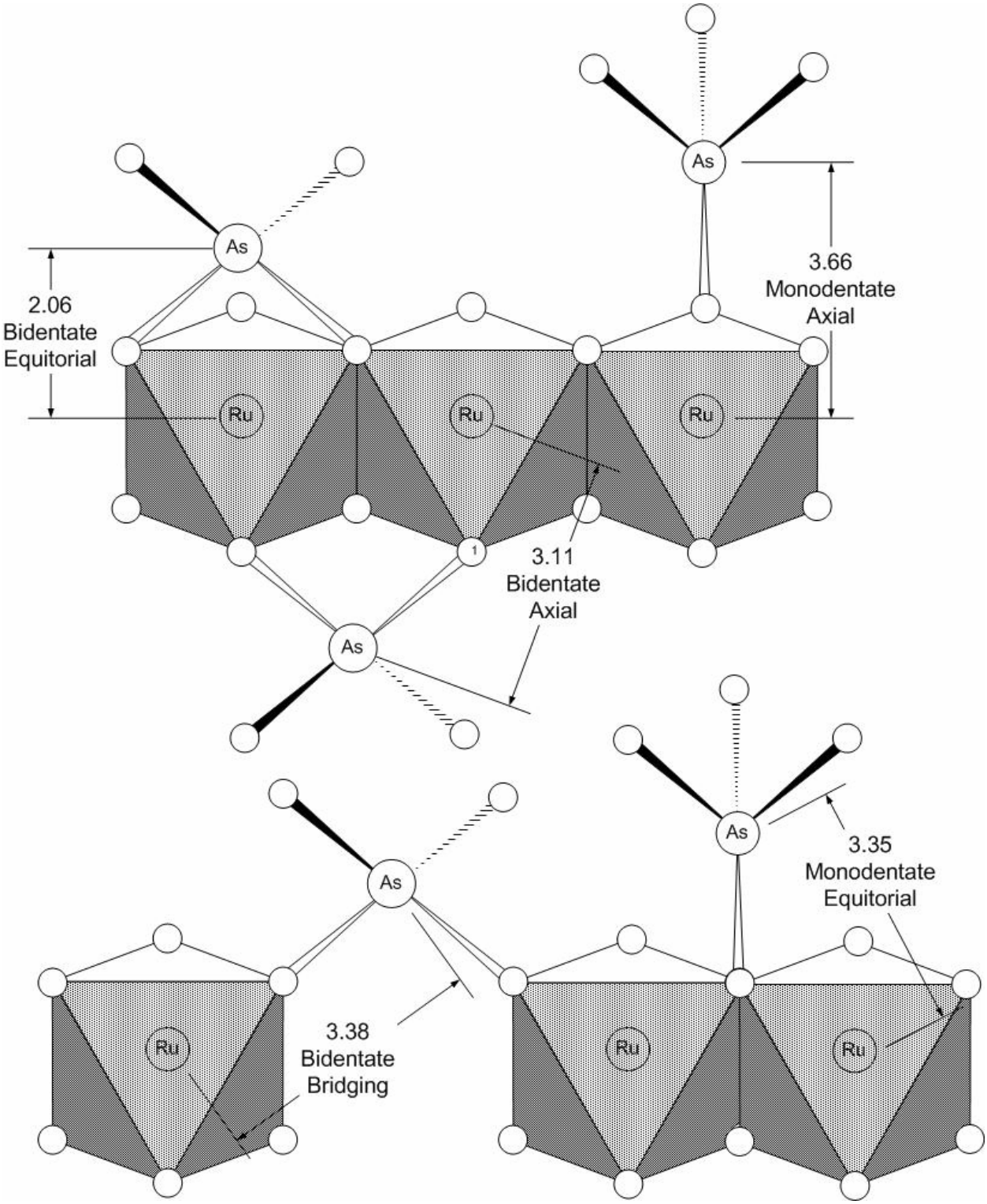

Figure 4-4 Schematic representation of the potential arsenate adsorption complexes on Ru-oxide. Distances were calculated from a theoretical crystal structure of RuO2 and the As-O bond distances and O-As-O bonds angles for a tetrahedral arsenate molecule. All distances are in angstroms.

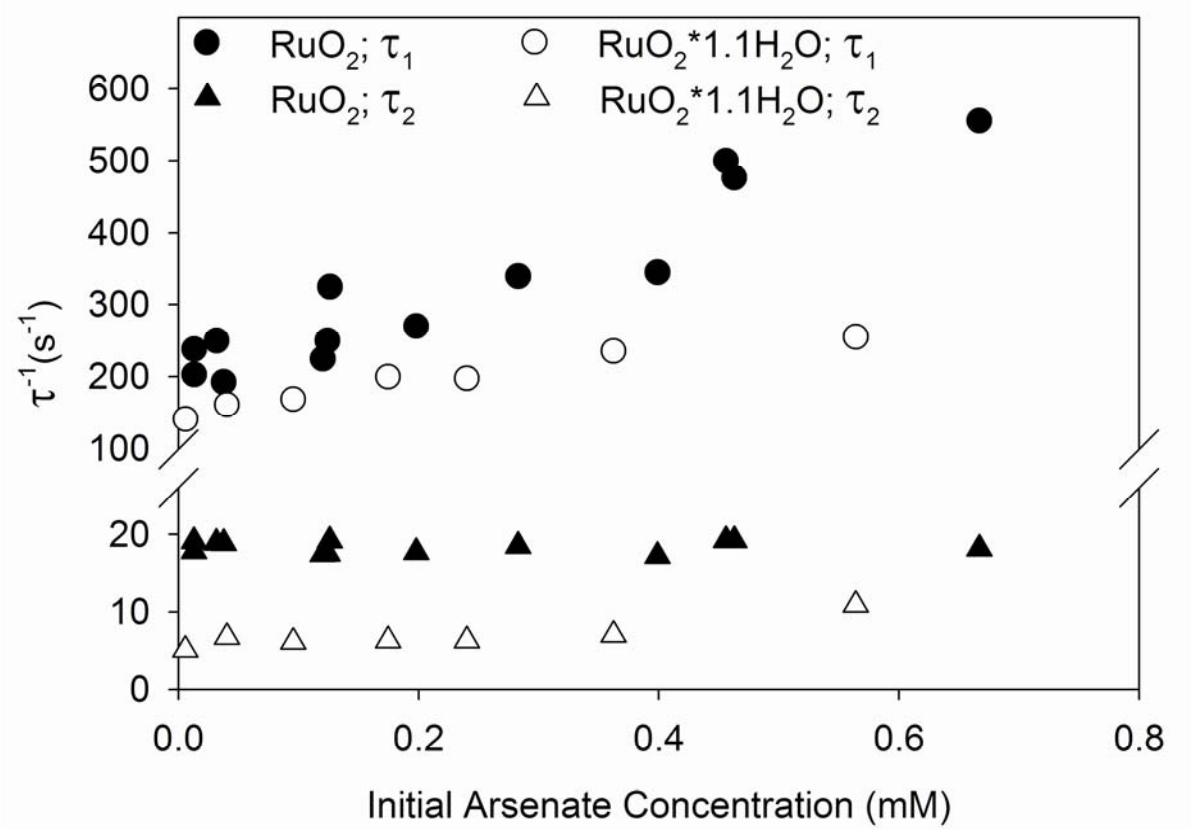

Figure 4-5 τ^{-1} values determined from p-jump experiments for arsenate adsorption/desorption from ruthenium oxides as a function of initial arsenate concentration. Data break occurs at 25 sec^{-1} on the y-axis.

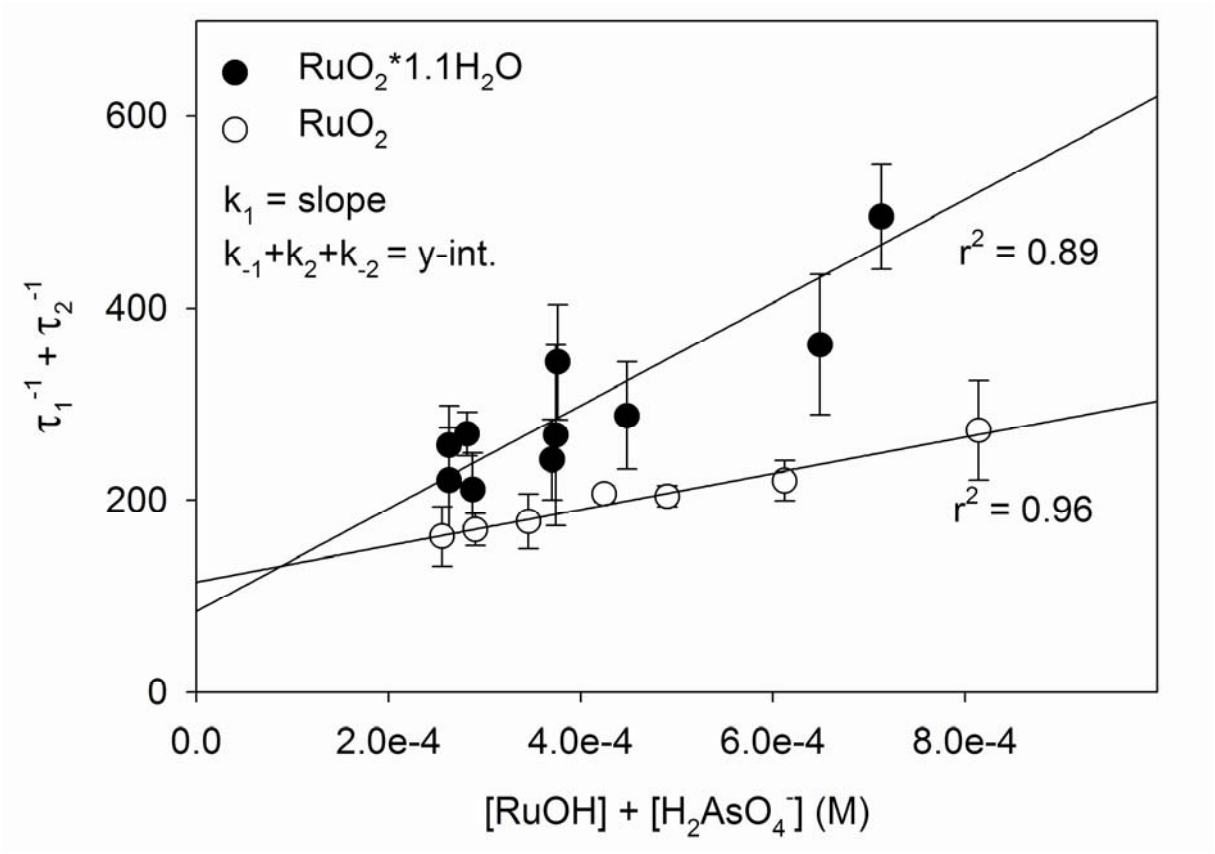

Figure 4-6 Evaluation of the linearized rate equation (Eq. 4-3) for the proposed two step mechanism regarding arsenate adsorption on amorphous and crystalline Ru-oxides.

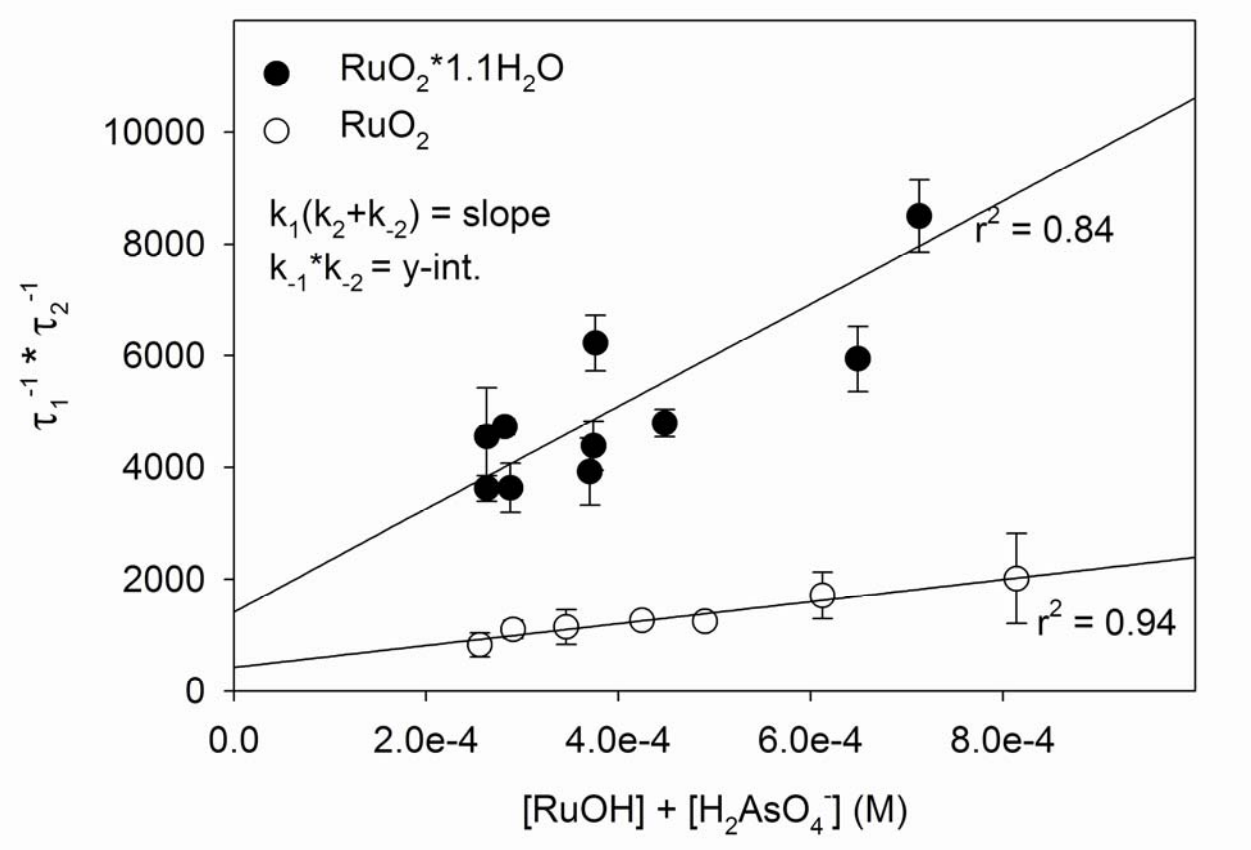

Figure 4-7 Evaluation of the linearized rate equation (Eq. 4-3) for the proposed two step mechanism regarding arsenate adsorption on amorphous and crystalline Ru-oxides.

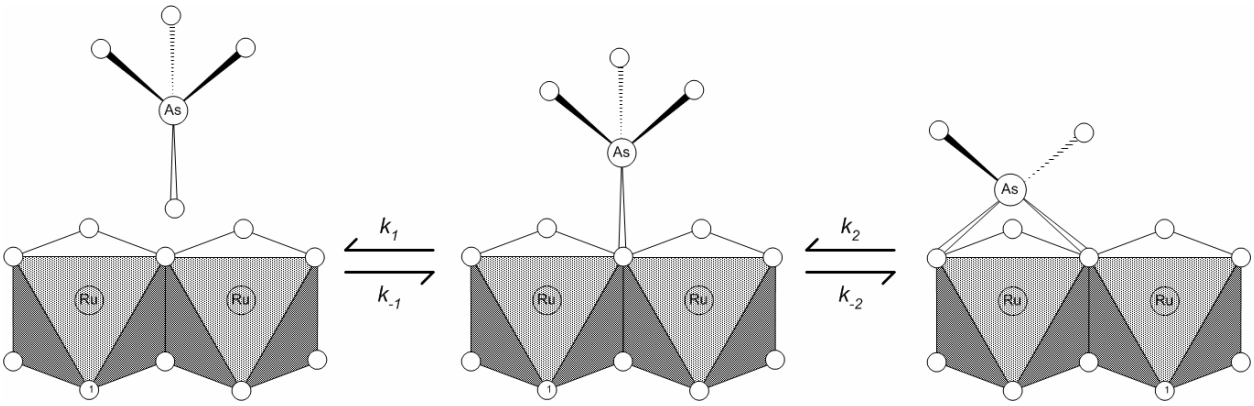

Figure 4-8 Schematic representation of the two step adsorption mechanism proposed for arsenate adsorption on Ru-oxide.

REFERENCES

Arai, Y., E.J. Elzinga, and D.L. Sparks. 2001. X-ray absorption spectroscopic investigation of arsenite and arsenate adsorption at the aluminum oxide-water interface. Journal of Colloid and Interface Science 235:80-88.

Beaulieu, B.T., and K.S. Savage. 2005. Arsenate adsorption structures on aluminum oxide and phyllosilicate mineral surfaces in smelter-impacted soils. Environmental Science & Technology 39:3571-3579.

Bernasconi, C.F. 1976. Relaxation Kinetics Academic Press, Inc., New York, NY.

Dixit, S., and J.G. Hering. 2003. Comparison of arsenic(V) and arsenic(III) sorption onto iron oxide minerals: Implications for arsenic mobility. Environmental Science & Technology 37:4182-4189.

Farquhar, M.L., J.M. Charnock, F.R. Livens, and D.J. Vaughan. 2002. Mechanisms of arsenic uptake from aqueous solution by interaction with goethite, lepidocrocite, mackinawite, and pyrite: An X-ray absorption spectroscopy study. Environmental Science & Technology 36:1757-1762.

Fendorf, S., M.J. Eick, P. Grossl, and D.L. Sparks. 1997. Arsenate and chromate retention mechanisms on goethite .1. Surface structure. Environmental Science & Technology 31:315-320.

Foster, A.L., G.E. Brown, Jr., and G.A. Parks. 2003. X-ray absorption fine structure study of As(V) and Se(IV) sorption complexes on hydrous Mn oxides. Geochimica et Cosmochimica Acta 67:1937-1953.

Frankenberger, W.T. 2002. Environmetal Chemistry of Arsenic Marcel Dekker, New York.

Fuller, C.C., J.A. Davis, and G.A. Waychunas. 1993. Surface-chemistry of ferrihydrite .2. Kinetics of arsenate adsorption and coprecipitation. Geochimica Et Cosmochimica Acta 57:2271-2282.

Goldberg, S., and C. Johnston. 2001. Mechanisms of arsenic adsorption on amorphous oxides evaluated using macroscopic measurements, vibrational spectroscopy, and surface complexation modeling. Journal of Colloid and Interface Science 234:204-216.

Grossl, P.R., M. Eick, D.L. Sparks, S. Goldberg, and C.C. Ainsworth. 1997. Arsenate and chromate retention mechanisms on goethite .2. Kinetic evaluation using a pressure-jump relaxation technique. Environmental Science & Technology 31:321-326.

Hochella, M.F, Jr. 1990. Atomic structure, microtopography, composition, and reactivity of mineral surfaces., *In* M. F. Hochella, Jr and A. F. White, eds. Mineral-Water Interface geochemistry, Vol. 23. Mineralogical society of America, Washington, D.C.

Huang, J.H., and J.S. Chen. 2001. Material characteristics and electrical property of reactively sputtered RuO2 thin films. Thin Solid Films 382:139-145.

Impellitteri, C.A., K.G. Scheckel, and J.A. Ryan. 2003. Sorption of arsenate and arsenite on RuO2•H(2)O: A spectroscopic and macroscopic study. Environmental Science & Technology 37:2936-2940.

Inskeep, W.P., T.R. McDermott, and S.E. Fendorf. 2002. As(V)/(III) cycling in soils and natural waters: chemical and microbiological processes, *In* W. T. Frankenberger, ed. Environmental Chemistry of Arsenic. Marcel Dekker, Inc., New York.

Ji, L., J. Lin, and H.C. Zeng. 2001. Thermal processes of volatile RuO2 in nanocrystalline Al2O3 matrixes involving gamma ->alpha phase transformation. Chemistry of Materials 13:2403-2412.

Lister, T.E., Y. Chu, W. Cullen, H. You, R.M. Yonco, J.F. Mitchell, and Z.U. Nagy. 2002. Electrochemical and X-ray scattering study of well defined RuO2 single crystal surfaces. Journal of Electroanalytical Chemistry 524-525:201-218.

Liu, C., and P.M. Huang. 2001. Pressure-jump relaxation studies on kinetics of lead sorption by iron oxides formed under the influence of citric acid. Geoderma 102:1-25.

Manceau, A. 1995. The Mechanism of Anion Adsorption on Iron-Oxides - Evidence for the Bonding of Arsenate Tetrahedra on Free Fe(O,OH)(6) Edges. Geochimica Et Cosmochimica Acta 59:3647-3653.

Manning, B.A., S.E. Fendorf, and S. Goldberg. 1998. Surface structures and stability of As(III) on goethite: evidence for inner sphere complexes. Environmental Science and Technology 32:2383-2388.

Manning, B.A., S.E. Fendorf, B. Bostick, and D.L. Suarez. 2002. Arsenic(III) oxidation and arsenic(V) adsorption reactions on synthetic birnessite. Environmental Science & Technology 36:976-981.

McKeown, D.A., P.L. Hagans, L.P.L. Carette, A.E. Russell, K.E. Swider, and D.R. Rolison. 1999. Structure of hydrous ruthenium oxides: Implications for charge storage. Journal of Physical Chemistry B 103:4825-4832.

Newville, M., P. Livins, Y. Yacoby, J.J. Rehr, and E.A. Stern. 1993. Near-Edge X-Ray-Absorption Fine-Structure of Pb - a Comparison of Theory and Experiment. Physical Review B 47:14126-14131.

Oscarson, D.W., P.M. Huang, and W.K. Liaw. 1980. The Oxidation of arsenite by aquatic sediments. Journal of Environmental Quality 9:700-703.

Oscarson, D.W., P.M. Huang, C. Defosse, and A. Herbillon. 1981. Oxidative power of Mn(IV) and Fe(III) oxides with respect to As(III) in terrestrial and aquatic environments. Nature 291:50-51.

Ravel, B., and M. Newville. 2005. ATHENA, ARTEMIS, HEPHAESTUS: data analysis for X-ray absorption spectroscopy using IFEFFIT. Journal of Synchrotron Radiation 12:537-541.

Rouquerol, F., J. Rouquerol, and K. Sing. 1999. Adsorption by Powders and & Porous Solids Academic Press, San Diego.

Sadiq, M. 1997. Arsenic Chemistry in soils: an overview of thermodynamic predictions and field observations. Water, Air, and Soil Pollution 93:117-136.

Sherman, D.M., and S.R. Randall. 2003. Surface complexation of arsenate(V) to iron(III) (hydr)oxides: Structural mechanism from ab initio molecular geometries and EXAFS spectroscopy. Geochimica et Cosmochimica Acta 67:4223-4230.

Singh, A.K. 2006. Chemistry of arsenic in groundwater of Ganges-Brahmaputra river basin. Current Science 91:599-606.

Smedley, P.L., and D.G. Kinniburgh. 2002. A review of the source, behavior and distribution of arsenic in natural waters. Applied Geochemistry 17:517-568.

Sparks, D.L., S.E. Fendorf, T.I.C. V., and T.H. Carski. 1996. Kinetic Methods and Measurements, p. 1275-1307, *In* D. L. Sparks, ed. Methods of Soil Analysis Part 3 Chemical Methods. Soil Science Society of America Inc., Madison, Wisconsin.

Stumm, W. 1992. Chemistry of the solid water interface John Wiley and Sons, New York.

Sun, X., and H.E. Doner. 1996. An investigation of arsenate and arsenite bonding structures on goethite by FTIR. Soil Science

161 12.

Tournassat, C., L. Charlet, D. Bosbach, and A. Manceau. 2002. Arsenic(III) oxidation by birnessite and precipitation of manganese(II) arsenate. Environmental Science & Technology 36:493-500.

Waychunas, G.A., J.A. Davis, and C.C. Fuller. 1995. Geometry of sorbed arsenate on ferrihydrite and crystalline FeOOH - Reevaluation of EXAFS results and topological factors in predicting sorbate geometry, and evidence for monodentate complexes. Geochimica et Cosmochimica Acta 59:3655-3661.

Waychunas, G.A., B.A. Rea, C.C. Fuller, and J.A. Davis. 1993. Surface-Chemistry of ferrihydrite .1. EXAFS studies of the geometry of coprecipitated and adsorbed arsenate. Geochimica et Cosmochimica Acta 57:2251-2269.

Yasunaga, T., and T. Ikeda. 1986. Adsorption-desorption kinetics at the metal-oxide-solution interface studied by relaxation kinetics American Chemical Society, Washington, D.C.

CHROMATE ADSORPTION BY RUTHENIUM OXIDES

ABSTRACT

The adsorption of chromate (Cr(VI)) by hydrous (RuO_2•$1.1H_2O$) and crystalline (RuO_2) ruthenium oxide was examined using macroscopic and spectroscopic techniques. Chromate adsorption on both oxides exhibited strong pH dependence with maximum adsorption occurring at low pH. Zeta potential measurements indicate a shift in the isoelectric point (IEP) of both solids upon addition of chromate. Subsequent additions of chromate resulted in a continued decrease in the IEP. The relative affinity of Cr(VI) for both oxides was determined by fitting the adsorption isotherm data with two equations. The model results indicate initially Cr(VI) has a higher affinity for RuO_2, that decreases with increasing surface concentrations of chromate. X-ray absorption near edge (XANES) spectra of Cr(VI) adsorbed to both oxides displayed a decrease in the intensity of the Cr(VI) pre-edge feature and a reduction in the adsorption edge energy indicating a portion of the Cr(VI) adsorbed to RuO_2•$1.1H_2O$ and RuO_2 is reduced to Cr(III). Radial distribution functions generated from the Fourier transforms of the extended x-ray adsorption fine structure (EXAFS) data reveal two back scattering distances for the first shell of oxygen in Cr adsorbed to ruthenium oxides. The two backscattering distances are equal to Cr-O atomic distances in Cr(VI) and Cr(III) compounds providing additional evidence for Cr(VI) reduction on RuO_2•$1.1H_2O$ and RuO_2 surfaces. Linear combination fitting (LCF) of the XANES data was used to quantify the relative proportion of Cr(III) to total Cr adsorbed on both oxide surfaces. Results from the LCS analysis demonstrate the percentage of Cr(III) to total Cr adsorbed reaches a maximum at low surface concentrations on both oxides before steadily decreasing with increasing surface concentrations of Cr. However, as the proportion of Cr(III) continues to decrease the total quantity of Cr(III) increases over the entire adsorption isotherm.

INTRODUCTION

Chromium is and has been used extensively in industrial applications ranging from metal alloying, electro metal plating, steel manufacturing (to increase material strength), metal surface coating to improve corrosion resistance, and animal hide tanning (Alvarez-Ayuso and Nugteren, 2005; Fendorf, 1995; Goswamee et al., 1998; Guha et al., 2001; Westbrook, 1983). Liquid and solid wastes generated from these industrial practices has resulted in the contamination of groundwaters, and soils throughout North America and Europe (Fendorf, 1995; Fetter, 1994). In natural environments chromium occurs in the (II), (III), and (VI) oxidation states, though the divalent state is unstable with respect to hydrogen evolution and is rarely present (Baes and Mesmer, 1976). The Cr(VI) species occurs as the chromate anion (CrO_4^{2-}), while the Cr(III) species occurs as the chromium cation (Cr^{3+}) (Baes and Mesmer, 1976). Chromium (Cr(III)) interacts strongly with organics and metal oxide surfaces forming highly stable surface adsorption complexes that are considered relatively inert and immobile (Peterson et al., 1997a). Chromate however, is considerably more mobile (Fendorf, 1995). Chromate does participate in adsorption reactions with Fe, Al, and Mn oxides resulting in the formation of both outer-and weakly bound inner-sphere surface complexes (Fendorf et al., 1997a; Grossl et al., 1997; Peterson et al., 1996). The mobility of the inner-sphere complex is a result of a high shared charged ratio from oxygen ligands coordinated to Cr(VI) (metal valence/No. Ligands = 6/4 = 1.5 shared charge) (McBride, 1994). The high charge value reduces the Lewis base properties of coordinated oxygen which results in the formation of weakly held surface complexes (McBride,

1994). Development of remediation strategies that result in the formation of stable Cr(VI) adsorption complexes or promote Cr(VI) reduction to the less toxic and more immobile Cr(III) species are of critical importance.

Numerous studies have evaluated the adsorption and reductive potential of metal oxides for chromate adsorption and sequestration. Much attention has been given to magnetites which are capable of reducing Cr(VI) under oxidizing conditions (Fendorf, 1995; Fendorf and Zasoski, 1992; Fendorf et al., 1994; Guha et al., 2001; Kendelelewicz et al., 2000; Peterson et al., 1996; Peterson et al., 1997a). Research investigating the mechanism responsible for Cr(VI) reduction indicates Cr(VI) is initially adsorbed through electrostactic interactions prior to reduction and specific adsorption of the reduced Cr species (Kendelelewicz et al., 2000; Peterson et al., 1996). Research also indicates the reduction potential of magnetite is finite due to the formation of Cr(III) secondary precipitate that prevents further reduction of Cr(VI) (Kendelelewicz et al., 2000). Recently Impelliterri, et al. (2004) and Scheckel et al. (2005) began studying the adsorption capabilities and capacity of ruthenium oxides. Their research has demonstrated the super adsorbent capacity of hydrous ruthenium oxides ($RuO_2 \cdot xH_2O$) which exhibited sorption capacities for arsenic and lead that exceeded those associated with tradition iron, aluminum, and manganese oxides. Additionally, Impelliterri, et al. (2004) demonstrated the compete oxidation of As(III) to As(V) by $RuO_2 \cdot xH_2O$. Previous research (Chapter 2) has demonstrated the insolubility of ruthenium oxides in acid and basic environments and in the presence of metal chelating and reducing organic ligands. Macroscopic, spectroscopic, and kinetic research previously conducted indicates both hydrous ($RuO_2 \cdot xH_2O$) and crystalline (RuO_2) ruthenium oxide readily undergo ligand exchange reactions with arsenate, oxalate, and ascorbate.

In the current study the adsorption behavior of chromate as a function of pH and initial solution concentration will be investigated over a broad pH range (3-10) and initial Cr(VI) concentrations (0.066-6.66 mM Cr(VI). The zeta potential of suspensions from the pH edge adsorption experiments will be determined to evaluate changes in the surface charge of ruthenium oxide upon addition of Cr(VI). Solid samples recovered for the adsorption isotherm will be analyzed by x-ray absorption spectroscopy to determine the oxidation state and the immediate local bonding environment of the adsorbed species.

MATERIALS AND METHODS

Ruthenium Oxide Characterization

Crystalline (RuO_2) and amorphous ($RuO_2 \cdot X\ H_2O$) ruthenium oxide used in the current study were obtained from a Ruthenium(IV) oxide hydrate Premion® (99.99% pure metal basis) from Alfa Aesar (Ward Hill, MA). The ruthenium oxide hydrate was purged under positive pressure N_2 gas for 5 days to remove sorbed argon from the packaging process. Thermogravimetric and calorimetric analysis (DuPont Instruments Hi-Res TGA 2950 and DSC 2910, New Castle, DE) of the solid phase were used to determine the quantity of structural water associated with the amorphous phase and the temperature at which conversion from the amorphous material to crystalline material occurred. Results from the thermal analysis indicated 1.1 moles of water per mole of material yielding the chemical formula $RuO_2 \cdot 1.1\ H_2O$ for the amorphous material. Thermal analysis also indicated that amorphous material underwent a

phase transformation to crystalline ruthenium oxide (RuO_2) at approximately 300^o C. After purging with N_2 gas RuO_2•1.1H_2O was used in the adsorption studies without any further treatments. The crystalline material was prepared by heating RuO_2•1.1H_2O to 500^o C for 24 hours in a muffle furnace. X-ray diffraction (Scintag® XDS 2000 X-ray Diffraction Spectrophotometer, Scintag Inc., Sunnyvale, CA), and differential scanning calorimetry data indicated a full conversion of RuO_2•1.1H_2O to crystalline RuO_2 with a rutile crystal structure. High resolution transmission electron microscopy (Titan S/TEM 80-300 X twin FEI microscope, Eindhoven, The Netherlands) images of the two oxides indicate the RuO_2•1.1H_2O material was amorphous in nature without any specific shape or size, while the RuO_2 was crystalline, exhibited a rutile structure with an average crystal size between 10 and 25 nm. Specific surface area (SSA) of the samples was measured by a 5 point Brunauer-Emmet-Teller (BET) sorption isotherm using a Micromoretics ASAP2010 Surface Area Analyzer (Norcross, GA). The SSA was 100 and 50 m^2 g^{-1} for theRuO_2•1.1H_2O and RuO_2, respectively. Nitrogen adsorption isotherms indicated 15 m^2 g^{-1} of micro-porous surface area for RuO_2•1.1H_2O and less than 1 m^2 g^{-1} RuO_2. The point of zero charge (PZC) for the two solids was 4.2±0.1 and 5.6±0.1 for the RuO_2•1.1H_2O and RuO_2, respectively. The PZC was determined by measurement of the isoelctric point (IEP) using a Zetasizer 3000HSa (Malvern Instruments, Southborogh, MA). Proton titrations of amorphous and crystalline Ru-oxide conducted in 0.01, 0.05 and 0.1 M NaCl with a 5 g L^{-1} suspension density indicated the surface concentration of titratable functional groups for each solid was 50 and 20 μmol m^{-2}, respectively. Titratable functional groups were defined by the micromole of acid and base consumed or produced by the solid phase during a titration from pH 2 to 11.

Batch Adsorption Experiments

Cr(VI) adsorption on ruthenium oxide was examined as a function of pH, Cr(VI) concentration, ruthenium oxide crystallinity, and suspension density. Experiments were conducted in duplicate at a constant ionic strength (0.01 M NaCl) using a pH-monitored stirred-batch reactor. For the adsorption experiments an appropriate quantity of N_2 sparged ruthenium oxide was weighed into a 500 mL glass beaker to which 350 mL of 0.01 M NaCl was added. The suspension was dispersed for ~2min using an ultrasonic dimembrator. The beaker was placed in a water jacketed reaction vessel kept at 25^o C, stirred using a Teflon coated magnetic stir bar, and kept under positive pressure with N_2 gas to eliminate CO_2. The suspension was allowed to hydrate for a period of 24 h while the pH was adjusted to the appropriate value using a Brinkman® 716 Stat-Trino pH stat (Brinkman Instruments, Westbury, NY) (with either 0.1 M HCl or NaOH). After the hydration period an appropriate quantity of a pH adjusted 100 mM Cr(VI) stock solution (made from a reagent grade sodium Cr(VI) salt) was added to the reactor to achieve the desired Cr(VI) concentration. The total volume was brought to 400 mL and a pH stat was used to maintain the appropriate pH. After three hours a 10 mL sample was removed and filtered through a 0.05 μm Millipore nitrocellulose filter (Billerica, MA) and the quantity of 0.1 M HCl added was recorded. The filtrate was analyzed by inductively coupled plasma atomic emission spectroscopy (ICP-AES) (SpectroFlame FTMOA85D, Spectro Analytical Instruments, Fitchburg, MA). The detection limit on the SpectroFlame ICP-AES for Cr and Ru was 5 and 12 μg L^{-1}, respectively. The quantity of oxyanion adsorbed was determined by subtracting the initial oxyanion concentration by the measured concentration.

Cr(VI) pH adsorption edges were conducted in a 0.5 g L^{-1} suspension over a broad pH range (3-10) at initial Cr(VI) concentrations 0.022 and 0.110 mM (1.70 and 8.50 mg L^{-1}). Adsorption experiments started at pH 10 and proceeded to pH 3 to avoid hysteresis effects associated with Cr(VI) desorption with increasing pH. After the addition of Cr(VI), the pH was adjusted to 10 and the system was allowed to equilibrate for 3 h. After the equilibration time period, two 10 mL samples were removed from the reactor for solution and zeta potential analysis. After sampling, the volume of titrant was recorded and the suspension was lowered one pH unit with 0.1 M HCl and allowed to re-equilibrate.

The Cr(VI) adsorption isotherm was conducted at pH 5 with a 1.0 g L^{-1} suspension density. The Cr(VI) concentration ranged from 0.033 to 6.6 mM. In between Cr(VI) additions the suspension was allowed to equilibrate for three hours. After three hours, two 10 mL samples were removed for solution analysis and zeta potential analysis.

Zeta Potential Analysis

Zeta potentials were calculated from microelectrophoresis measurements collected using a Malvern Zetasizer 3000HSa (Malvern Instruments, Southborogh, MA). Based on preliminary data, the voltage applied to the capillary cell was set at 100 mV and a Henry function ($f(K_a)$) of 1.5 to 1.23 was used to calculate zeta potential. The pH of each sample was measured prior to zeta potential measurement to account for any drift in pH. The reported zeta potential values are the average of 10 microelectrophoresis measurements. The standard deviation for all zeta potential measurements was less 1.5 mV.

X-ray Absorption Fine Structure Spectroscopy

Samples analyzed by extended x-ray absorption fine structure spectroscopy (EXAFS) were filtered through a 0.05 μm Millipore filter and washed three times with 10 mL of pH adjusted 0.01 M NaCl to remove any entrained Cr(VI) not associated with the surface. The resulting paste was stored moist in between two filter papers in a sealed plastic bag (3.8 x 5 cm) at 5 ^{o} C until analysis. No more than 12 h prior to analysis the samples were transferred to a 0.25 mm thick polycarbonate sample holder affixed with Kapton® tape on both sides to hold the sample in place and prevent drying. Chromium K-edge spectra (5989eV) were collected at beamline 20-BM (Pacific Northwest Consortium Collaborative Access Team) at the Advanced Photon Source at Argonne National Laboratory, Argonne, IL. EXAFS spectra were collected in fluorescence mode using an Ar filled Lytle detector with a 3 μm thick Z-1 filter to reduce unwanted x-ray fluorescence. The electron storage ring operated at 7 GeV. The light source was equipped with a Si 111 monochromator with the horizontal slit set at 6 mm and the vertical at 2.3 mm. Scans were collected from 11,699 to 12, 867 eV.

The collected spectra were analyzed using the Athena and Artemis software programs (Ravel and Newville, 2005) in the computer package IFEFFIT (Version 1.2.9, 2006). At least three individual spectra were averaged followed by subtraction of the background through the pre-edge region using the Autobk algorithm (Newville et al., 1993). The averaged spectra were normalized to an atomic absorption of one. The spectra were fit with the FEFF8 computer code which uses ab initio calculations to determine phase shift and amplitude functions for single and multiple atomic scattering paths. Each spectrum was fit by isolating the first shell of Cr

adsorbed on RuO_2•1.1$H_2O$and RuO_2 and fitting the data with Cr in tetrahedral and octahedral coordination with oxygen, fitting was conducted in R-Space

RESULTS

Batch Adsorption Experiments

The pH dependent adsorption of Cr(VI) on RuO_2•1.1H_2O and RuO_2 was typical of stronger acid oxyanion adsorption and similar in nature to Cr(VI) adsorption on Fe and Al (hydr)oxides (Aide and Cummings, 1997; Eick et al., 1999; Grossl et al., 1997; Mesuere and Fish, 1992; Samad and Watson, 1997; Zachara et al., 1987) (Figure 5-1). Upon the addition of a pH adjusted Cr(VI) stock solution to either Ru-oxide suspension there was an immediate increase in pH. Titration with 0.1 M HCl was required for the first half hour after Cr(VI) addition to maintain pH. On a surface area basis RuO_2•1.1H_2O and RuO_2 had similar surface concentrations for both the 0.022 and 0.110 mM Cr(VI) concentrations. However, on a mass basis, the quantity of Cr(VI) removed from solution by RuO_2•1.1H_2O was nearly double that of the crystalline material for both initial Cr(VI) concentrations.

Total Cr(VI) adsorption capacity was determined from an adsorption isotherm conducted at pH 5 for both Ru oxide phases (Figure 5-2). The adsorption isotherm exhibited L and S-shape adsorption behavior over the range of Cr(VI) concentrations investigated (Sposito, 1984). Initially, Cr(VI) adsorption exhibited an L-shape isotherm (Figure 5-2 inset) prior to an exponential increase in Cr(VI) surface concentrations resulting in an S-shape isotherm. When the Cr(VI) isotherm is presented on a surface area basis, the concentration of adsorbed Cr(VI) on RuO_2 is nearly double that of RuO_2•1.1H_2O (Figure 5-2). When presented on a mass basis (Figure 5-3) the adsorption isotherm data indicates nearly identical adsorption behavior. The difference between the data presentation in Figures 5-2 and 5-3 highlights the importance of surface area when evaluating the adsorption capacity of metal oxides. Chromate adsorption on both oxides was modeled with the Langmuir equation.

$$q_{\mathrm{Cr}} = \frac{bKC_{\mathrm{Cr}}}{1 + KC_{\mathrm{Cr}}} \qquad (5\text{-}1)$$

In Equation 5-1 q_{Cr} equals adsorbed Cr(VI) (mmol g^{-1}) and C_{Cr} equals Cr(VI) solution concentration (mM). The constants b and K are adjustable parameters related to the asymptotic value of q_{Cr} as C_{Cr} becomes arbitrarily large (b), and the magnitude of the initial slope (K) (Sposito, 1984; Sposito, 1989). The portion of the adsorption data that was well described by the Langmuir equation is shown in the inset of Figure 5-3A. Beyond surface concentrations of 0.6 and 0.3 mmol g^{-1} for RuO_2•1.1H_2O and RuO_2, respectively Cr(VI) adsorption exhibited exponential growth which was modeled by a general exponential growth equation.

$$q_{\mathrm{Cr}} = q_L + ae^{(K_D C_{\mathrm{Cr}})} \qquad (5\text{-}2)$$

In Equation 5-2, the variable q_{Cr} and C_{Cr} are identical to Eq. 5-1, q_L equals the y-intercept (q_o) minus a ($q_L = q_o - a$), a is an adjustable parameter, and K_D is the ratio of adsorbed and aqueous Cr(VI)as follows:

$$K_D = \ln a * \frac{q_{Cr} - q_L}{C_{Cr}} \qquad (5\text{-}3)$$

The model results for Equations 5-1 and 5-2 are presented in Figure 5-3, and the values for all of the variables used are presented in Table 5-1 along with the adjusted R^2 value and p-value from

the nonlinear least squares regression analysis using Sigma Plot 10.0 (Systat software, Inc, 2006).

Zeta Potential Analysis

Changes in the surface potential of oxide minerals at a specific pH or a shift in the oxides point of zero charge (PZC) due to adsorbing cations and anions can be used as an indirect method for elucidating sorption mechanisms. A decrease in the surface potential of RuO_2•$1.10H_2O$ and RuO_2 with the addition Cr(VI) would suggest the formation of an inner-sphere complex. The decrease in the surface potential or (PZC) results from the adsorption of ions with protonizable functional groups. The adsorbed complex can undergo protonation/deprotonation reactions that will contribute to particle charge and surface potential (Anderson and Malotky, 1979).

Zeta potential measurements for RuO_2•$1.1H_2O$ and RuO_2 were collected from pH 3 to 10, in the presence of 0.00, 0.022, 0.110 mM Cr(VI) (Figure 5-4). The isoelectric point (IEP) or PZC of the two Ru-oxides in the absence of arsenate was 4.2 and 5.6 for the amorphous and crystalline material, respectively. The addition of Cr(VI) to either Ru-oxide phase resulted in a decrease in the PZC. Successive additions of Cr(VI) further reduced the IEP of both materials, suggesting that Cr(VI) forms an inner-sphere complex with Ru-oxide. The continued decrease in the PZC with successive additions of Cr(VI) provides an additional evidence for the formation of an inner sphere surface complex.

X-ray Absorption Fine Structure Spectroscopy

Solid samples from the Cr(VI) adsorption isotherms were analyzed by X-ray adsorption fine structure spectroscopy. XANES spectra displayed a reduction in the intensity of the Cr(VI) pre-edge feature and a shift to higher energy for the Cr absorption energy (Figure 5-5). A reduction in the pre-edge feature and a shift in the absorption energy of Cr(VI) is often associated with mixed Cr oxidation states (i.e. Cr(VI) and Cr(III)) (Peterson et al., 1996; Peterson et al., 1997a). EXAFS data also indicated the presence of both Cr(VI) and Cr(III) adsorbed on both Ru-oxide surfaces (Figure 5-6). Results from modeling the first shell of the Fourier transformed EXAFS data of adsorbed Cr (peaks 1 and 2 in Figure 5-6) are related to electron backscattering from oxygen atoms located 1.66±0.02, and 1.99±0.03 Å from Cr. The two scattering distances determined for peak 1 and 2 coincide with previously published atomic distances for Cr(VI)-O (1.67 Å) and Cr(III)-O (1.99 Å) atomic distances, indicating both Cr oxidation states are present at the Ru-oxide surface (Figure 5-6) (Fendorf et al., 1997b; Hoffmann et al., 2001; Peterson et al., 1996; Peterson et al., 1997a).

Linear combination fitting (LCF) of Cr(VI) (Na_2CrO_4) and Cr(III) (Cr_2O_3) standards was used to determine the relative percentage of each Cr species adsorbed to RuO_2•$1.1H_2O$ and RuO_2. Previous research using LCF to determine the percentage of Cr(III) and Cr(VI) in XANES spectra from known molar ratios demonstrated the technique was accurate within 6% of the actual molar ratio present (Peterson et al., 1997a). Linear combination fitting was done from -30 to 100 eV above the absorption edge with the Ifeffit computer software package (Version 1.2.9, 2006) implemented through the Athena software program (Ravel and Newville, 2005). Results from the LCF indicate that both Cr(VI) and Cr(III) are present on RuO_2•$1.10H_2O$ and RuO_2. Overall, the majority of the adsorbed Cr is in the oxidized form (Cr(VI) (Table 5-2). At

the most Cr(III) comprises 47 and 35% of the total Cr adsorbed for RuO_2•$1.1H_2O$ and RuO_2, respectively. Surface normalized concentrations for Cr(III) were calculated using the results of the LCF, and plotted as a function of the total Cr adsorbed (Figure 5-7). The percentage of Cr(III) to total Cr adsorbed reached a maximum at 0.51 and 0.62 μmol m^{-2} for RuO_2•$1.1H_2O$ and RuO_2, respectively (Table 5-2). However, the surface concentration of Cr(III) adsorbed on both oxides continued to increase over the entire adsorption edge (Figure 5-7 and Table 5-2).

DISCUSSION

Previous spectroscopic research indicates Cr(VI) adsorbs to most metal oxide surfaces through a ligand exchange reaction resulting in the formation of an inner-sphere surface complex (Fendorf et al., 1997b; Grossl et al., 1997; Peterson et al., 1997a). Adsorption isotherms and pH edge data presented in the literature and numerous other studies are similar to the Cr(VI) adsorption results obtained in this study (Aide and Cummings, 1997; Eick et al., 1999; Fendorf et al., 1997b; Garman et al., 2004; Grossl et al., 1997; Li et al., 2003; Mesuere and Fish, 1992; Peterson et al., 1997a; Zachara et al., 1987). The similarity between Cr(VI) adsorption on RuO_2•$1.1H_2O$ and RuO_2 compared with other metal oxides and the production of hydroxyls during Cr(VI) adsorption suggests it adsorbs to RuO_2•$1.1H_2O$ and RuO_2 through a ligand exchange mechanism. Additionally a reduction in the IEP for both oxides following Cr(VI) adsorption suggests the formation of an inner-sphere surface complex.

Based on the surface normalized Cr(VI) adsorption isotherm, Cr(VI) appears to have a higher affinity for the RuO_2 surface since the surface concentration is nearly double that for RuO_2•$1.1H_2O$ (Figure 5-2). However, the surface area for RuO_2•$1.1H_2O$ is double that of RuO_2 and on a mass basis the adsorption isotherms are nearly identical (Figure 5-3). Empirical modeling results of Cr(VI) adsorption onto both oxides was used to determine if Cr(VI) demonstrated a preference for RuO_2•$1.1H_2O$ or RuO_2. Results from the Langmuir equation indicate initially Cr(VI) has a greater affinity for RuO_2 which is related to an increase in the value of K, or the initial slope of the L-shaped isotherm (Figure 5-3A and Table 5-1). At elevated concentrations the results of the exponential growth equation (Eq. 5-2) indicate a similar distribution of Cr between the oxide surface and solution for both phases, demonstrating a similar affinity of Cr(VI) for either surface (K_D in Table 5-2). While the K_D values for both oxides are similar, the surface concentration of Cr(VI) on RuO_2 at the highest concentration investigated was 20.17 μmol m^{-2}, slightly greater than the quantity of reactive functional groups present on RuO_2 (20 μmol m^{-2}). The quantity of Cr(VI) adsorbed compared with the reactive surface site concentration, suggests that oxyanion adsorption is not the only mechanism involved in Cr(VI) sequestration. The reduction of Cr(VI) to Cr(III) with increasing Cr(III) over the adsorption isotherm may result in the formation of a Cr(III) hydroxide, explaining the large quantity of Cr adsorbed by RuO_2. Previous research has demonstrated that Cr(III) will precipitate as a hydroxide phase mineral surfaces (Fendorf et al., 1994; Kendelelewicz et al., 2000; Peterson et al., 1996). Furthermore, Peterson et al. (1996) noted a reduction in the quantity of Cr(VI) as Cr(VI) surface concentrations increased. They attributed this to the formation of a Cr(III) oxide/hydroxide phase at the surface of magnetite. Similar results for a decrease in the quantity of Cr(VI) reduced, compared to total Cr adsorbed, at higher surface loadings was noted in the current study suggesting the formation of a secondary Cr(III) precipitate on the RuO_2 surface (Table 5-2).

The increased affinity of Cr(VI) for RuO_2 at low pH may be related to the reduction of Cr(VI) to Cr(III) as demonstrated by the XAFS data and LCF analysis of the XANES spectra. The two spectra presented in Figure 5-5 and the RDF in Figure 5-6 are indicated by arrows in Figures 5-2 and 5-7, and are italic in Table 5-2. The relative percentage of Cr(III) on the surface of RuO_2•$1.1H_2O$ and RuO_2 reaches a maximum at low surface concentrations (0.51 and 0.63 μmol m^{-2} for RuO_2•$1.1H_2O$ and RuO_2, respectively) before steadily decreasing thereafter (Table 5-2). At the maximum percentage of Cr adsorbed as Cr(III), there is an greater quantity of Cr(III) on the RuO_2 surface compared to RuO_2•$1.1H_2O$ surface. Furthermore, the maximum percentage of Cr(III) present on RuO_2 occurs at an initial solution concentration an order of magnitude less than that of RuO_2•$1.1H_2O$ (Table 5-2). The increased quantity of Cr(VI) reduction at lower initial solution concentrations suggests a more chemically reactive surface which results in the increased initial slope (K value) in the Langmuir equation.

The origin of S-shaped adsorption isotherms are generally attributed to cooperative interaction among the adsorbed phase (Sposito, 1984). In the current research the S-shaped portion of the isotherm occurs after an initially large proportion of the total Cr adsorbed is reduced to Cr(III). The reduction of Cr(VI) to Cr(III) would reduce the negative potential of the oxide surface creating a more positive surface charge due to the ionic form and adsorption complex of each Cr species. An increase in the positive surface charge resulting from Cr(VI) reduction may promote additional Cr(VI) adsorption by reducing the magnitude of the negative surface potential produced by anion adsorption resulting in a cooperative interaction among the adsorbed species (Figure 5-2, 5-3, and 5-7).

The mechanism by which Cr(VI) is reduced to Cr(III) is not readily apparent, but more than likely involves the oxidation of Ru. Future research regarding reduction mechanism should focus on quantifying the oxidation state of Ru present in both oxides prior to and after addition of Cr(VI) since both RuO_2•$1.1H_2O$ and RuO_2 are known to contain mixed Ru oxidation states. Soft x-ray core photoemission spectroscopy or high resolution x-ray photoelectron spectroscopy could provide detailed information regarding the Ru oxidation states present prior to and after adsorption (Kendelelewicz et al., 2000). Furthermore cyclic voltammetry studies could be used to elucidate the active redox couples during Cr(VI) reduction to determine the ratio of moles of Ru/moles of Cr(VI) reduced (Kendelelewicz et al., 2000; Lyons and Burke, 1987; Zen et al., 2001). Additional research focused on modeling the EXAFS data beyond the first shell of oxygen will also aid in determining the Cr(VI) reduction mechanism by determining if Cr(III) hydr(oxide) phases are present.

CONCLUSIONS

The current research demonstrates the adsorption capacity of and electrochemical properties of RuO_2•$1.1H_2O$ and RuO_2. Chromate adsorption on RuO_2•$1.1H_2O$ and RuO_2 appears to occur through ligand exchange mechanism, resulting in the formation of a inner-sphere surface complex, based on solution chemical data, zeta potential measurements, and current and previous spectroscopic research evaluating Cr(VI) adsorption on other metal oxides. The isotherm and pH edge data for Cr(VI) were similar to previously published adsorption data. Empirical modeling of the adsorption isotherm data with a Langmuir and exponential growth equation indicates that at low surface concentrations Cr exhibits a preference for RuO_2. The S-shaped portion of the adsorption isotherm is attributed to the reduction of Cr(VI) and the

subsequent reduction in surface potential that would be associated with Cr(III) adsorption complexes.

XANES and EXAFS spectroscopy indicate the reduction of Cr(VI) to Cr(III) occurred on both oxide surfaces. The relative proportion of Cr(III) to Cr(V) was determined from LCF calculations using a Cr(VI) and Cr(III) standard. The proportion of Cr(III) adsorbed to total Cr adsorbed reached a maximum at low surface concentration, however the quantity of Cr(III) present on the Ru-oxide surface increased over the entire adsorption isotherm.

The results further demonstrate the dynamic nature of the Ru-oxide surface through the reduction of Cr(VI) to the less toxic Cr(III) (Fendorf, 1995). Previous research evaluating the reduction of Cr(VI) on magnetite demonstrates that a finite quantity of Cr(VI) is reduced before the precipitation of a Cr(III) (hydro)oxide phase inhibits the reaction (Kendelewicz et al., 2000; Peterson et al., 1997b). The inhibitory effect of a Cr(III) (hydr)oxide phase is not apparent in the current results even at surface concentrations equal to the quantity of surface functional groups, suggesting that ruthenium oxide may provide improved reduction of Cr(VI) compared to other oxide surfaces.

In addition to reducing Cr(VI), previous research has demonstrated the complete oxidation of As(III) to As(V) by hydrous ruthenium oxide (Impellitteri et al., 2003). Current and previous research demonstrates that ruthenium oxides behave as both oxidants and reductants in solution. The unique electrochemical behavior combined with the large sorption capacity makes the oxide a unique material for adsorption of an array of highly toxic trace elements present in natural and engineered environments. Additionally, the redox properties of $RuO_2 \cdot 1.1H_2O$, RuO_2, and similar redox active materials allows for the potential for remediation strategies designed to simultaneously oxidize and reduce specific contaminants to less harmful or more recalcitrant forms.

TABLES

Table 5-1 Modeling results from the Langmuir and exponential growth equations used to describe Cr(VI) adsorption onto RuO_2•1.1H_2O and RuO_2. All of the regression results had an adjusted R2 value of 0.98 or above and were significant at $\alpha = 0.01$.

Equation	Variables	Solid Phase		Statistics	
		RuO_2	RuO_2•1.1H_2O	RuO_2	RuO_2•1.1H_2O
Langmuir $q_{Cr} = \frac{bKc_{Cr}}{1+Kc_{Cr}}$	b	0.0431±0.001	0.0463±0.004	$R^2 = 0.85$	$R^2 = 0.98$
	K	68.602±7.40	42.90±5.20	p-value = 0.020	p-value = 0.007
Exponential $q_{Cr} = q_L * ae^{(xc_{Cr})}$	q_L	-0.048±0.01	-0.056±0.03	$R^2 = 0.99$	$R^2 = 0.99$
	q_0			p-value = 0.001	p-value = 0.015
	a	0.08±0.01	0.08±0.02		
	K_D	0.46±.01	0.44±.04		

Table 5-2 Linear combination fitting of X—ray absorption fine structure analysis of Cr adsorbed to RuO_2•1.1H_2O and RuO_2. Italicized correspond to the data presented in Figure 5-5.

Initial Cr (mM)	Results from the LCF Analysis Percent of XANES Spectra Attributed to Each Species			Cr Adsorbed μmol m^{-2}	
	Cr(III)[a]	Cr(VI)	Cr Total	Cr(III)[b]	Cr(VI)
		RuO_2•1.1H_2O			
0.033	20	80	0.19	0.04	0.15
0.067	26	74	0.28	0.07	0.20
0.133	23	77	0.34	0.08	0.26
0.334	*47*	*53*	*0.38*	*0.18*	*0.20*
0.667	40	60	0.51	0.20	0.31
1.335	31	69	1.05	0.33	0.73
3.337	30	70	2.82	0.85	1.98
6.674	12	88	10.56	1.27	9.29
		RuO_2			
0.033	25	75	0.42	0.10	0.31
0.067	*35*	*65*	*0.62*	*0.22*	*0.41*
0.133	30	70	0.78	0.23	0.55
0.334	30	70	0.80	0.24	0.56
3.337	9	91	5.28	0.48	4.80
6.674	10	98	20.17	2.02	18.15

FIGURES

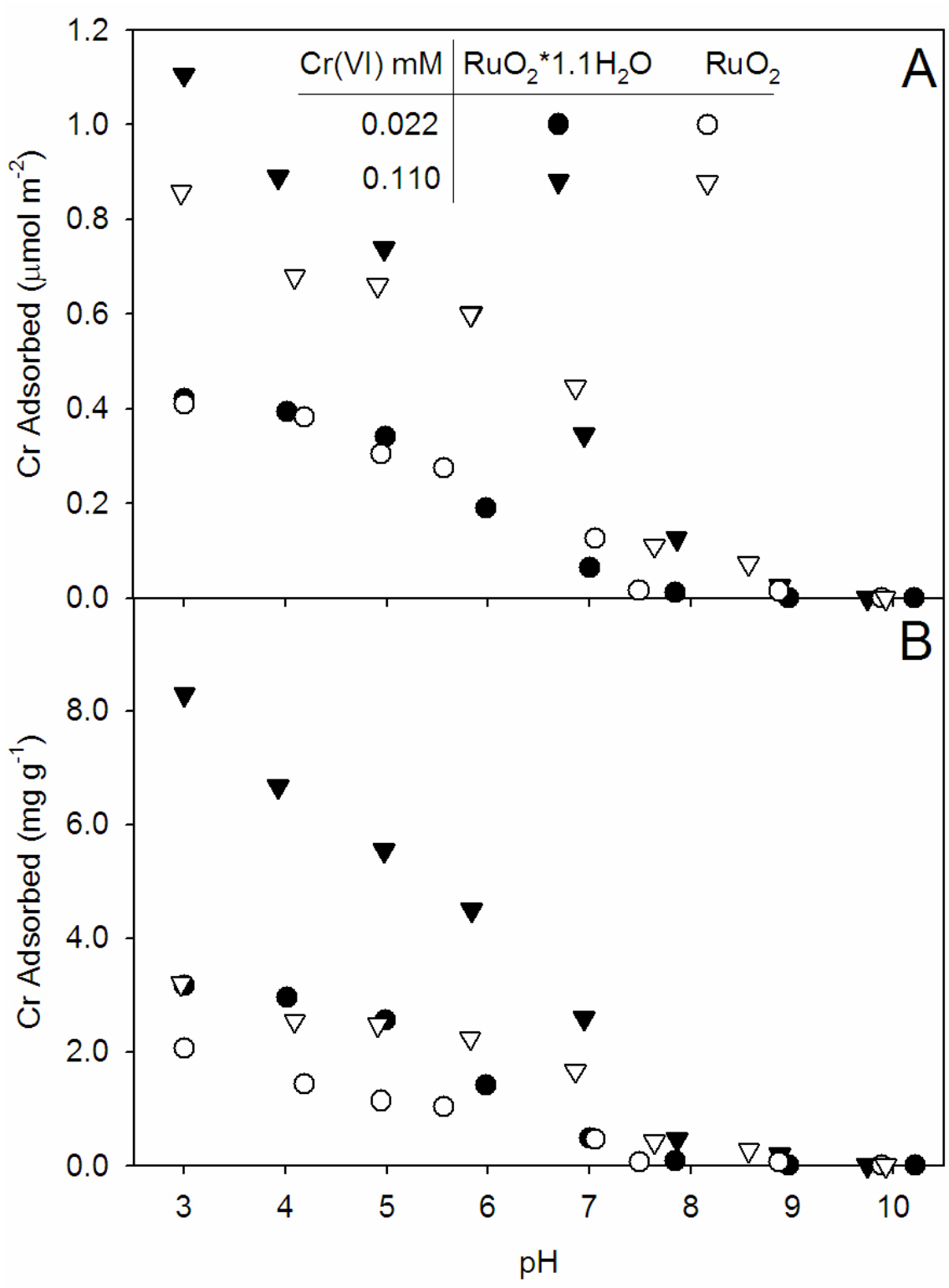

Figure 5-1 Cr(VI) adsorption on RuO_2•1.1H_2O and RuO_2. (A) Cr(VI) adsorption on a surface area basis. (B) Cr(VI) adsorption on a mass basis.

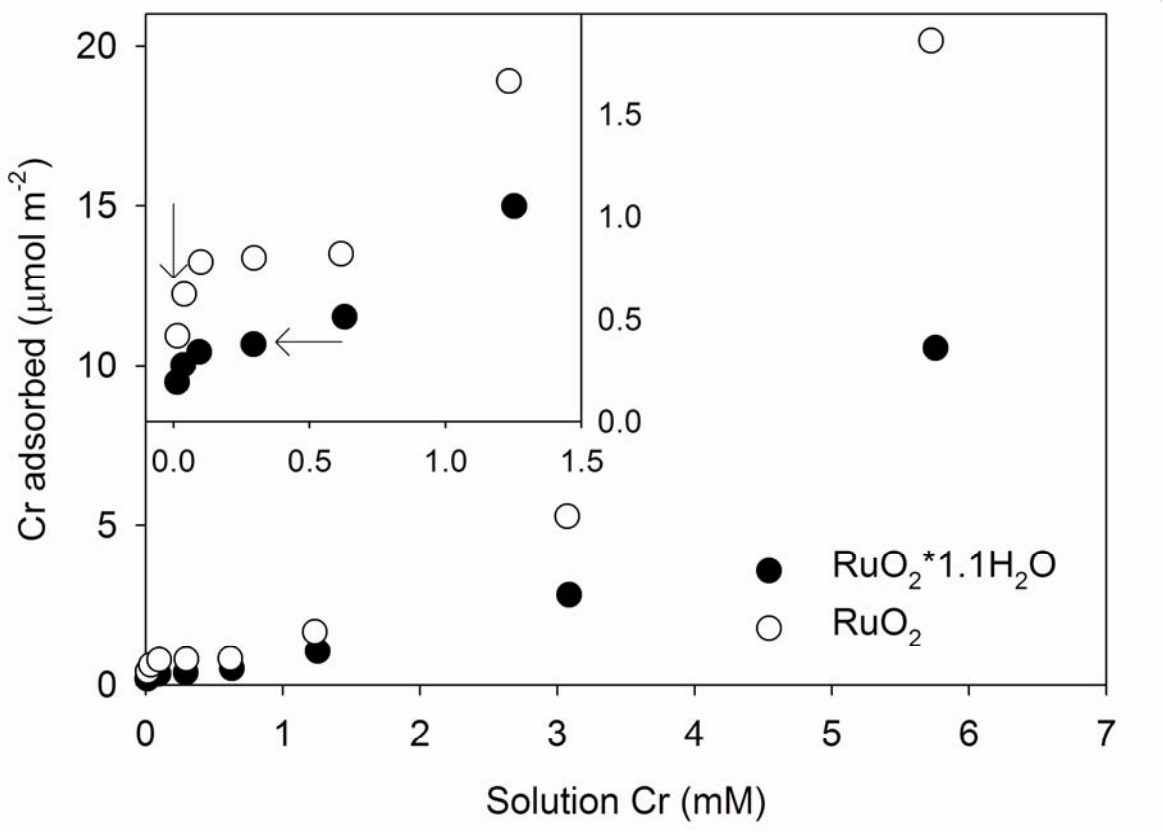

Figure 5-2 Cr(VI) adsorption isotherm conducted on RuO_2•1.1$H_2O$and RuO_2. Inset shows adsorption isotherm from 0.00 to 0.15 mM Cr. Arrows indicate XANES spectra presented in Figure 5-5.

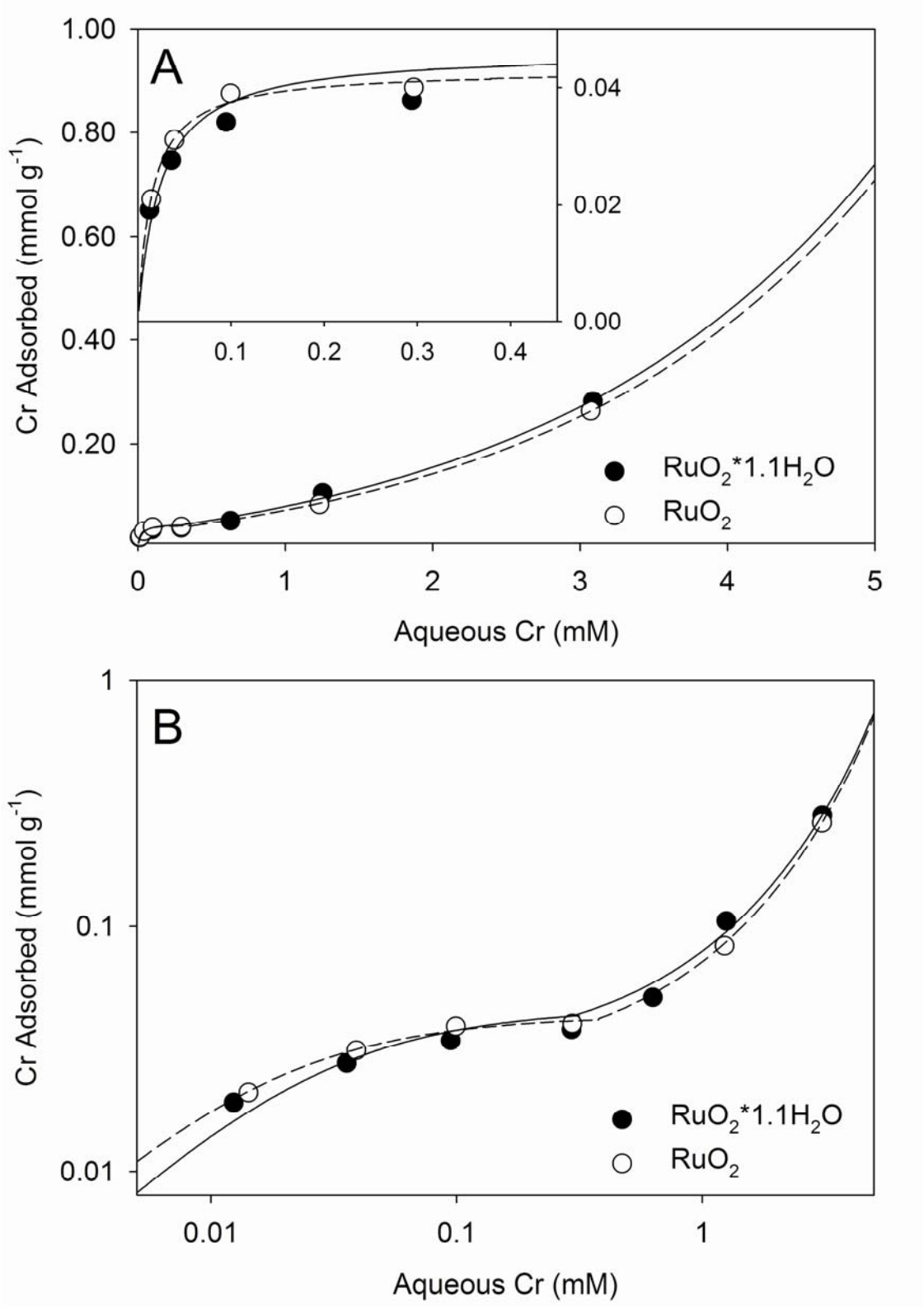

Figure 5-3 Cr(VI) adsorption isotherm conducted on RuO_2•1.1H_2O and RuO_2. (A) Linear Scale. (B) Double logarithmic scale. Symbols denote data points and lines represent mathematical models. Inset in (A) shows Cr(VI) adsorption isotherm from 0 to 0.15 M Cr, same axes.

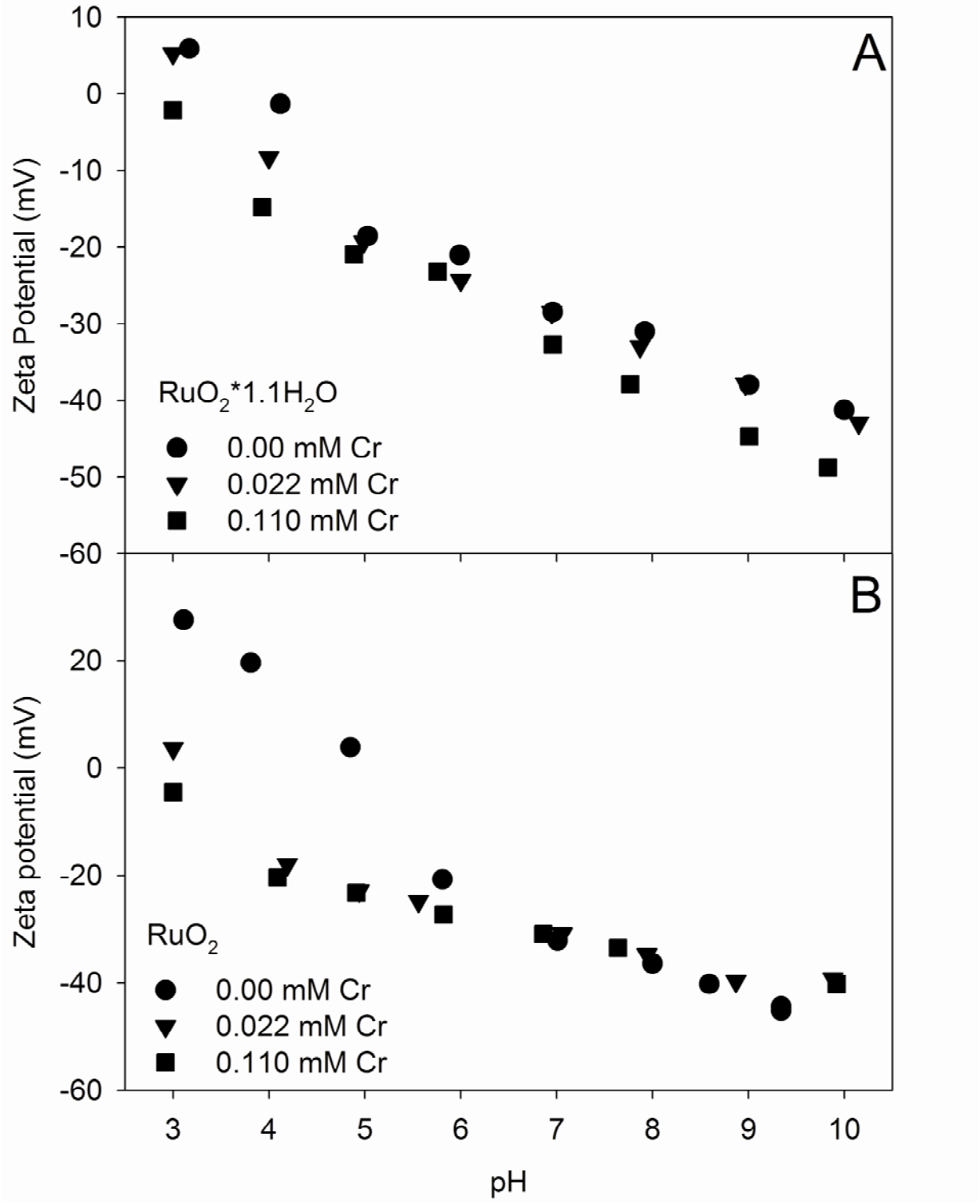

Figure 5-4 Zeta potential measurements for Cr(VI) adsorption on RuO_2•1.1H_2O and RuO_2 at two initial Cr(VI) concentrations, 0.022 and 0.110 mM. (A) RuO_2•1.10H_2O. (B) RuO_2.

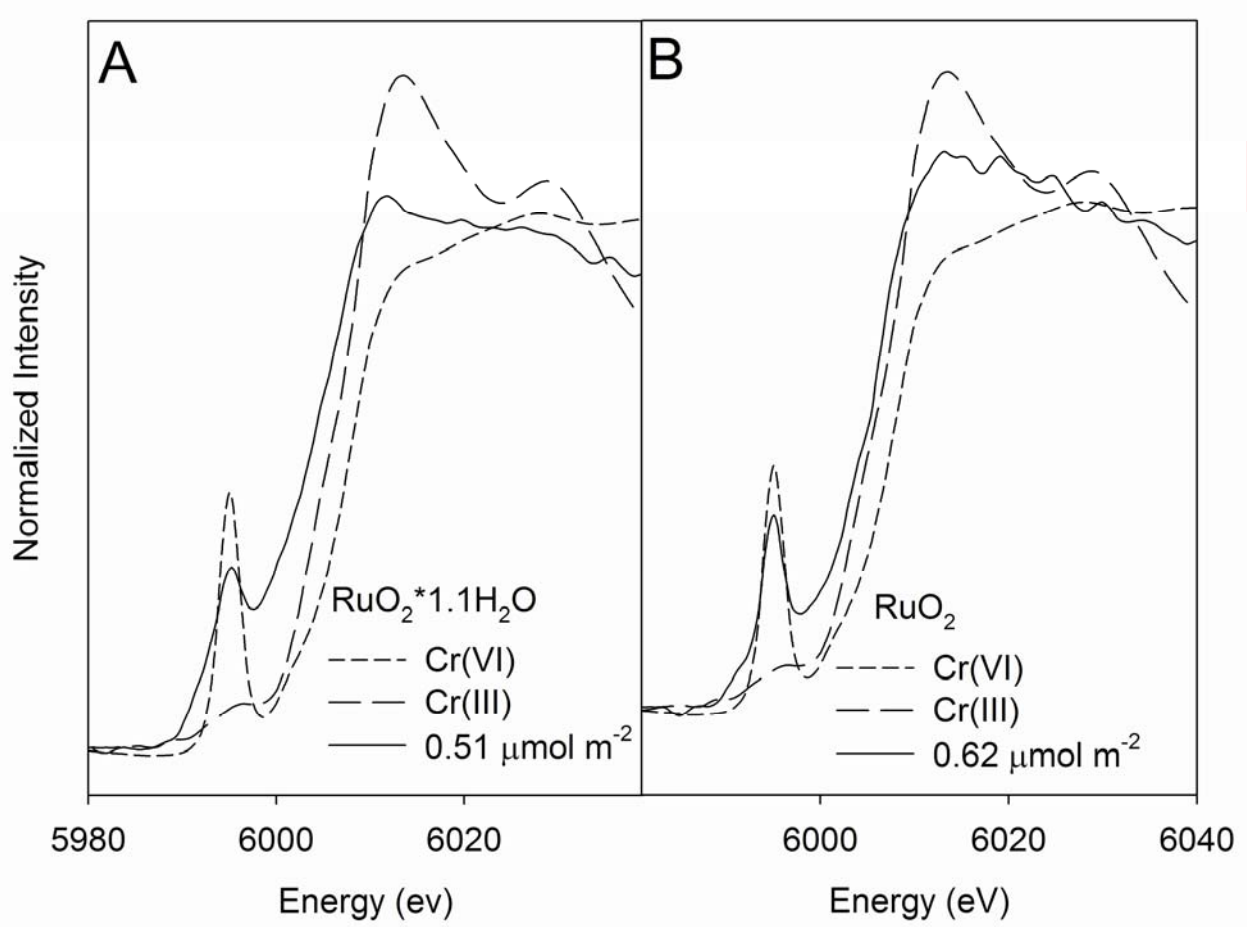

Figure 5-5 XANES spectra for Cr adsorbed to RuO_2•1.1H_2O and RuO_2. The spectra presented for Cr(VI) is from a potassium salt (Na_2CrO_4) and the spectra for Cr(III) is from a chromium sesquioxide (Cr_2O_3).

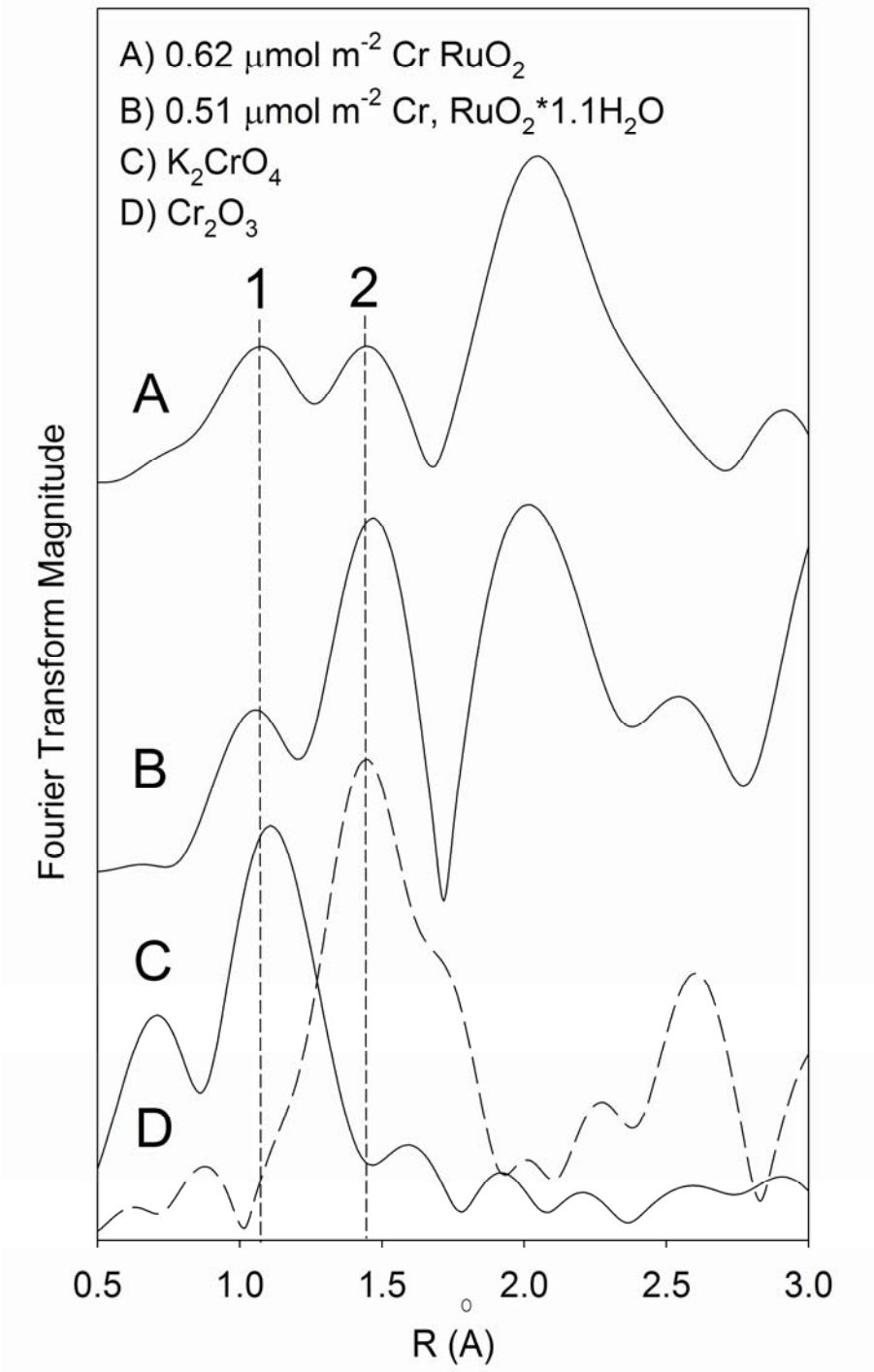

Figure 5-6 Radial distribution functions for potassium chromate, chromium sequioxide, and Cr adsorbed on RuO_2•1.1H_2O and RuO_2. Peaks represent atomic distances (uncorrected for phase shifts) between Cr and nearby atoms.

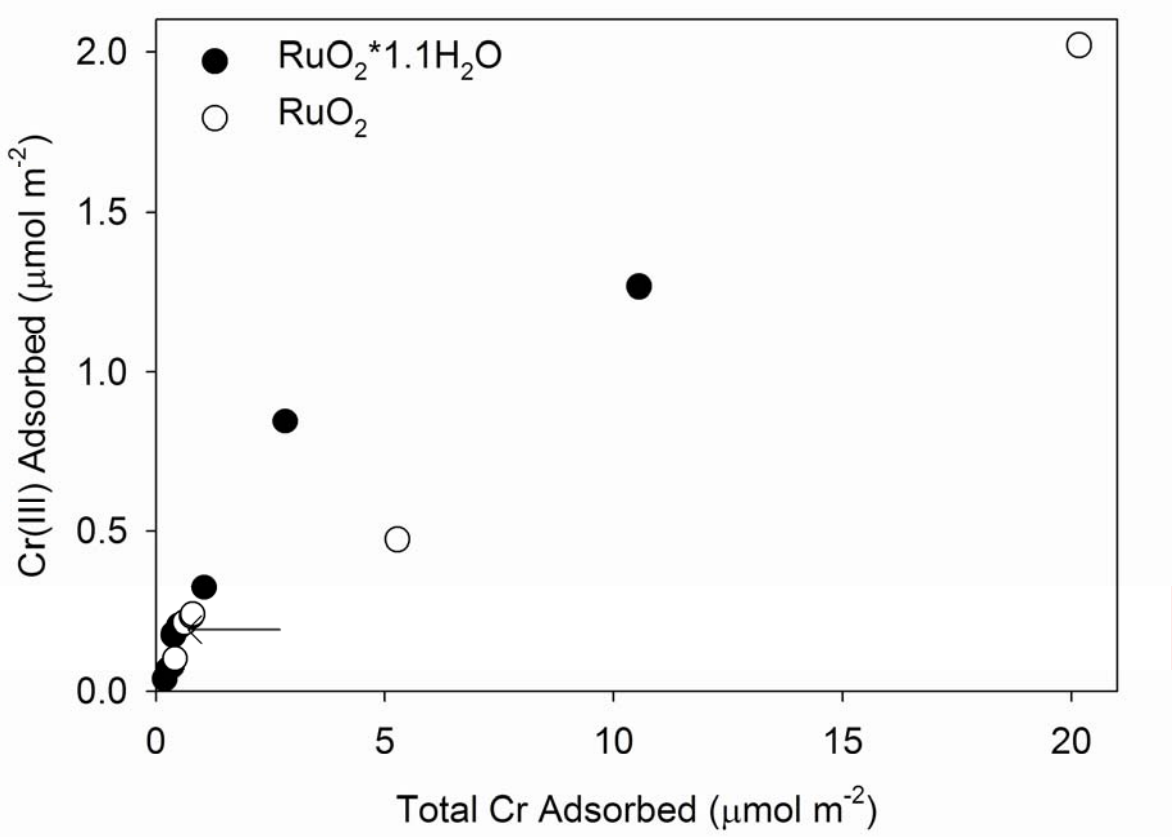

Figure 5-7 Surface concentration of Cr(III) as determined from the LCF analysis plotted a s function of total Cr adsorbed on RuO_2•1.1H_2O and RuO_2. Arrows indicate the two Cr XANES and EXAFS spectra presented in Figure 5-5 and 5-6.

REFERENCES

Aide, M.T., and M.F. Cummings. 1997. The influence of pH and phosphorus on the adsorption of chromium (VI) on boehmite. Soil Science 162:599-603.

Alvarez-Ayuso, E., and H.W. Nugteren. 2005. Purification of chromium(VI) finishing wastewaters using calcined and uncalcined Mg-Al-CO3-hydrotalcite. Water Research 39:2535-2542.

Anderson, M.A., and D.T. Malotky. 1979. The adsorption of protolyzable anions in hydrous oxides at the isoelectric pH. Journal of Colloid and Interface Science 72:413-427.

Baes, J.C.F., and R.E. Mesmer. 1976. The Hydrolysis of Cations Wiley-Interscience, New York.

Eick, M.J., J.D. Peak, and W.D. Brady. 1999. The effect of oxyanions on the oxalate-promoted dissolution of goethite. Soil Science Society of America Journal 63:1133-1141.

Fendorf, S., M.J. Eick, P. Grossl, and D.L. Sparks. 1997a. Arsenate and chromate retention mechanisms on goethite 1. Surface structure. Environmental Science & Technology 31:315-320.

Fendorf, S., M.J. Eick, P. Grossl, and D.L. Sparks. 1997b. Arsenate and chromate retention mechanisms on goethite .1. Surface structure. Environmental Science & Technology 31:315-320.

Fendorf, S.E. 1995. Surface-Reactions of chromium in soils and waters. Geoderma 67:55-71.

Fendorf, S.E., and R.J. Zasoski. 1992. Chromium(III) Oxidation by Delta-Mno2 .1. Characterization. Environmental Science & Technology 26:79-85.

Fendorf, S.E., G.M. Lamble, M.G. Stapleton, M.J. Kelley, and D.L. Sparks. 1994. Mechanisms of chromium(III) sorption on silica .1. Cr(III) surface-structure derived by extended x-ray-absorption fine-structure spectroscopy. Environmental Science & Technology 28:284-289.

Fetter, C.W. 1994. Applied Hydrogeology. 3rd ed. Prentice Hall, Upper Saddle River, NJ.

Garman, S., M.J. Eick, and T.P. Luxton. 2004. Kinetics of chromate adsorption on goethite in the presence of sorbed silicic acid. Journal of Environmental Quality 33:1703-1708.

Goswamee, R.L., P. Sengupta, K.G. Bhattacharyya, and D.K. Dutta. 1998. Adsorption of Cr(VI) in layered double hydroxides. Applied Clay Science 13:21-34.

Grossl, P.R., M. Eick, D.L. Sparks, S. Goldberg, and C.C. Ainsworth. 1997. Arsenate and chromate retention mechanisms on goethite 2. Kinetic evaluation using a pressure-jump relaxation technique. Environmental Science & Technology 31:321-326.

Guha, H., J.E. Saiers, S. Brooks, P. Jardine, and K. Jayachandran. 2001. Chromium transport, oxidation, and adsorption in manganese-coated sand. Journal of Contaminant Hydrology 49:311-334.

Hoffmann, M.M., J.G. Darab, and J.L. Fulton. 2001. An infrared and X-ray absorption study of the structure and equilibrium of chromate, bichromate, and dichromate in high-temperature aqueous solutions. Journal of Physical Chemistry A 105:6876-6885.

Impellitteri, C.A., K.G. Scheckel, and J.A. Ryan. 2003. Sorption of arsenate and arsenite on RuO2•xH(2)O: A spectroscopic and macroscopic study. Environmental Science & Technology 37:2936-2940.

Kendelelewicz, T., P. Liu, C.S. Doyle, and G.E. Brown, Jr. 2000. Spectroscopic study of the reaction of aqueous Cr(VI) with Fe3O4 (111) surfaces. Surface science 469:144-163.

Kendelewicz, T., P. Liu, C.S. Doyle, and G.E. Brown, Jr. 2000. Spectroscopic study of the reaction of aqueous Cr(VI) with Fe3O4(111) surfaces. Surface Science 469:144-163.

Li, Z., C.A. Willms, and K. Kniola. 2003. Removal of anionic contaminants using surfactant-modified palygorskite and sepiolite. Clays and Clay Minerals 51:445-451.

Lyons, M.E.G., and L.D. Burke. 1987. Mechanism of oxygen reactions at porous oxide electrodes .1. Oxygen evolution at Ruo2 and RuO2•xH(2)O electrodes in alkaline-solution under vigorous electrolysis conditions. Journal of the Chemical Society-Faraday Transactions I 83:299-321.

McBride, M.B. 1994. Environmental Chemistry of Soils Oxford Press, New York.

Mesuere, K., and W. Fish. 1992. Chromate and oxalate adsorption on goethite .1. Calibration of surface complexation models. Environmental Science & Technology 26:2357-2364.

Newville, M., P. Livins, Y. Yacoby, J.J. Rehr, and E.A. Stern. 1993. Near-Edge x-Ray-absorption fine-structure of Pb - a comparison of theory and experiment. Physical Review B 47:14126-14131.

Peterson, M.L., G.E. Brown, Jr., and G. Parks. 1996. Direct XAFS evidence for heterogeneous redox reaction at the aqueous chromium/magnetite interface
Colloids and Surfaces A: Physicochemical and Engineering Aspects 107:77-88.

Peterson, M.L., G.E. Brown, Jr.,G.A. Parks, and C.L. Stein. 1997a. Differential redox and sorption of Cr(III/VI) on natural silicate and oxide minerals: EXAFS and XANES results. Geochimica et Cosmochimica Acta 61:3399-3412.

Peterson, M.L., A.F. White, G.E. Brown, Jr., and G.A. Parks. 1997a. Surface passivation of magnetite by reaction with aqueous Cr(VI): XAFS and TEM results. Environmental Science & Technology 31:1573-1576.

Ravel, B., and M. Newville. 2005. ATHENA, ARTEMIS, HEPHAESTUS: data analysis for X-ray absorption spectroscopy using IFEFFIT. Journal of Synchrotron Radiation 12:537-541.

Samad, A.H., and P.R. Watson. 1997. An XPS study of the adsorption of chromate on goethite (alpha-FeOOH). Applied Surface Science 108:371-377.

Sposito, G. 1984. The surface chemistry of soils Oxford University Press, New York.

Sposito, G. 1989. The Chemistry of Soils Oxford University Press, New York.

Westbrook, J. 1983. Chromium and Chromium Alloys, p. 54-82, *In* M. Grayson, ed. Kirk-Othmer Encyclopedia of Chemical Technology, Vol. 6, 3rd ed. Wiley Interscience, New york, NY.

Zachara, J.M., D.C. Girvin, R.L. Schmidt, and C.T. Resch. 1987. Chromate adsorption on amorphous iron oxyhydroxide in the presence of major groundwater ions. Environmental Science & Technology, ES & T 21:589-594.

Zen, J.M., A.S. Kumar, and J.C. Chen. 2001. Electrochemical behavior of lead-ruthenium oxide pyrochlore catalyst: redox characteristics in comparison with that of ruthenium dioxide. Journal of Molecular Catalysis a-Chemical 165:177-188.

VITA

Todd Peter Luxton

Address and Contact Information

252 Smyth Hall CSES
Virginia Tech
Blacksburg, VA 24061

Phone: (540) 239-6785
Fax: (540) 231-3431
Email: tluxton@vt.edu

Education

2003-2007 Virginia Polytechnic Institute and State University

Ph.D. Candidate Environmental Chemistry
Advisor: Dr. Matthew Eick
Dissertation Topic: *Oxyanion Adsorption by Iron and Ruthenium Oxides: A Macroscopic, Spectroscopic and Kinetic Investigation*

2000 -2002 Virginia Polytechnic Institute and State University
M.S. Environmental Soil Chemistry
Advisor Dr. Matthew Eick
Thesis Topic: *Competitive Adsorption of Silicic Acid and Arsenite on Geothite*

1997-2000 *The* Pennsylvania State University
B.S in Environmental Soil Science
Minor Geosciences
Senior Thesis Advisor: Dr. Jon Chorover
Senior Thesis Topic: *The Influence of Dissolved Organic Matter on Lead Desorption Kinetics form Rifle Range Soils*

Professional Experience

2007-Present Post Doctoral Fellow at United States, Environmental Protection Agency, Office of Research and Development, National Risk Management Laboratory, Cincinnati, OH

2003-2007 Graduate Fellow and Teaching Assistant at Virginia Polytechnic Institute and State University—Graduate Teaching Instructor for Environmental Soil Chemistry and Soil Physical and Colloidal Chemistry

2002-2003 Research Associate in the Crop and Soil Environmental Science Department, Virginia Polytechnic Institute and State University

2000-2002 Graduate Teaching Assistant, Department of Crop and Soil Environmental Sciences, The Virginia Polytechnic Institute and State University—Introductory Soils Laboratory, Soils in the Landscape Laboratory, Introduction to Environmental Science

2000 (May-August)	Environmental Consultant at Crouse and Company, Pittsburgh, PA
1999-2000	Undergraduate Researcher at The Pennsylvania State University, State College, PA
Professional Affiliations	American Chemical Society Geochemical Society of America Mineralogical Association of America Soil Science Society of America

Fellowships and Awards

2006	U. S. Department of Energy, Advanced Photon Source EXAFS School (July 26th through the 28th)
2006	C.I. Rich Scholarship, Virginia Tech for Excellence in Graduate Education
2005	NSF-IGERT, EIGER (Exploring Interfaces through Graduate Education and Research) Fellowship Recipient
2005	Waste Policy Institute, Virginia Tech Fellowship Recipient
2004	U. S. Environmental Protection Agency, Research Grant
2004	Department of Education GAANN Fellowship Recipient

Publications

Luxton. T. P., M. J. Eick, S. M. Garman. 2007. Soil chemical properties as a tool in archeological investigations: Identifying previous anthropogenic disturbances. In Preparation.

Luxton, T. P., M. J. Eick, and K. G. Scheckel. 2007. Chromate adsorption and reduction by ruthenium oxides. Submitted

Luxton, T. P., M. J. Eick, and K. G. Scheckel. 2007. Characterization and dissolution behaviour of ruthenium oxides. Submitted.

Luxton, T. P., M. J. Eick, and K. G. Scheckel. 2007. Arsenate adsorption by amorphous and crystalline ruthenium oxides. Submitted.

Luxton, T. P., M. J. Eick, and K. G. Scheckel. 2007. Arseante adsorption on ruthenium oxide: a spectroscopic and kinetic investigation. Submitted.

Luxton, T. P., M. J. Eick, and J. D. Rimstidt. 2007. Kinetics of the competitive adsorption of arsenite and silicic acid on goethite. Soil Science Society of America Journal. In Review.

Madden, A. S., M. F. Jr. Hochella, and T. P. Luxton. 2006. Insights for size dependent reactivity of hematite nano-surfaces through Cu^{2+} adsorption. Geochimica et Cosmochimica Acta. 70:4095-4104.

Luxton, T. P., C. J. Tadanier, and M. J. Eick. 2006. Competitive adsorption of arsenite and silicic acid on goethite. Soil Science Society of America 70:204-214.

Garman, S., M. J. Eick, and T. P. Luxton. 2004. Chromate adsorption on goethite in the presence of silicic acid. Journal of Environmental Quality 33:1703-1708.

Kogut, L. S. and T. P. Luxton. 2002. Collaborative learning in general chemistry with CQI monitoring and evaluation. Effective Teaching for Meaningful Learning. http://wwwcsi.unian.it/educa/.

Conference Presentations

Luxton, T. P. and Eick, M. J. 2006. Silica polymerization on goethite and its influence on ligand promoted dissolution. 18th World Congress of Soil Science, Philadelphia, PA.

Luxton, T. P., Eick, M. J., and Garman, S. M. 2006. Soil chemical properties as a tool in archeological
investigations: Identifying previous anthropogenic disturbances. 18th World Congress of Soil Science, Philadelphia, PA.

Luxton, T. P., Eick, M. J. Scheckel, K. G. 2004. Dissolution and characterization of ruthenium oxide. Annual Meeting of the Soil Science Society of America, Seattle, WA.

Luxton, T. P. Eick, M. J. 2004. Modelling arsenite and silicic acid adsorption on goethite using the CD MUSIC surface complexation model. Annual Meeting of the Soil Science Society of America, Seattle, WA.

Tadanier, C. J., T. Luxton, and M. Eick. 2002. Competitive adsorption of oxyanions. Goldschmidt Conference, Davos, Switzerland.

Luxton, T. P. and M. J. Eick, 2001. Competitive adsorption of monosilicic acid and arsenite on goethite. Annual Meeting of the Soil Science Society of America, Charlotte, NC.